QUANTITATIVE MEASUREMENT OF LIGHTNING-INDUCED
ELECTRON PRECIPITATION USING VLF REMOTE SENSING

A DISSERTATION
SUBMITTED TO THE DEPARTMENT OF ELECTRICAL
ENGINEERING
AND THE COMMITTEE ON GRADUATE STUDIES
OF STANFORD UNIVERSITY
IN PARTIAL FULFILLMENT OF THE REQUIREMENTS
FOR THE DEGREE OF
DOCTOR OF PHILOSOPHY

William Bolton Peter
February 2007

I certify that I have read this dissertation and that, in my opinion, it is fully adequate in scope and quality as a dissertation for the degree of Doctor of Philosophy.

_____

(Umran S. Inan)   Principal Adviser

I certify that I have read this dissertation and that, in my opinion, it is fully adequate in scope and quality as a dissertation for the degree of Doctor of Philosophy.

_____

(Martin Walt)

I certify that I have read this dissertation and that, in my opinion, it is fully adequate in scope and quality as a dissertation for the degree of Doctor of Philosophy.

_____

(Philip Scherrer)

Approved for the University Committee on Graduate Studies.

iv

# Abstract

Lightning is pervasive around our planet, with on the average $\sim$40 lightning discharges occurring every second. Lightning-induced electron precipitation (LEP) events are produced by the fraction of the VLF energy radiated by lightning discharges that escapes into the magnetosphere and propagates as a whistler-mode wave. The whistler-mode wave interacts with trapped radiation belt electrons via cyclotron resonance, resulting in pitch angle scattering of the electrons. If the pitch angle of radiation belt electrons at the edge of the loss cone is sufficiently decreased via resonant interaction with the whistler wave field, its lowered mirror height lies in the dense upper atmosphere and the particle is lost (i.e., precipitated) from the radiation belts.

This dissertation examines the detection of lightning-induced energetic electron precipitation via subionospheric Very Low Frequency (VLF) remote sensing. The primary measurement tool used is a distributed set of VLF observing sites, the Holographic Array for Ionospheric/Lightning Research (HAIL), located along the eastern side of the Rocky Mountains in the Central United States. The temporal and spatial signatures of VLF signal perturbations associated with LEP events are characterized for two disparate storms occurring over two four-hour periods. Measurements of the VLF signal perturbations indicate that 90% of the precipitation occurs over a region $8°\pm1°$ and $9°\pm1°$ in latitudinal extent for the two time periods. The measured peak of the precipitation is poleward displaced ($6°45'\pm30'$ and $7°45'\pm30'$ for the two case studies) from the causative discharge. The onset delay and the duration of precipitation steadily increase with increasing $L$-shell, while the signal recovery time is independent of $L$-shell for the LEP events associated with both storms. The causative lightning discharges associated with the two storms were located at different latitudes.

For lightning occurring in the storm at higher latitudes, the associated LEP events are of longer duration and exhibit precipitation in a smaller area displaced less from the causative discharge. The general spatial and temporal signatures are consistent with those expected for LEP events induced by nonducted whistlers.

While the HAIL array accurately captures the spatial and temporal characteristics of the VLF signal perturbations, the VLF signal perturbations have not previously been quantitatively related to the electron precipitation associated with the LEP event. A comparison of the VLF signal perturbations recorded on the HAIL array with a comprehensive model of LEP events allows for the measurement of electron precipitation and ionospheric density enhancement with unprecedented quantitative detail. The model consists of three major components: a test-particle model of gyroresonant whistler-induced electron precipitation; a Monte Carlo simulation of energy deposition into the ionosphere; and a model of VLF subionospheric signal propagation. In the two cases studied, the model calculates peak VLF amplitude and phase perturbations within a factor of three of those observed, which is well within the expected variability of radiation belt flux levels. The model calculates a peak in the precipitation that is poleward displaced $\sim 6°$ from the causative lightning flash, also consistent with observations. The modeled precipitated energy flux ($E > 45$ keV) peaks at $\sim 1 \times 10^{-2}$ [ergs s$^{-1}$ cm$^{-2}$], resulting in a peak loss of $\sim 0.001\%$ from a single flux tube at $L \sim 2.2$, consistent with previous satellite measurements of LEP events.

To quantitatively relate VLF signal perturbations to electron precipitation and the ionospheric density enhancement, several metrics quantify the precipitation and ionospheric disturbance along a given VLF signal path. Metrics quantifying the ionospheric density enhancement ($N_{\mathrm{ILDE}}$) and the electron precipitation ($\Gamma$) are strongly correlated with the VLF signal perturbations calculated by the model. A conversion ratio $\Psi$, relating VLF signal amplitude perturbations ($\Delta A$) to the time-integrated precipitation (100-300 keV) along the VLF path ($\Psi = \Gamma / \Delta A$), of $1.1 \pm 0.2 \times 10^{10}$ [el m$^{-1}$/dB] is suggested for precipitation events of similar location and characteristics to those examined. The total precipitation (100-300 keV) induced by one of the representative LEP events is estimated at $\sim 1.6 \pm 0.3 \times 10^{16}$ electrons, using only the

conversion ratio $\Psi$ and observations of VLF signal perturbations, independent of radiation belt flux levels. The model framework developed is directly applicable to precipitation events and VLF signal paths other than those described, and the application of the methodology described in this dissertation should encourage the use of VLF remote sensing as a measurement tool of radiation belt precipitation loss.

# Acknowledgements

As I put in place the final details for this dissertation, I realize how much I owe to all the people who have contributed directly or indirectly to the completion of this work. I want to take this opportunity to thank all of those whom have helped shape my time here at Stanford.

I would like to express my sincere thanks to my principal advisor, Professor Umran Inan. His limitless energy and passion for his research along with his genuine concern for his students have been an inspiration to me. I deeply appreciate his support and flexibility through the years. I thank my second advisor, Professor Martin Walt, for his approachability, unending helpfulness, patience and friendliness. My thanks go out to the faculty and emeriti that make the VLF group such a wonderful research group, especially Professors Don Carpenter, Timothy Bell and Robert Helliwell. I also appreciate the efforts put forth by Professor Phil Scherrer, who served on both my defense and reading committees, and by Professor Mark Cappelli, chairman of my defense committee. To Shaolan Min and Helen Niu, thank you for your endless contributions that ensure that the VLF group runs so smoothly. I extend my thanks to the many members of the VLF group that have mentored me over the years, notably Doctors Jacob Bortnik, Maria Spasojevic, Mike Chevalier and Robb Moore.

To my parents, Tom and Marjorie, I am grateful for your constant support, encouragement, and love. To my brothers, Max and David, thank you for your friendship, loyalty, and support. I know how lucky I am to have such a wonderful family. I also thank my friends who have kept me sane through the years, especially my good friends and former roommates Dan Johnson and Amit Patel. Finally, I thank my beautiful wife, Kersti Miller. I can never thank her enough for her patience and understanding

through the years. I look forward to spending an exciting and fulfilling life together, starting with a couple years in Melbourne!

# Contents

# List of Tables

# List of Figures

# Chapter 1

# Introduction

## 1.1 Purpose

The purpose of this dissertation is to estimate the precipitation loss of radiation belt electrons into the atmosphere, as induced by pitch-angle scattering with lightning-generated whistlers, through the use of VLF remote sensing. The primary measurement tool we use is the Holographic Array for Ionospheric/Lightning Research (HAIL), a set of VLF receivers located along the eastern side of the Rocky Mountains in the Central United States. The specific areas upon which we focus our attention are: (i) determination of the temporal and spatial characteristics of the VLF perturbations associated with lightning-induced electron precipitation (LEP) events; (ii) development of a framework to model the electron precipitation, resulting ionospheric disturbance, and VLF signal perturbation associated with LEP events; and (iii) development of a methodology by which observations of VLF signal perturbations can be used to quantitatively estimate the ionospheric density enhancement and energetic electron precipitation loss associated with LEP events.

The quantification of electron-radiation belt loss is currently of major scientific interest for modeling the relaxation and quiet-time structure of the belts [*NRCR*, 2003, p.156] and as a prerequisite to understanding the process of acceleration [*Horne*, 2002]. The primary loss process for trapped radiation belt electrons is precipitation resulting from pitch angle scattering of particles via wave-particle interactions, yet the

relative roles of different waves and the $L$-shell regions over which they are dominant are not known [*Abel and Thorne*, 1998a,b]. Both theoretical works [e.g., *Bortnik et al.*, 2003a; *Abel and Thorne*, 1998a,b] and experimental evidence [e.g., *Burgess and Inan*, 1993; *Voss et al.*, 1998] suggest that wave energy injected by lightning discharges are an important contributor to the loss rates of radiation belt particles, especially at lower $L$-shells ($L{\sim}3$). However, the lack of quantitative measurements of lightning-induced precipitation events makes it difficult to confirm the calculations of *Abel and Thorne* [1998a,b] and *Bortnik et al.* [2003a]. Through a comparison of VLF observations of LEP events with a comprehensive model of lightning-induced electron precipitation and the resulting ionospheric disturbance, we examine herein the use of VLF remote sensing to quantitatively measure the precipitating flux associated with two representative LEP events. We demonstrate the use of VLF remote sensing in accurately characterizing precipitation events and resulting ionospheric electron density enhancements. In general, our results are consistent with previous theoretical work [*Lauben et al.*, 1999, 2001]. The analysis described in this dissertation provides a quantitative methodology for assessing the contribution of the LEP process to the loss of radiation belt particles on a global scale.

## 1.2   Scientific Background

### 1.2.1   The Earth's Radiation Belts

The radiation belts consist of high-energy (hot) charged particles trapped by the Earth's geomagnetic field. This hot particle population consists mostly of electrons and protons with energies >100 keV. The radiation belts consist of an inner belt ($1.1{<}L{<}2.5$), an outer belt ($3{<}L{<}9$), and an intermediate region with depleted energetic fluxes known as the "slot-region" ($2.5{<}L{<}3.0$), as illustrated in Figure 1.1. Trapped radiation-belt particles undergo three types of periodic motion: the first is a rapid gyration about the static magnetic field line, the second is a mirroring motion between the northern and southern hemispheres, and the last is the relatively slow drift rotation about the Earth. These periodic motions occur on very different (and
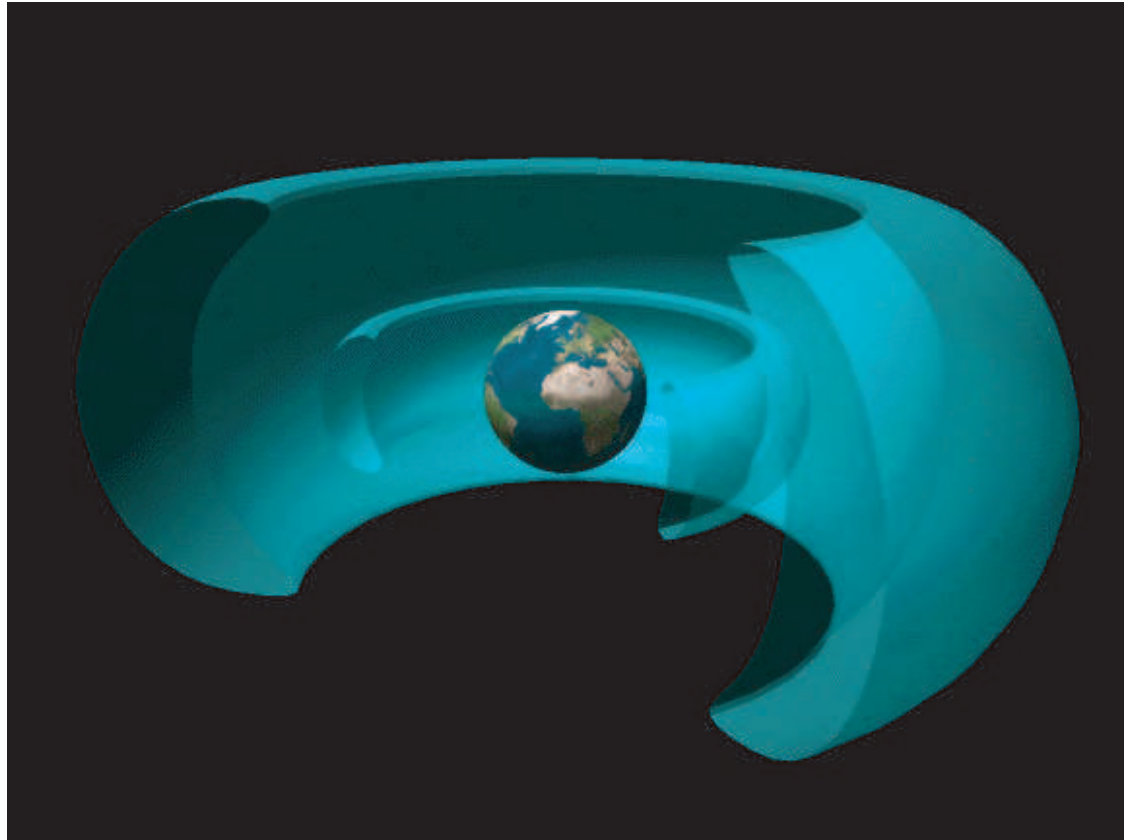
Figure 1.1: Cartoon depicting the Earth's radiation belts, consisting of two toroidal shaped regions of trapped energetic particles surrounding the Earth. Figure taken from *Bortnik* [2004].

thus separable) timescales of $\sim 10^{-3}$ s (cyclotron motion), $\sim 1$ s (bounce motion), and $\sim 10^3$ s (drift motion). The physics of these three periodic motions is discussed in *Walt* [1994, p.36]. In this dissertation, we are concerned primarily with the cyclotron and bounce motions of the Earth's radiation belt electrons.

In the absence of perturbing forces, the trapped energetic particles of the radiation belts would theoretically remain in their stable orbits indefinitely. However, it has been shown that the energetic particle fluxes can undergo dramatic temporal variations. Figure 1.2 shows SAMPEX satellite measurements of energetic flux over the course of 2001. The measurements illustrate several particle injection and energization events and subsequent decays of the particle population.
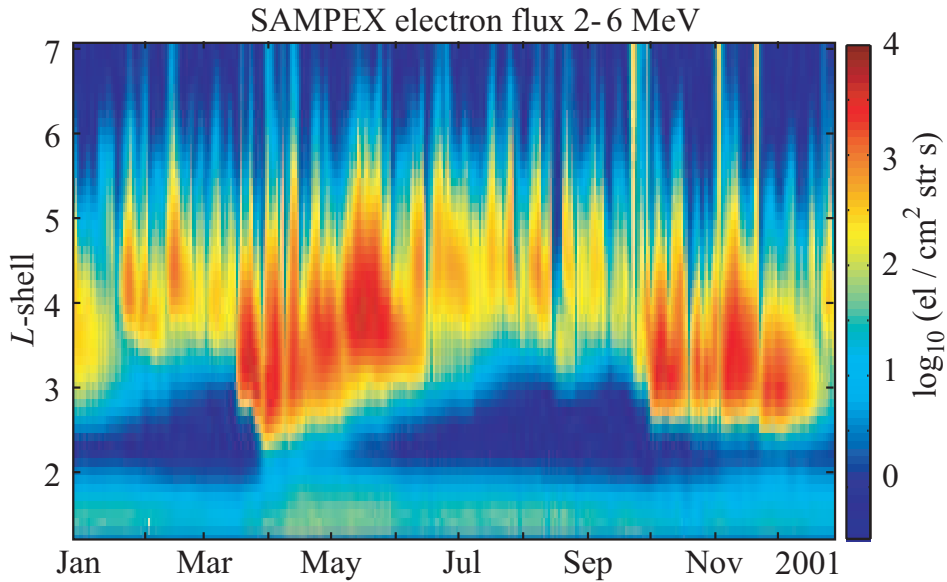
Figure 1.2: SAMPEX satellite measurements of high-energy (2-6 MeV) electron flux over the course of a year (2001), meant to illustrate the variability in radiation belt flux levels. Figure courtesy of *M. Spasojevic* [2006].

Despite nearly fifty years of radiation belt research by the scientific community, the principal source and loss mechanisms are still under investigation [*Walt*, 1994, p.1]. *Walt and MacDonald* [1964] recognized the importance of Coulomb collisions with atmospheric constituents at *L*-shells below 1.25 as a major loss process. However, the loss of radiation belt particles at higher *L*-shells is due primarily to the resonance interaction with whistler mode waves, as first suggested by *Dungey* [1963] and *Cornwall* [1964]. Possible types of VLF whistler mode waves observed in the inner magnetosphere responsible for radiation belt loss are plasmaspheric hiss [*Lyons et al.*, 1972], lightning generated whistler waves [*Helliwell*, 1965], and VLF transmitter signals [e.g., *Vampola*, 1977; *Inan et al.*, 1978]. The origin of some of these waves is uncertain as is the relative contributions to electron loss of each wave type [*Horne*, 2002, and references therein]. The present work focuses on a particular loss process: the precipitation loss of energetic electrons into the atmosphere induced by resonance interaction with nonducted lightning-generated whistlers, including magnetospherically reflecting whistler wave components.
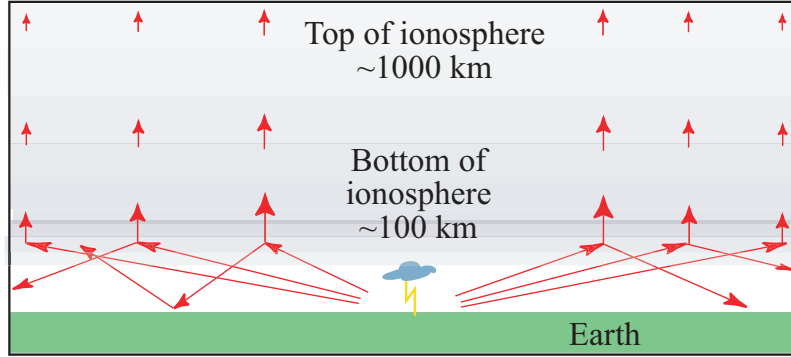
Figure 1.3: Cartoon illustrating the propagation of electromagnetic waves (shown in red) away from the lightning flash through the Earth-ionosphere waveguide. A portion of this energy leaks through the ionosphere and couples into the magnetosphere. Figure modified from *Bortnik* [2004].

## 1.2.2 Lightning-Induced Electron Precipitation (LEP) Events

Lightning is pervasive around our planet, with on the average ~40 lightning discharges occurring every second [*Christian et al.*, 1999]. Lightning-induced electron precipitation (LEP) events are produced by the fraction of the VLF energy radiated by lightning discharges that escapes into the magnetosphere and propagates as a whistler-mode wave (Figure 1.3). A terrestrial cloud-to-ground lightning discharge radiates a broad spectrum of electromagnetic waves, including waves in the extra low frequency (ELF) and very low frequency (VLF) bands, i.e., 300 Hz to 30 kHz [*Uman*, 1984, p.127]. These ELF/VLF waves propagate in the Earth-ionosphere waveguide away from the lightning source. If the ionosphere were an isotropic and unmagnetized plasma, the wave energy would be confined to the Earth-ionosphere waveguide and would not escape upward. However, the presence of the Earth's magnetic field allows a fraction of the wave energy to leak through and propagate to the top of the ionosphere in the so-called whistler mode. There, it couples into the magnetosphere and propagates therein as a whistler mode wave, illuminating a magnetospheric region around the location of the lightning discharge.

Figure 1.4 illustrates the propagation of whistler-mode waves generated by the lightning flash through the magnetosphere. The whistler mode wave travels along ray trajectories (shown in red) away from the Earth, and is guided by gradients

in the Earth's magnetic field strength and direction as well as in the cold electron number density. Past work has distinguished two types of perturbation signatures associated with electron precipitation induced by "ducted" and "nonducted" whistler waves. In the presence of field-aligned ducts of enhanced ionization in the magnetosphere, "ducted" whistler waves propagate along and within the enhanced duct [*Burgess and Inan*, 1993]. Precipitation of energetic electrons can also be caused by obliquely propagating "nonducted" whistlers [*Lauben et al.*, 1999, 2001; *Johnson et al.*, 1999], in which the whistler wave energy can illuminate much larger regions of the radiation belts, precipitating electrons onto ionospheric regions as large as ∼1000 km in extent [*Johnson et al.*, 1999; *Clilverd et al.*, 2002; *Peter and Inan*, 2004]. Nonducted whistlers can also magnetospherically reflect (MR whistlers), resulting in longer wave lifetimes and an increase in total precipitation [*Bortnik et al.*, 2003a]. This dissertation exclusively considers precipitation induced by nonducted, obliquely propagating whistlers, with the whistler wave energy crossing magnetic field lines and migrating across $L$-shells with time, resulting in precipitation over a large region that is displaced in latitude from the lightning flash. Since the lightning discharge injects whistlers over a range of latitudes and longitudes around the source, nonducted whistlers affect regions of the radiation belts of several degrees in invariant latitude and geomagnetic longitude and result in precipitation of electrons over ionospheric regions of ∼1000 km lateral extent [*Lauben et al.*, 1999, 2001]. The additional precipitation due to magnetospherically reflected whistlers can further expand this region of precipitation, especially toward higher $L$-shells [*Bortnik et al.*, 2003a].

The whistler-mode wave interacts with trapped radiation belt electrons (shown in blue) via cyclotron resonance, resulting in pitch angle scattering of the electrons. If the pitch angle of radiation belt electrons at the edge of the loss cone is sufficiently decreased via resonant interaction with the whistler wave field, its lowered mirror height lies in the dense upper atmosphere and the particle is lost from the radiation belts. It is this process that we refer to as electron "precipitation", and such a pitch angle change occurs when the particle experiences the electromagnetic fields of an oblique whistler wave oscillating (and rotating) at approximately the gyration frequency in the particle frame of reference.
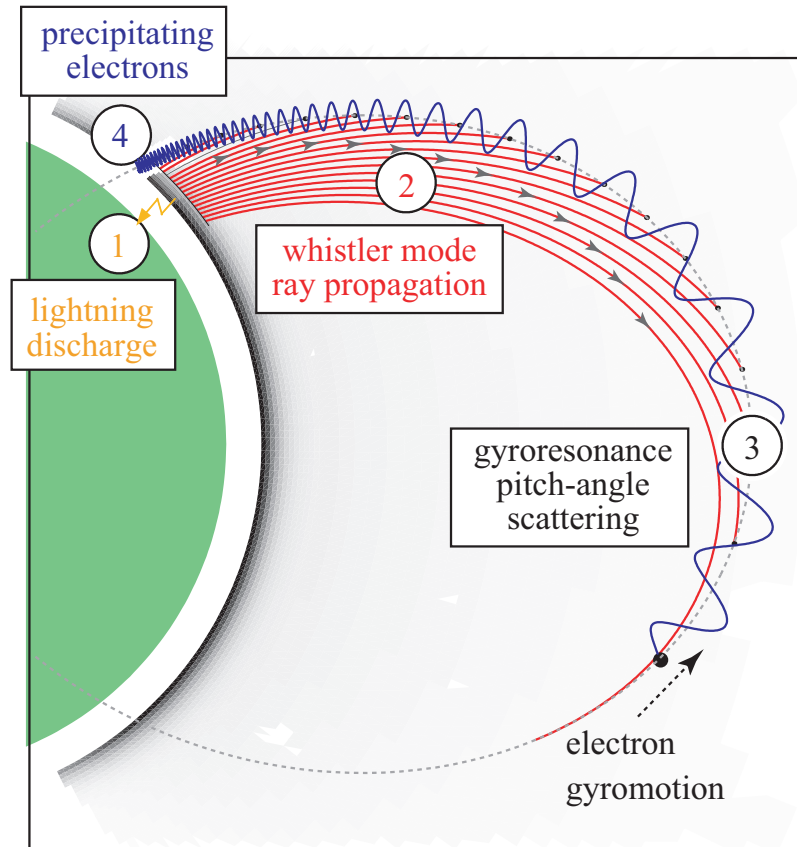
Figure 1.4: Cartoon illustrating the wave-particle interaction process: 1. Lightning discharge occurs; 2. Propagation of the whistler mode wave (shown in red) in the magnetosphere; 3. Wave-particle interaction near the equatorial plane scatters the pitch angle of a fraction of the trapped energetic radiation belt electrons (shown in blue) into the loss cone; 4. Electrons precipitate into the dense upper atmosphere. Figure modified from *Lauben et al.* [2001].

For a more detailed treatment of the propagation of lightning-generated whistler waves and the resonance interaction with energetic electrons, the reader is referred to *Bortnik* [2004] and references therein.

### 1.2.3   VLF Remote Sensing

The ionosphere consists of several electrically neutral ionized layers, commonly referred to as the $D$, $E$, and $F$ regions, which are produced because of the different rates of ionization, attachment, and recombination processes at different altitudes [*Hargreaves*, 1992, Ch. 6]. In this thesis, we restrict our attention to the lowest altitudes of the ionosphere, specifically the altitude range between 40 and 100 km, known as the $D$-region (often dubbed the "ignorosphere" due to the difficulty of systematic measurements [*Sechrist*, 1974]). Furthermore, we exclusively consider ionospheric disturbances which occur during nighttime, when the ambient ionization levels are substantially lower and the ionospheric density enhancements associated with LEP events result in larger fractional changes in the overall ionospheric density, and hence the ionospheric disturbances are easier to detect via VLF remote sensing. VLF remote sensing is uniquely suited for the investigation of the nighttime $D$-region because of the sensitivity of subionospherically propagating VLF signals to changes in lower ionospheric conductivity.

Very Low Frequency (VLF) radio waves ($\sim$3 to 30 kHz) are guided by the spherical waveguide formed between the Earth's surface and the lower ionosphere (referred to as the Earth-ionosphere waveguide), and can efficiently propagate to long distances. The amplitude and phase of the subionospherically propagating VLF signals depend sensitively on the electrical conductivities of the lower ionosphere and ground. Hence, disturbances to the lower ionospheric conductivity change the amplitude and/or phase of VLF transmitter signals propagating in the Earth-ionosphere waveguide on Great Circle Paths (GCPs) that pass through or near the localized disturbance [*Poulsen et al.*, 1993b].

Precipitating energetic electrons (induced by lightning-generated whistlers or other sources) deposit energy into the atmosphere, and through secondary ionization alter
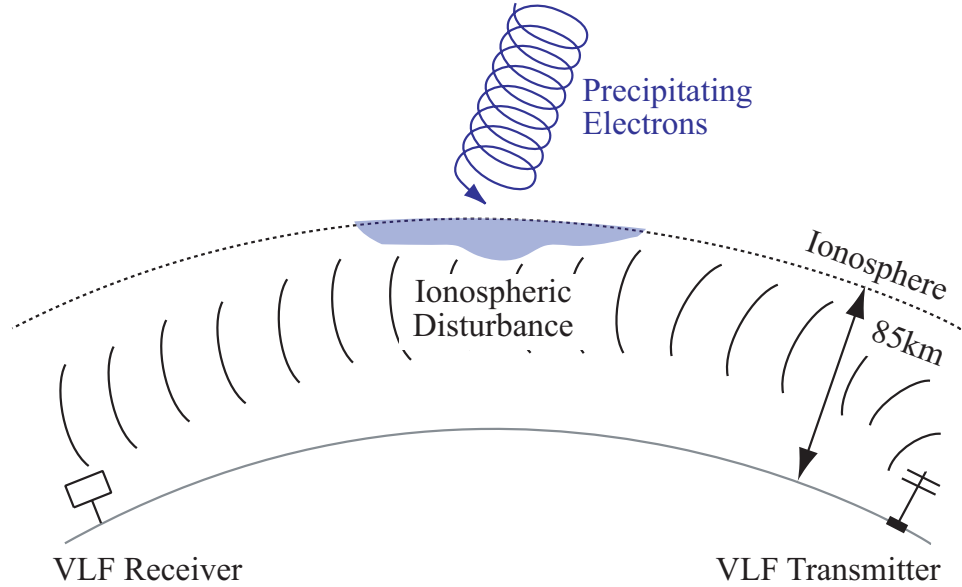
Figure 1.5: Precipitating electrons (shown in blue) produce secondary ionization, which in turn changes the electrical conductivity of the upper boundary of the Earth-ionosphere waveguide and perturbs the VLF wave propagating underneath.

the electron density and conductivity of the lower ionosphere (Figure 1.5). This ionospheric density enhancement in turn perturbs subionospheric VLF signals propagating on GCPs that pass through or near the disturbance. The amplitude and phase of VLF transmitter signals observed at any point can thus be used to measure the spatial and temporal characteristics of localized disturbances in the lower ionosphere, a technique referred to as subionospheric VLF remote sensing.

The subject of this thesis is the use of measurements of VLF signals propagating in the Earth-ionosphere waveguide to quantitatively estimate ionospheric disturbances and radiation belt particle precipitation associated with lightning-induced electron precipitation events.

**The Holographic Array for Ionospheric/Lightning research (HAIL)**

The Holographic Array for Ionospheric/Lightning research (HAIL) consists of nine separate VLF receivers spaced ~130 km apart along the eastern side of the "Front Range" of the Rocky Mountains in the Central United States (Figure 1.6). The HAIL
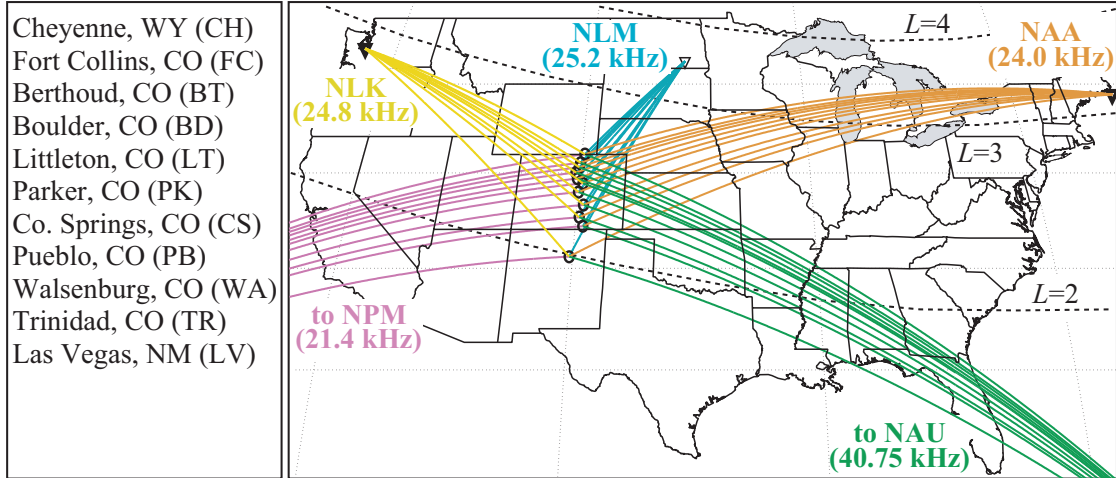
Figure 1.6: Holographic Array for Ionospheric/Lightning Research (HAIL). The location of the HAIL VLF receivers, with the Great Circle Paths (GCPs) of the subionospherically propagating VLF signals shown as solid lines. The names of the receiver locations (top to bottom corresponding to North to South) are shown in the box to the left. Note that the configuration of HAIL sites shown is for March 2001. The configuration has since been slightly modified.

array continuously monitors the amplitude and phase of coherent and subionospherically propagating VLF signals from transmitters operated by the United States Navy in Washington (NLK at 24.8 kHz), Maine (NAA at 24.0 kHz), North Dakota (NLM at 25.2 kHz), Hawaii (NPM at 21.4 kHz) and Puerto Rico (NAU at 40.75 kHz). This dissertation focuses only on the recorded data from the NAA and NAU transmitters.

Each VLF receiver is deployed at a rural high school or community college with Internet access, so that the data can be brought back to Stanford without delay and the receiver can be controlled remotely. Data are acquired daily from 01:00 to 13:00 UT, when the GCPs between transmitter and receiver are partially or wholly in the nighttime sector. A 1.7 x 1.7 m$^2$ magnetic loop antenna connected to a preamplifier is used to detect the VLF signal at all receivers. The broadband VLF signal is bandpass filtered to the range of 9-45 kHz and then is digitized at a rate of 100 kHz with 16-bit resolution, with triggers provided by GPS timing. Each receiver digitally down-converts the individual VLF transmitter signals, demodulates the Minimum Shift Keying (MSK) modulation, and records the demodulated amplitude and phase

with 20 ms resolution. The data is then sent to Stanford University each morning automatically via FTP.

For a more detailed description of the HAIL array and the VLF receivers, the reader is referred to *Johnson* [2000].

## 1.3 VLF Signatures of LEP Events

This dissertation concerns observations of VLF signal perturbations recorded by HAIL that are associated with lightning-induced electron precipitation events. Figure 1.7 shows an example LEP event as detected on a single VLF signal. The map shows the GCP of the subionospherically propagating VLF wave between the NAU VLF transmitter and one of the HAIL VLF receivers located near Parker, Colorado. A hypothetical region (based on *Johnson et al.* [1999]) of ionospheric disturbance associated with the LEP event is superimposed. Notice that the precipitation is poleward displaced from the lightning flash, due to the oblique propagation of the nonducted whistler wave across magnetic field lines. Below the map is a five-minute snapshot of the NAU signal amplitude recorded at Parker, showing the characteristic signature of a LEP event in VLF data: a sharp change in amplitude followed by a slower recovery as the lower ionosphere returns to its ambient state.

Zooming in on the LEP event onset, we see that the sharp amplitude perturbation occurs over a period of about one second, corresponding to the duration of the LEP burst, or to the time over which significant precipitation occurs. The impulse in the amplitude data is referred to as a "spheric" and corresponds to the VLF energy generated by the lightning flash that propagates directly to the VLF receiver through the Earth-ionosphere waveguide. This broadband impulse has energy across the entire VLF range, including the ~400 Hz band around the VLF transmitter frequency used to measure the amplitude of the VLF transmitter signal, thus appearing as an impulse in the "narrowband" transmitter signal. The spheric defines the time of the lightning flash, which is correlated with a specific lightning flash in the National Lightning Detection Network (NLDN) data. The NLDN network provides the timing, location, and peak current of cloud-to-ground (CG) lightning discharges with one-ms resolution

across the continental United States [*Cummins et al.*, 1998]. In this connection, it is useful to note that the propagation of the spheric from the lightning location to the receiver occurs nearly at the speed of light, so that this propagation delay is negligible compared to the 20-ms resolution of the VLF data. Notice the delay between the causative lightning flash (as recorded by the spheric) and the onset of the amplitude perturbation. This "onset delay" roughly corresponds to the time it takes for the whistler wave energy generated by the lightning flash to propagate through the magnetosphere (at a relatively slow whistler-mode speed of $0.1c$ to $0.01c$), interact with the radiation belt electrons, and for the electrons to travel along the Earth's magnetic field lines down to the ionosphere where they precipitate.

### 1.3.1   LEP Event Measurables

In typical LEP events, the measurable features (Table 1.1) of VLF signal perturbations consist of:

1. *Event Perturbation Magnitude* ($\Delta A$) of the VLF signal refers to the change in amplitude, measured in dB, from the ambient levels prior to the event, to the maximum (or minimum) levels reached during the event (Figure 1.7c). The associated phase change $\Delta\phi$ is also measured.

2. *Onset Delay* ($\Delta t$) refers to the time delay between the causative lightning discharge, as recorded in NLDN data and time-correlated spherics in the HAIL VLF data, and the onset of the event (Figure 1.7c). The impulsive spheric associated with the lightning discharge contains energy over a wide range of frequencies and is often visible as a sharp peak in many of the narrowband channels monitored. For the purposes of this dissertation, the onset of the event is defined as the time at which the amplitude has changed by 10% of the final perturbation magnitude ($\Delta A$). With the onset time defined in this manner, the onset delay measurement is relatively independent of the magnitude of the perturbation.
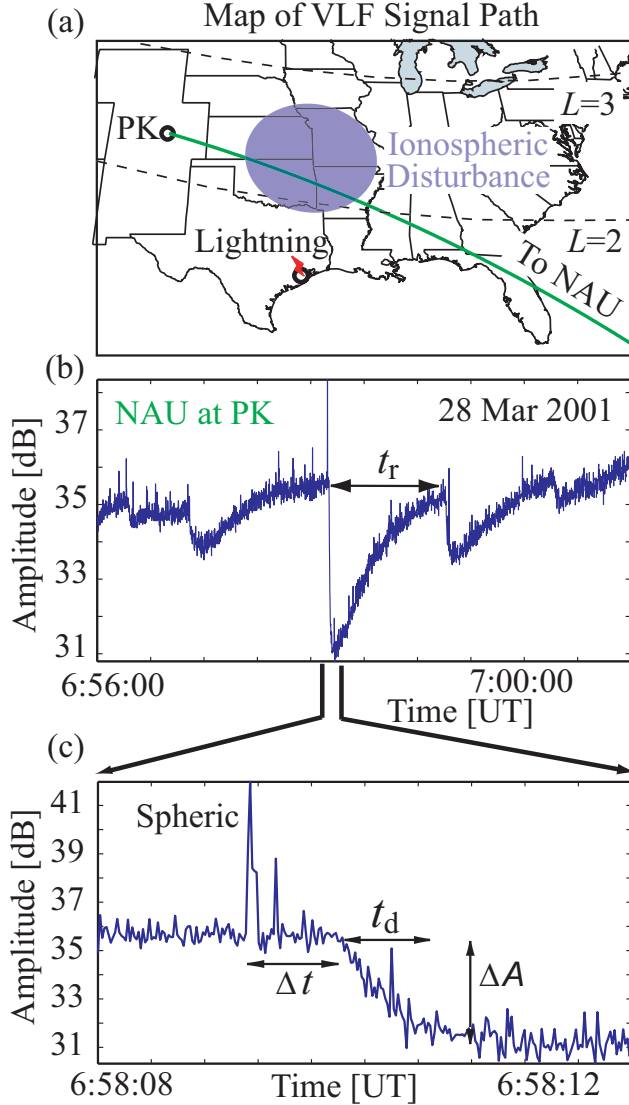
Figure 1.7: An example LEP event (∼6:58:09). (a) Great circle path (GCP) of the subionospherically propagating VLF wave, with a hypothetical region of ionospheric disturbance superimposed. The change in the conductivity of the *D*-region of the ionosphere leads to the perturbation of the VLF signal propagating underneath. (b) A five-minute snapshot of the received VLF signal for a typical LEP event, showing one of the measurable temporal features, namely the *recovery time* ($t_r$). The panel shows the amplitude of the received signal in dB. (c) A zoom-in of the same event showing a five second snapshot with the other three measurable temporal features, namely event *perturbation magnitude* ($\Delta A$), *onset delay* ($\Delta t$), and *onset duration* ($t_d$).

Table 1.1: Measurables of LEP Events

| Measurable | Range |
|---|---|
| Perturbation Magnitude | $0.5\,\mathrm{dB} \leq |\Delta A| \geq 10\,\mathrm{dB}$ |
| Onset Delay | $0.2\,\mathrm{s} \leq \Delta t \leq 2.5\,\mathrm{s}$ |
| Onset Duration | $0.5\,\mathrm{s} \leq t_\mathrm{d} \leq 5\,\mathrm{s}$ |
| Recovery Time | $10\,\mathrm{s} \leq t_\mathrm{r} \leq 100\,\mathrm{s}$ |

3. *Onset Duration* $(t_\mathrm{d})$ refers to the length of time over which the signal amplitude continues to change up to its maximum value (either negative or positive), and corresponds to the temporal duration of the precipitation burst (Figure 1.7c). The onset duration is defined as the time between the onset of the event and the end of the increase in perturbation magnitude, the latter being defined as the point at which the signal amplitude change has reached 90% of its full value $(\Delta A)$. The measurement of the onset duration is also relatively independent of the magnitude of the perturbation.

4. *Recovery Time* $(t_\mathrm{r})$ is the time at which the signal recovers back to the amplitude it would have exhibited in the absence of the perturbation, and it signifies the time at which the ionosphere recovers back to its ambient profile (Figure 1.7b). For the purposes of this dissertation, recovery time is defined as the time between the time of maximum perturbation and the time when the amplitude has returned to within 10% of the value it would have had in the absence of the event, so that it also is relatively independent of the magnitude of the perturbation. If the recovery is interrupted by another event, it is assumed that the event would have recovered at a similar rate, and the typically exponential recovery of the signal is extrapolated to estimate the recovery time.

## 1.3.2   Differential Onset Delay

The multiple VLF receivers of the HAIL array can be used to measure the spatial and temporal characteristics of ionospheric disturbances associated with lightning-induced electron precipitation. Figure 1.8 shows an example LEP event as detected on multiple paths of the HAIL array. The top panel shows the NAA signal observed at
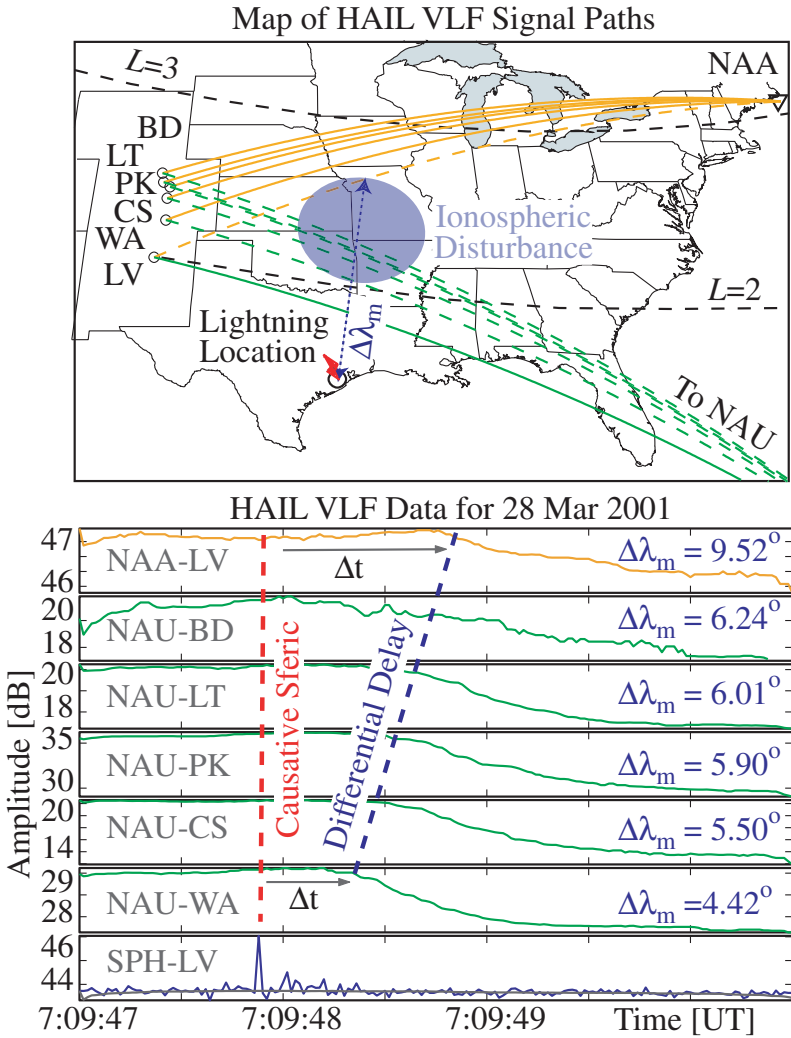
Figure 1.8: An example LEP event ($\sim$7:09:48) shows a differential onset delay as measured on the different VLF paths spanning the HAIL array. (Top) Map showing the great circle paths (GCPs) of propagating VLF waves monitored by the HAIL array, with the presumed ionospheric disturbance region superimposed. The dashed lines denote the GCPs on which the propagating signals are disturbed, while no measurable perturbations are detected on the signals propagating along the paths denoted by solid lines. The dark blue dashed line denotes the latitudinal displacement ($\Delta\lambda_m$) of the GCP from the lightning flash, as listed in the panel below for each signal. (Bottom) A 3.5 second snapshot of each of the perturbed signals, shown in amplitude (dB). Also denoted is the onset delay for each signal. The increase in onset delay with latitude is termed "differential delay".

LV, shown in orange. The panels below show in green color the signals corresponding to paths from the NAU transmitter to the different HAIL receiver locations. Top to bottom corresponds to north to south GCPs. The bottommost signal is included only to show the timing of the lightning flash (causative spheric). The lateral distance $(\Delta\lambda_{\mathrm{m}})$, in degrees latitude, between the flash location $(30°11'\mathrm{N}, 95°44'\mathrm{W})$ and the point of crossing of the GCP and the geomagnetic longitude of the causative flash is shown for each signal. This coordinate of "latitudinal distance" between the GCP and the lightning flash is used throughout this dissertation.

The onset delay $(\Delta t)$ is also indicated for each signal. Typical VLF signatures associated with nonducted whistler-induced electron precipitation exhibit an increase in onset delay with latitude [*Johnson et al.*, 1999]. This is due to the oblique propagation of the whistler mode wave across magnetic field lines resulting in the whistler wave packet reaching the equatorial wave-particle interaction region later in time at higher $L$-shells and a "splashing" down of precipitation. The signals arriving over the corresponding GCPs thus exhibit the event onset at increasingly later times with increasing latitude of the GCP. The differences in onset delay across the receiver sites at which the event is visible are referred to as "differential delay". This difference in onset delays is the temporal signature that distinguishes the so-called nonducted LEP events produced by an obliquely propagating (nonducted) whistler from other events such as those produced by ducted whistlers.

## 1.4   Review of Past Work

Due to the broad scope of this dissertation, the review of past work is described under three related topics. Only the most relevant works are mentioned, with special emphasis given to the most recent analyses.

### 1.4.1   Whistler-Induced Electron Precipitation

*Voss et al.* [1984] documented multiple strong ($\sim100\times$ background) transient ($\sim1$ s) enhancements in precipitating energetic electron flux with one-to-one associations

with lightning-generated whistlers, establishing LEP events as both detectable and significant. While the LEP process has been observed on satellites [*Voss et al.*, 1998; *Blake et al.*, 2001], its transient/localized nature render such observations difficult. Conversely, hundreds of LEP bursts have been measured on a given night with VLF methods [*Lev-Tov et al.*, 1995; *Rodger et al.*, 2002; *Peter and Inan*, 2004]. Both before and after the first satellite observations of LEP events, subionospheric VLF signatures of LEP events were detected and extensively studied [i.e., *Helliwell et al.*, 1973; *Carpenter and LaBelle*, 1982; *Inan et al.*, 1985, 1988a,b; *Inan and Carpenter*, 1986; *Burgess and Inan*, 1993].

Modeling of whistler-mode wave-induced electron precipitation has followed two main approaches. The first is the diffusion (or "Fokker-Planck") approach, which calculates long-term changes in the particle population by assuming that a broad band of incoherent waves perturb trapped energetic electrons, causing a violation of the first adiabatic invariant and pitch angle diffusion. This approach was originally applied to plasmaspheric hiss [i.e., *Roberts*, 1969; *Lyons et al.*, 1971, 1972; *Lyons and Thorne*, 1973] and subsequently extended to include wave-particle interactions involving other types of waves, such as lightning-generated whistlers and VLF transmitter signals [i.e., *Abel and Thorne*, 1998a,b] in studying the equilibrium structure of the radiation belts.

The second approach to modeling whistler-mode wave-induced electron precipitation is the test particle approach, which is based on the integration of the equations of motion for individual test particles as they traverse the whistler wave packet [*Inan et al.*, 1978, 1982]. The behavior of the entire distribution function is based on these sample test particles, paying particular attention to the fraction of particles scattered into the loss cone [*Bortnik*, 2004]. Efforts to model bursts of precipitation induced by lightning-generated whistler waves originally focused on "ducted" whistlers, with the wave energy propagating parallel to the magnetic field line during its traverse through the magnetosphere [*Inan et al.*, 1978, 1985a, 1989; *Chang and Inan*, 1983, 1985a,b]. However, precipitation induced by nonducted whistlers was eventually considered, and in an unusual juxtaposition of theoretical predictions [*Lauben et al.*, 1999] and experimental observation [*Johnson et al.*, 1999], it was realized that such

precipitation occurs commonly and that some of the observations previously inter-preted as being due to ducted wave-induced precipitation may well have been due to nonducted waves.  Observations of VLF signal perturbations [*Johnson et al.*, 1999; *Clilverd et al.*, 2002; *Peter and Inan*, 2004] indeed show that the spatial extent of the ionospheric disturbance is often inconsistent with the observed dimensions of whistler ducts [e.g., *Angerami*, 1970].  It is now believed that the far greater portion of whistler wave energy entering vast volumes of the magnetosphere propagates in the oblique "nonducted" mode, with non-zero wave normal and ray path angles with respect to the Earth's field lines [*Lauben*, 1998, p.3].

The basic equations of motion for oblique-mode gyroresonance were developed by *Bell* [1984] and implemented by *Jasna et al.* [1992]; *Jasna* [1993]; and *Ristic'-Djurovic' et al.* [1998], the latter which treats the single pass interaction of an ensemble of energetic electrons through fixed-frequency (monochromatic) steady-state oblique-mode wave fields.  This treatment was extended to transient broadband oblique waves in *Lauben et al.* [1999, 2001], in which only the first traverse of the magnetic equator (a so-called "hop") of the oblique whistler was considered.  The *Lauben et al.* [1999, 2001] work led to the predictions of latitude dependent onset delays and large extended precipitation regions which were experimentally confirmed in the work of *Johnson et al.* [1999] and *Peter and Inan* [2004].  The most current model of nonducted whistler-induced precipitation was developed in *Bortnik et al.* [2003a,b, 2006a,b], in which multiple passes (due to magnetospheric reflection) of the whistler wave energy through the magnetic equator are also considered, and it is this model that is used in this dissertation (described in Section 3.3.1).

It should be noted that the bulk of the precipitation induced by nonducted whistlers are in fact due to the first hop, with the magnetospherically reflected com-ponents only affecting the duration of the event onset.  The important properties of onset delay and peak precipitation flux are solely determined by the first hop, so that most of the theoretical calculations against which we compare our data in this dissertation could just as well have been obtained with the *Lauben et al.* [1999, 2001] model.

## 1.4.2  VLF Signal Propagation

Using VLF techniques, studies have been made of *D*-region processes involving solar flares [*Bracewell and Straker*, 1949], meteor showers [*Chilton*, 1961], nuclear detonations [*Zmuda et al.*, 1963], auroral enhancements [*Cummer et al.*, 1997; *Peter et al.*, 2006], and gamma ray bursts and flares of extraterrestrial origin [*Fishman and Inan*, 1988; *Inan et al.*, 1999]. Several methods have been applied to modeling VLF signal propagation in the Earth-ionosphere waveguide. For shorter VLF signal paths a ray optics approach [*Morfitt et al.*, 1976] is used, with the propagation of the VLF signal analyzed in terms of rays that satisfy the boundary conditions at all points along the propagation path. The ray optics approach is not suited for longer (>500 km) paths, due to the need to consider an unreasonably large number of discrete ray paths [*Johnson*, 2000]. The second major approach is the representation of the propagating VLF signal as a superposition of discrete waveguide modes. Single waveguide mode analytical solutions have been used to interpret variations of narrowband VLF transmitter signals propagating on long (>6000 km) and primarily sea-based paths [*Inan and Carpenter*, 1987; *Poulsen et al.*, 1990], but are not useful for the relatively short (∼3000 km) and primarily land-based paths considered in this work. Based upon a mathematical formulation of the waveguide mode approach [*Budden*, 1962], a two-dimensional model was developed at the Naval Research and Development Laboratory, known as the Long Wave Propagation Capability (LWPC) code [*Feguson and Snyder*, 1987, and references therein]. *Poulsen et al.* [1990] and *Poulsen et al.* [1993a,b] extended the two-dimensional LWPC model to include effects of waveguide parameter variations in the dimension transverse to the direction of propagation to model cases in which a localized ionospheric disturbance occurs on or near the propagation path.

More recently, a Finite-Difference Frequency Domain (FDFD) model was developed to simulate the propagation of electromagnetic waves in a magnetized plasma [*Chevalier et al.*, 2007b]. For an overview of FDFD modeling techniques, the reader is referred to *Zhao et al.* [2002]. This FDFD model was then applied to long (>1000 km) VLF signal propagation paths in *Chevalier and Inan* [2006], and the modeling of VLF signal propagation used in this dissertation is based on the application of this

new code (see Section 3.3.3).

### 1.4.3   VLF Signatures of LEP Events

The first observations of VLF signal perturbations associated with lightning-induced electron precipitation was made by Stanford operator Mike Trimpi while monitoring VLF transmitter signals in Antarctica [*Helliwell et al.*, 1973]. Following this observation, the use of subionospheric VLF signals to detect transient perturbations of the upper atmosphere associated with lightning-induced electron precipitation (LEP) events was continued in such works as *Inan et al.* [1985, 1988a, 1990], *Carpenter et al.* [1984], *Burgess and Inan* [1993] and references therein. This early work focused on "ducted" LEP events of smaller (<100 km) spatial extent. The first observations of precipitation induced by nonducted whistlers was realized by *Johnson et al.* [1999], who observed latitude dependent onset delays consistent with theoretical predictions [*Lauben et al.*, 1999]. Other VLF observations [*Rodger et al.*, 2002; *Clilverd et al.*, 2002, 2004; *Peter and Inan*, 2004] have since confirmed the precipitation over large perturbation regions (∼1000 km), consistent with "nonducted" whistler-induced precipitation.

Despite the extensive work describing the VLF signatures of LEP events, there has been little past work on the use of these VLF signal perturbations to quantitatively estimate electron precipitation induced by lightning-generated whistlers. The most relevant work in this area is Chapter 4 of *Johnson* [2000], in which the precipitating electron flux and spectra as determined by a nonducted whistler-induced precipitation model [*Lauben et al.*, 1999] was used as an input to a Monte Carlo simulation model of energy deposition [*Lehtinen et al.*, 2001] to determine the ionization enhancement profile associated with the LEP event. A 2D LWPC model of VLF signal propagation [*Feguson and Snyder*, 1987] was then used to calculate the disturbed amplitude and phase of VLF signals propagating on GCPs through the disturbed region, with the calculated VLF signal perturbations compared directly to the observations made on HAIL. It was estimated that a single 15 kA peak current lightning discharge precipitated electrons with a total energy of 1.8 MJ. However, no attempt was made

to quantitatively relate the VLF signal perturbations to the associated ionospheric disturbance or electron precipitation along the signal path. Also relevant is the work of *Rodger et al.* [2004], which modeled satellite and ground-based observations of electron precipitation event onset and decay and its effects in the ionosphere by examining associated VLF signal perturbations.

### 1.4.4   The Role of LEP in Radiation Belt Loss

The role of MR whistlers in the loss-rate of energetic radiation-belt electrons was estimated in *Abel and Thorne* [1998a,b], who calculated the scattering rates and electron lifetimes due to plasmaspheric hiss, coulomb interactions, lightning-generated whistlers, and VLF transmitters. For the lightning-generated MR whistlers, *Abel and Thorne* [1998a,b] assumed a constant frequency band of $f=4.5\pm2$ kHz and a constant wave normal angle of $\Theta\sim45°\pm22.5°$ throughout the magnetosphere. They concluded that lightning-generated MR whistlers generally dominated 100 to 300 keV electron lifetimes from $2<L<3$. *Bortnik et al.* [2003a] provided a first-order estimate of the distribution of MR whistler wave energy as a function of $L$-shell, using ray tracing and incorporating Landau damping of the whistler wave. The results indicated that MR whistler energy deposition is maximized at the location of the slot region, suggesting that MR whistlers may play a more significant role than previously assumed in the formation and maintenance of the slot region. Also relevant is the work of *Clilverd et al.* [2004], which examined the dependence of precipitation fluxes arising from whistler-induced radiation belt losses on the strength of the return stroke current of the associated lightning. Four days of lightning activity occurring near the east coast of North America were compared with observations of VLF signal perturbations observed in the conjugate region of the southern hemisphere ($2<L<2.5$). The range of observed VLF amplitude perturbations (10 to 35 dB) was associated with precipitation bursts with energy fluxes estimated at $0.4$–$6.5\times10^{-3}$ ergs cm$^{-2}$ s$^{-1}$, based on the modeling work of *Rodger et al.* [2004].

Lightning may additionally contribute to electron losses via generation of plasmaspheric hiss and drift loss cone enhancements. *Green et al.* [2005] examined three

years of plasma wave observations from the Dynamics Explorer and the Imager for Magnetopause-to-Aurora Global Exploration spacecraft and provided evidence of an association between lightning and plasmaspheric hiss. Lightning as an embryonic source of hiss was first recognized by *Sonwalkar and Inan* [1989] based on direct observations of hiss bursts following whistlers on the Dynamics Explorer 1 satellite. *Draganov et al.* [1992] used ray-tracing to demonstrate the evolution of MR whistler energy into hiss-like spectra. In view of the recognized role of plasmaspheric hiss in pitch angle scattering of radiation belt electrons [*Lyons et al.*, 1972; *Abel and Thorne*, 1998a,b], quantifying the degree to which lightning is an embryonic source of hiss is at the forefront of understanding the distribution and dynamics of the Earth's inner radiation belt and slot regions. Furthermore, drift loss cone enhancements of >150 keV and >500 keV electrons measured on the SAMPEX spacecraft, in association with thunderstorm activity, were interpreted as precipitation driven by MR whistlers [*Blake et al.*, 2001]. Neither lightning-generated plasmaspheric hiss nor drift loss cone enhancements due to MR whistlers are considered in this dissertation.

## 1.5   Thesis Organization

The present work is organized into 6 chapters:

Chapter 1 (the current chapter) introduces lightning-induced electron precipitation (LEP) events, VLF remote sensing, and the detection of LEP events using the Holographic Array for Ionospheric/Lightning Research (HAIL). This chapter also provides the context of LEP events in terms of radiation belt research, and reviews previous related research.

In Chapter 2 we describe the use of HAIL to measure the temporal and spatial characteristics of VLF signal perturbations associated with LEP events. A statistical analysis of two nights of LEP event activity is presented, as well as a discussion of the variability in occurrence rates.

In Chapter 3 we detail a comprehensive model of lightning-induced electron precipitation. The model is made up of three major components: a model of whistler-induced electron precipitation [*Bortnik et al.*, 2006a]; a Monte Carlo simulation of

the energy deposition into the ionosphere resulting from the calculated precipitation flux [*Lehtinen et al.*, 2001]; and a model of VLF subionospheric signal propagation that takes into account the disturbed ionospheric density profiles [*Chevalier and Inan*, 2006].

In Chapter 4 we apply the model framework to two representative LEP events and compare the model calculations directly to the observations recorded on HAIL.

In Chapter 5 the VLF signal perturbations are quantitatively related to the precipitation flux and ionospheric density enhancement associated with the LEP event through the use of metrics. An estimate of the total precipitation induced by a representative LEP event is calculated using the VLF signal perturbations recorded on HAIL.

Chapter 6 summarizes the results presented in Chapters 2 to 5, compares these results with those of related research, and concludes with a discussion of future extensions to this work and the use of the proposed methodology for other types of precipitation events.

## 1.6 Contributions of this Research

The major contributions of this research can be summarized as follows:

1. Quantification of the spatial and temporal characteristics of VLF perturbations associated with nonducted LEP events.

2. Development of a framework to model the effects of electron precipitation associated with nonducted LEP events on subionospheric VLF signals.

3. Use of VLF remote sensing to quantitatively estimate the electron precipitation and ionospheric density enhancement associated with nonducted LEP events.

This page intentionally left blank.

# Chapter 2

# VLF Signatures of LEP events

## 2.1  Introduction

In this section we describe a statistical examination of LEP events as detected by the HAIL array during March 2001. We examine in detail two nights of LEP event activity, 24 and 28 March 2001, determining the spatial and temporal characteristics of the VLF signal perturbations associated with the LEP events. We will also discuss the variability in occurrence rates of LEP events, and argue that the precipitation induced by a given lightning flash is highly sensitive to the trapped radiation belt flux levels near the loss cone. The results of this chapter are published in *Peter and Inan* [2004].

## 2.2  LEP Events During March 2001

During March 2001, an unusually large number of LEP events are captured by the HAIL array. While the signal amplitudes exhibit significant variations over various time scales, the VLF signatures of LEP events are identified on the basis of previously established criteria [*Johnson et al.*, 1999], including a short onset duration (0.5 to 5 s) followed by a slower recovery (10 to 100 s). The onset delay itself is found to vary significantly, depending on the latitudinal distance between the GCP of the perturbed VLF signal and the causative lightning flash. The onset delay is required to be greater

than 0.2 seconds to ensure that other VLF events, known as Early/Fast events [*Inan et al.*, 1995], are not inadvertently included in the data set. For ease of identification and accuracy in the presence of other fluctuations in signal amplitude, only events with perturbation magnitudes larger than 0.5 dB are considered. While our choice of a threshold of 0.5 dB excludes smaller LEP events from the study, it allows for a more reliable measurement of the different temporal features for the events that are included. In this context, it should be noted that both the duration and recovery time measurables require measurement changes of 10% of the perturbation magnitude, or a minimum of 0.05 dB; only slightly larger than the inherent ambient noise for the recorded signal amplitudes.

Data from the HAIL array are available during the entire month of March 2001, with at least five receivers operating on each day of the month. The recorded signals (from NAA and NAU) for each day are examined for VLF signatures of LEP events that met the criteria specified above. The number of LEP events on each day of March 2001 is shown in Figure 2.1a. As mentioned above, only those events with perturbation magnitudes greater than 0.5 dB are considered as LEP events in this study. As the occurrence of lightning discharges is a prerequisite for lightning-induced electron precipitation, Figure 2.1b shows the number of cloud-to-ground (CG) lightning discharges recorded by the NLDN network occurring from 30°–42°N and 70°–105°W, an area generally associated with producing LEP events monitored by the HAIL array. Due to the poleward displacement of the precipitation region from the causative discharge, this region is chosen to include areas distant from the GCPs of the propagating VLF signals. The exact dimensions of the region are chosen based on our familiarity with HAIL data and the knowledge of the regions of lightning activity which typically result in producing LEP events detectable on the HAIL array. Possible reasons for the small numbers of LEP events compared to the number of CG discharges recorded by the NLDN network is discussed in the following section.

The number of LEP events on any given day is found to be highly variable, with the latter days of this particular month tending to exhibit a higher number of occurrences of events (Figure 2.1a). The occurrence of a lower number of LEP events on the $26^{th}$ and $27^{th}$ corresponds to a period when few lightning discharges occur in
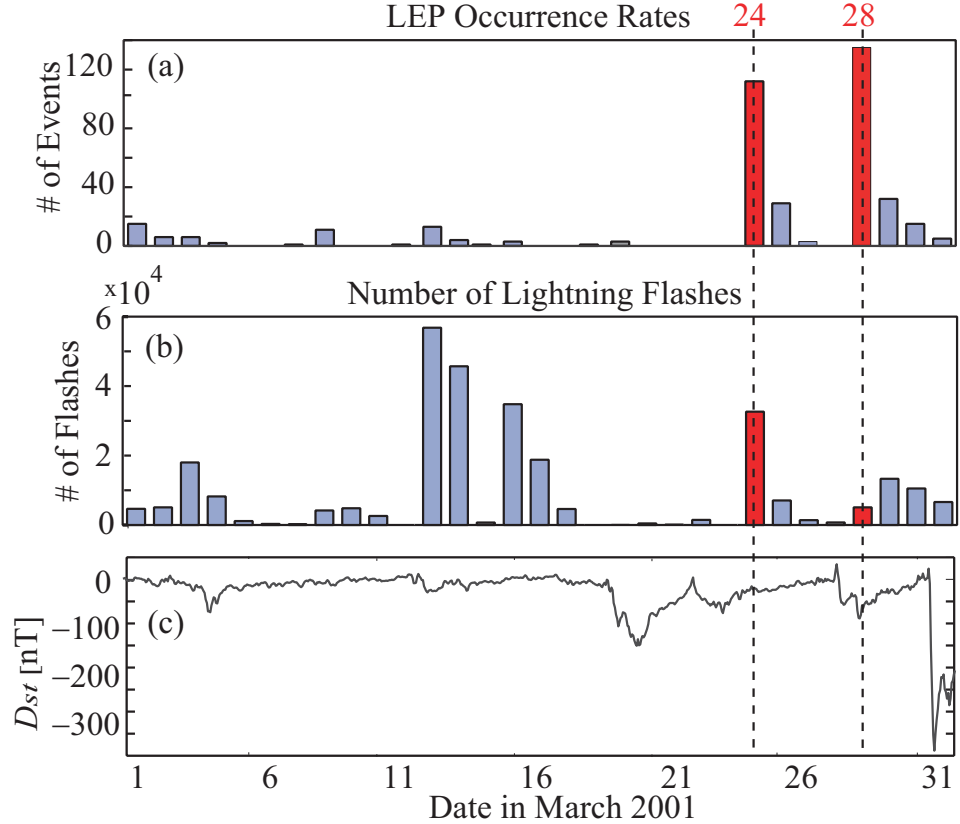
Figure 2.1: LEP events during March 2001. (a) The number of LEP events detected on the HAIL array each night during March 2001. (b) The number of cloud-to-ground (CG) discharges recorded by NLDN from 01:00 to 13:00 UT on each day of March 2001, occurring from 30°–42°N and 70°–105°W, an area generally associated with producing LEP events monitored by the HAIL array. (c) Geomagnetic activity ($Dst$) index for the month of March 2001.

the region. However, a relatively small number of LEP events occur on earlier days (the $12^{th}$, $13^{th}$, $15^{th}$ and $16^{th}$) despite the large number of lightning flashes. The lack of correlation between Figures 2.1a and 2.1b suggest that factors other than CG lightning occurrence significantly influence the occurrence rates of LEP events.

To more clearly illustrate this variability in occurrence rates, Figure 2.2 shows HAIL amplitude data from two days in March 2001, with pronounced LEP event activity on the $28^{th}$, but not on the $9^{th}$, despite similar thunderstorm activity on the two days. The LEP events on the $28^{th}$ are induced by nonducted, obliquely propagating whistler waves, as determined by the temporal and spatial characteristics of the VLF perturbations.

## 2.2.1   Dependence on Trapped Radiation Belt Flux Levels

The early part of the month of March 2001 is a period of relatively quiet geomagnetic conditions (as indicated by the *Dst* index shown in Figure 2.1c). A decrease in the *Dst* index signifies a decrease in the Earth's magnetic field, indicative of an increase in the ring current which is often associated with an increase in the flux levels of trapped energetic electrons and ions [*Friedel and Korth*, 1995]. Interestingly, many of the later days of the month, starting at about 19 March, correspond to a period of high geomagnetic activity (low *Dst* index). Previous experimental data is suggestive of the dependence of the occurrence rate of LEP events on geomagnetic activity [*Leyser et al.*, 1984]. It is thus likely that the variation in LEP event occurrence rates evident in this study is due to the fact that the energetic electron population in the slot region increases with the advent of geomagnetic activity. Such an enhancement in the population of near-loss-cone energetic electrons available for scattering into the loss cone by lightning induced whistlers would proportionally increase the resulting precipitation fluxes, leading to the production of more frequent bursts of precipitation of sufficient magnitude to be classified as LEP events.

Figure 2.3 shows NOAA-16 POES satellite data for three passes over the HAIL array during March 2001. Data are shown (Figure 2.3a) for the Space Environment Monitor's (SEM-2) Medium Energy Proton and Electron Detector (MEPED). The
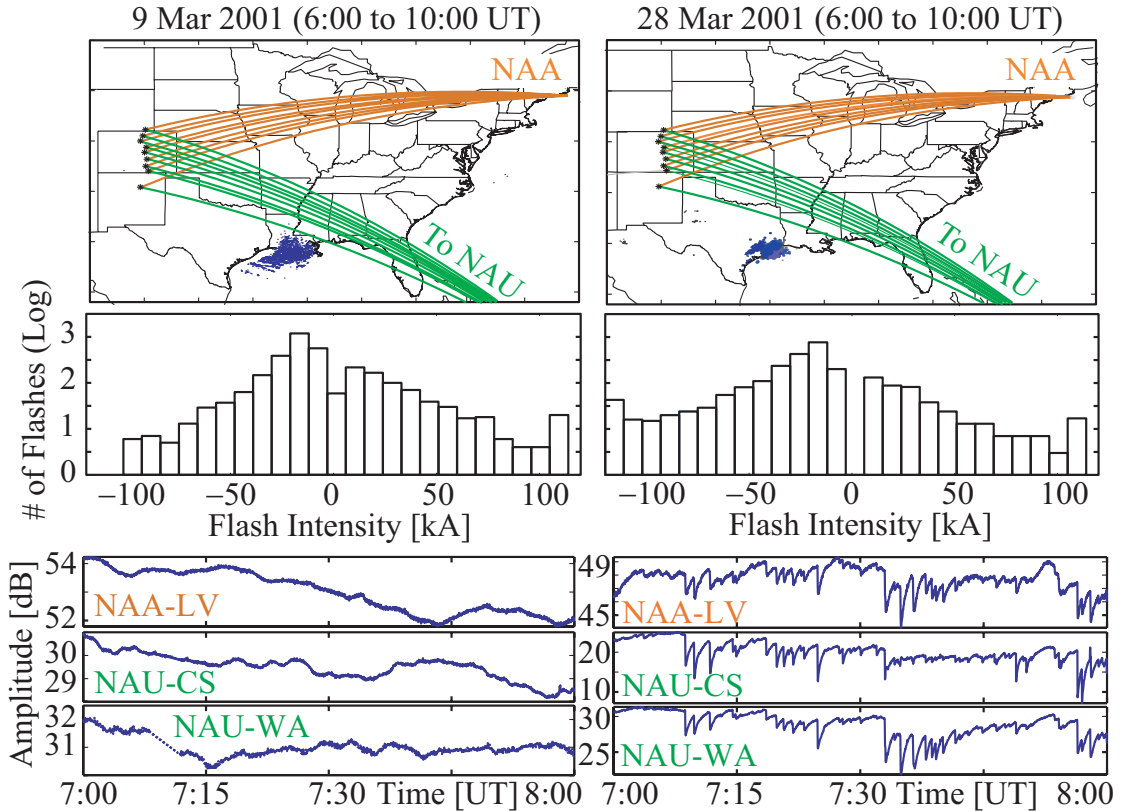
Figure 2.2: LEP events for two thunderstorms. (Top) Maps showing the location of two storms of similar locations during March 2001. Storms are designated by the blue dots representing CG flashes recorded by the NLDN network from 06:00 to 10:00 UT. (Middle) Histogram of all CG flashes as recorded by the NLDN network from 06:00 to 10:00 UT, binned according to flash intensity. (Bottom) HAIL amplitude data from 07:00 to 08:00 UT showing pronounced LEP event activity on 28 March, but not on 9 March 2001.

low altitude (830 to 870 km) polar-orbiting (98° inclination) satellite monitors the flux of energetic electrons. The data shown here are 16-second averaged 100-300 keV electron flux. For all passes, the angle of the detector with respect to the magnetic field remained nearly constant, between 60° and 70°. Furthermore, the variation of the angle with $L$-shell is nearly identical ($\pm 1°$) for each pass. The detector's aperture has a 15° half-angle cone. It is assumed that these measurements are representative of the flux of energetic electrons available for pitch-angle scattering into the loss cone by nonducted whistler wave interaction. Since the angle (with respect to the magnetic field) of the detector is similar for each pass, the variations in flux observed for the different passes are not likely to be due to differences in the measurement angle. Figure 2.3b shows a map of the corresponding tracks of the satellite passes over the HAIL array, projected down to 120 km altitude along the field line passing through the satellite. All passes occurred during the night between 07:00 and 09:30 UT, with each pass taking less than ten minutes to cross over the region of interest.

During the early part of the month, when the occurrence rates of LEP events are low, the energetic electron flux levels are also lower (Figure 2.3a). The satellite measurements made on 2 March 2001 are representative of the low flux levels detected during the first half of the month. However, a sharp increase in flux levels is observed during the later half of the month, including on 24 and 28 March 2001. This increase in trapped energetic flux levels suggests that the energetic electron population in the slot region ($2<L<3$) was enhanced by at least an order of magnitude above that observed earlier in the month. This time period corresponds to a period of high geomagnetic activity (Figure 2.1c) when the energetic electron population in the slot region has been shown to frequently increase [*Friedel and Korth*, 1995]. It is during this later part of the month when a relatively large number of LEP events are detected on the HAIL array. This occurrence supports the notion that the variance in the number of LEP events detected is largely due to the energetic electron population in the slot region increasing with the advent of geomagnetic activity, thus increasing the population of energetic electrons available for scattering into the loss cone by the lightning induced whistler waves.

The data in Figures 2.1 and 2.3 are consistent with the previously noted [*Leyser et*
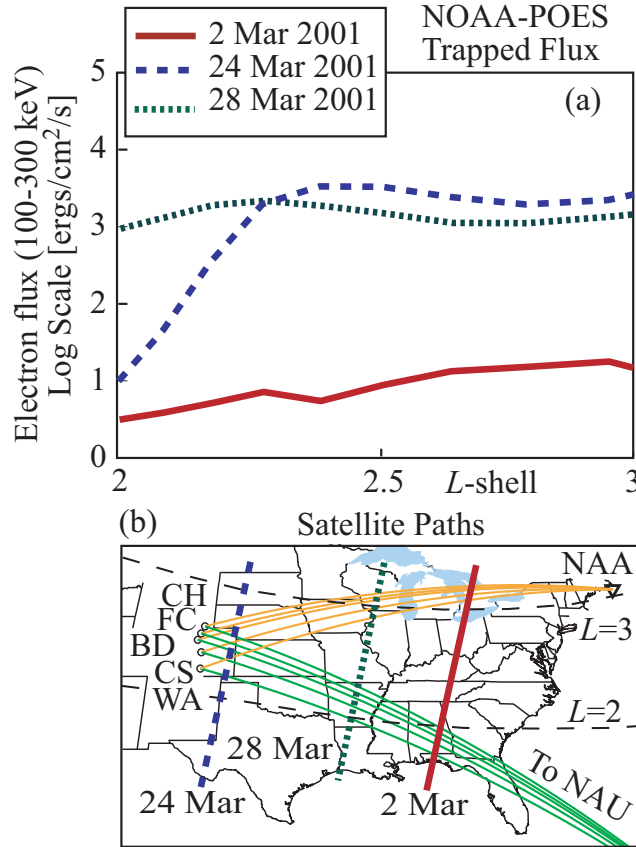
Figure 2.3: Energetic electron flux data for March 2001. (a) Data from the Space Environment Monitor's (SEM-2) Medium Energy Proton and Electron Detector (MEPED) aboard the NOAA-16 POES satellite. The low altitude (830 to 870 km) polar-orbiting (98° inclination) satellite monitors the flux of energetic electrons. The data shown here are 16-second averaged 100-300 keV electron flux with the detector nearly perpendicular (with a window of 30°) to the magnetic field. (b) A map of the corresponding tracks of the satellite passes over the HAIL array, projected down to 120 km altitude along the field line passing through the satellite. All passes occurred during the night between 07:00 and 09:30 UT, with each pass taking less than ten minutes over the region of interest.

*al.*, 1984] relationship between geomagnetic activity and the conditions conducive to the occurrence of detectable LEP events. However, a significantly longer time epoch of analysis is necessary to accurately establish the degree of this correlation, especially since the occurrence of causative lightning activity is a necessary prerequisite for LEP events to occur. Further work is also needed to determine what other factors (i.e., lightning location, equinoctial dependence), besides geomagnetic conditions and CG lightning flash rates, might influence the frequency of LEP events.

## 2.3   Two Case Studies of LEP Event Activity

The peak of LEP activity in March 2001 occurred on the $24^{th}$ and $28^{th}$. The lightning storms that contained the causative lightning discharges on these two days are shown in Figure 2.4, with each blue dot representing a single cloud-to-ground (CG) flash detected by the NLDN network from 06:00 to 10:00 UT. The lightning storm on 24 March 2001 is located in northern Texas, with over 34,000 CG flashes detected by the NLDN network from 06:00 to 10:00 UT. The storm remains quite localized, with little movement over this four-hour period. The mean location of all CG flashes recorded by NLDN for these four hours is at $32°57'$N, $98°10'$W, with a standard deviation in flash location of $58'$ in latitude and $3°48'$ in longitude. The storm on 28 March 2001 is located on the southeastern coast of Texas, with over 4,800 GC flashes detected by the NLDN network between 06:00 and 10:00 UT. This storm is also quite localized, with little movement over the four-hour period. The mean location of all CG flashes recorded by NLDN for these four hours is at $29°09'$N, $95°11'$W, with a standard deviation in flash location of $48'$ in latitude and $2°05'$ in longitude.

Due to the $3°48'$ difference in geographic latitude of the mean locations of the CG flashes detected by the NLDN network for the two storms, nonducted whistlers induced by lightning discharges associated with the different storms are expected to enter the magnetosphere at different $L$-shells, resulting in different precipitation signatures as a function of $L$-shell or geomagnetic latitude. Previous theoretical work [*Lauben et al.*, 1999, 2001] calculated the spatial distribution of the ionospheric "hot spots" (or precipitation regions), examined at various locations of causative
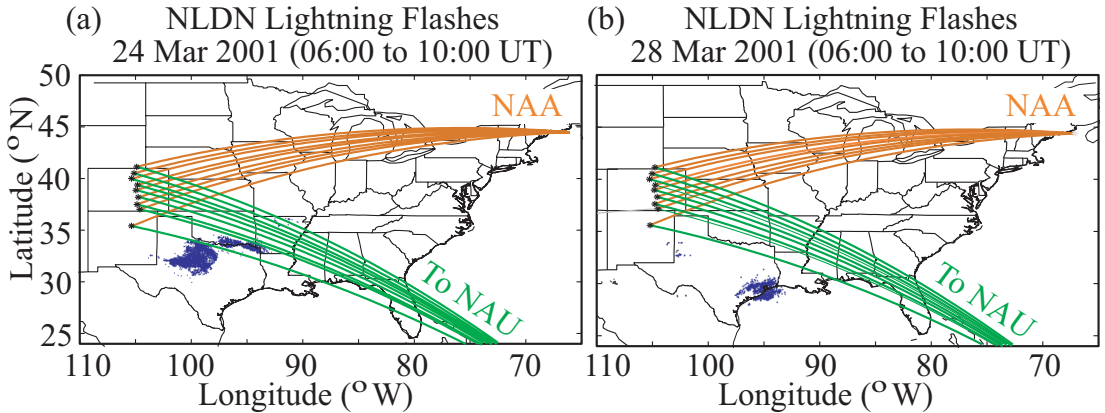
Figure 2.4: The location of all CG discharges recorded by NLDN from 06:00 to 10:00 UT on (a) 24 March and (b) 28 March 2001, represented by blue dots.

discharges, sampled every 10 degrees in latitude. The spatial and temporal distribution of the precipitation region is found to depend critically on the location of the causative discharges. The difference in source latitude of the two storms used in this dissertation (∼4 degrees) is significantly smaller than the 10 degree sampling used in *Lauben et al.* [1999, 2001]. However, it is assumed that this difference in source latitude would produce measurable differences (albeit on a smaller scale than in the theoretical work) in the precipitation signatures of LEP events for the two case studies. While it is unclear whether the differences observed in the precipitation signatures for the two time periods are due to this difference in injection latitude or other factors (i.e., geomagnetic activity, ionospheric conditions) between the two days studied, our analysis represents the first work documenting observational results that are consistent with theoretical calculations for the dependence of the latitude distribution of the precipitation regions on the *L*-shells at which the nonducted whistler wave energy is released.

On the two days studied here, the VLF data were acquired with different receivers of the HAIL array. On the first day, 24 March 2001, five receivers were operating, located at Fort Collins (FC), Boulder (BD), Colorado Springs (CS), and Walsenburg (WA), Colorado, and Cheyenne, Wyoming (CH). On the second day, 28 March 2001, receivers at six HAIL sites were operational, located at Boulder, Littleton (LT), Parker

(PK), Colorado Springs, and Walsenburg, Colorado along with Las Vegas, New Mexico (LV). All of these receivers are components of the overall HAIL array and monitor the amplitudes and phases of both the NAA and NAU transmitter signals as well as other VLF signals.

### 2.3.1   Case I: 24 March 2001

Between 06:00 and 10:00 UT on 24 March 2001, HAIL data from multiple receivers exhibits VLF signatures of numerous LEP events on both the NAA and NAU transmitters. In those four hours, 80 LEP events with a maximum perturbation of at least 0.5 dB are recorded. All events are detectable on at least three sets of VLF paths.

A typical LEP event for this time period is shown in Figure 2.5. The lower panel shows a three-minute sequence of HAIL data, exhibiting a large signal perturbation meeting our criteria of the LEP event classification. The event marked at $\sim$07:13:20 UT is clearly visible on multiple paths, which are displayed on the map above. The latitudinal distance ($\Delta\lambda_{\mathrm{m}}$) between the flash location and the point of crossing of the GCP and the geomagnetic longitude of the causative flash is shown for each signal. Each perturbed signal is a separate data set for analysis, yielding measurements of onset delay, onset duration, perturbation size, and recovery time versus latitudinal distance. For this event, a lightning flash in northern Texas causes precipitation in a region poleward displaced with respect to the location of the causative lightning, and a hypothetical ionospheric disturbance region is superimposed on the map based on the VLF signal perturbations measured on HAIL. A perturbation is observed on the paths denoted by dashed lines, but no measurable perturbation is detected on the paths denoted by solid lines. The southernmost paths (NAU-CS and NAU-WS) and the northernmost path (NAA-CH) do not exhibit any perturbation, meaning the full latitudinal extent of the LEP precipitation region is captured by the HAIL array. The majority of the LEP events during this time period are detected in a similar location, with multiple paths perturbed and the full spatial extent of the event captured with the available VLF signal paths.

Map of HAIL VLF Signal Paths



HAIL Data for 24-Mar-2001
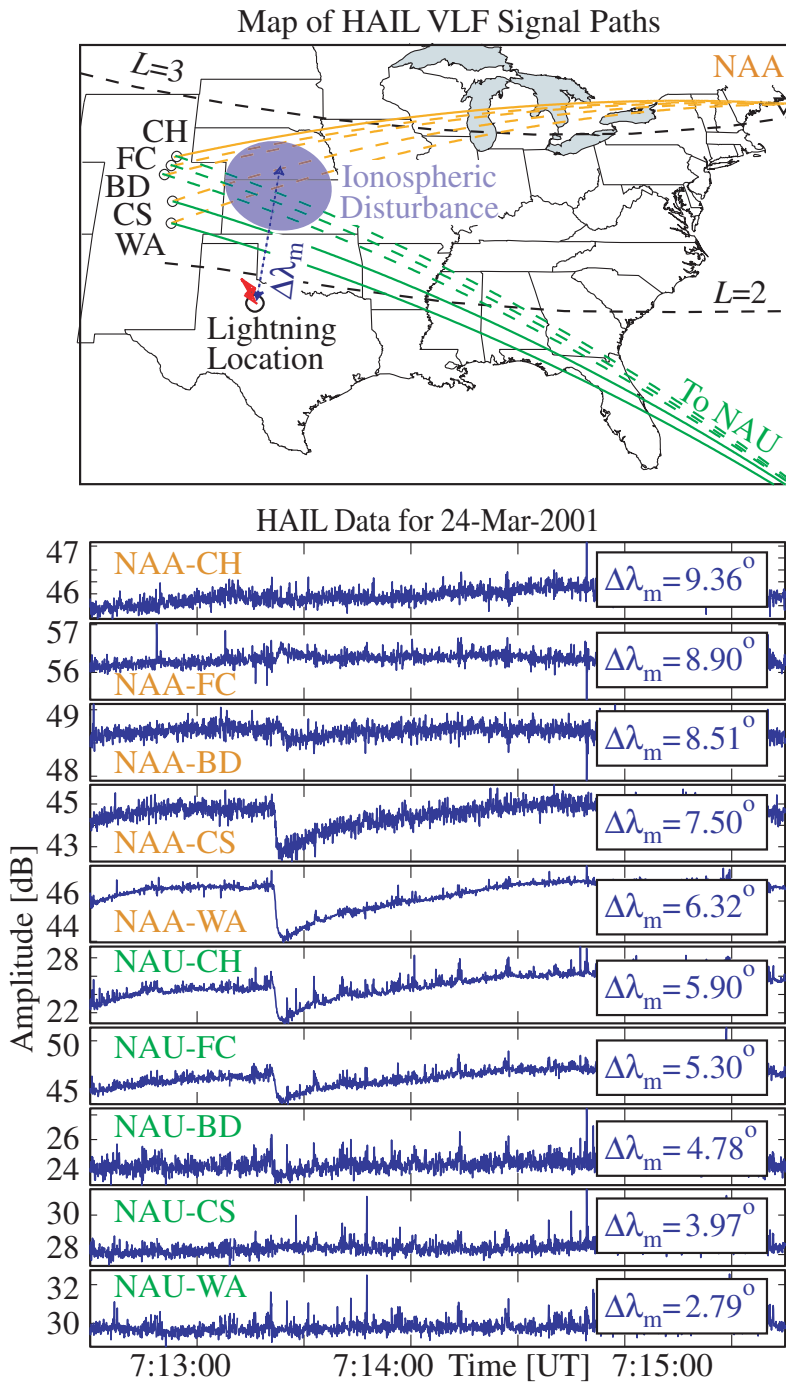
Figure 2.5: [Previous Page] Typical LEP event observed on 24 March 2001. The top panel shows a map of the five HAIL site locations, together with GCPs from the two VLF transmitters. Footprints of the $L=2$ and $L=3$ field lines are shown for reference. The causative lightning (07:13:20.723) is located in northern Texas ($35°41'$N, $92°04'$W). The inferred region of ionospheric disturbance is indicated on the map. An associated VLF perturbation is detected on signals arriving along those great circle paths denoted by dashed lines, with no measurable perturbation detected on signals propagating along the paths denoted by solid lines. The lower panels show a three-minute record of the amplitude (in dB) received at the five HAIL sites. Top to bottom corresponds to north to south GCPs in the map. The distance ($\Delta\lambda_\mathrm{m}$), in degrees latitude between the flash location and the point of crossing of the GCP of the geomagnetic longitude of the causative flash, is shown for each signal.

## 2.3.2   Case II: 28 March 2001

Similarly, HAIL data exhibited multiple VLF signatures of LEP events on both the NAA and NAU transmitters between 06:00 and 10:00 UT on 28 March 2001. Over the four-hour period, 81 LEP events with perturbations of at least 0.5 dB are recorded. Figure 2.6 illustrates an example of one such event. A large LEP event at $\sim$06:42:07 UT is recorded in the lower panel, with a hypothetical ionospheric disturbance region superimposed on the map based on the VLF signal perturbations measured on HAIL. A more accurate determination of the theoretical ionospheric disturbance region is provided in Section 4.3. While different stations are recording data during this day, the event is once again observable on only some of the paths (denoted by dashed lines), while there are no discernible perturbations on other paths (denoted by solid lines). The causative discharge is located on the southeastern coast of Texas, and therefore the region of precipitation is expected to be centered at a different latitude than on 24 March 2001. The southernmost (NAU-LV) and northernmost paths (NAA-PK, NAA-CS) do not exhibit any VLF perturbation, indicating that the latitudinal extent of the LEP precipitation region is once again captured.

Map of HAIL VLF Signal Paths



HAIL Data for 28-Mar-2001
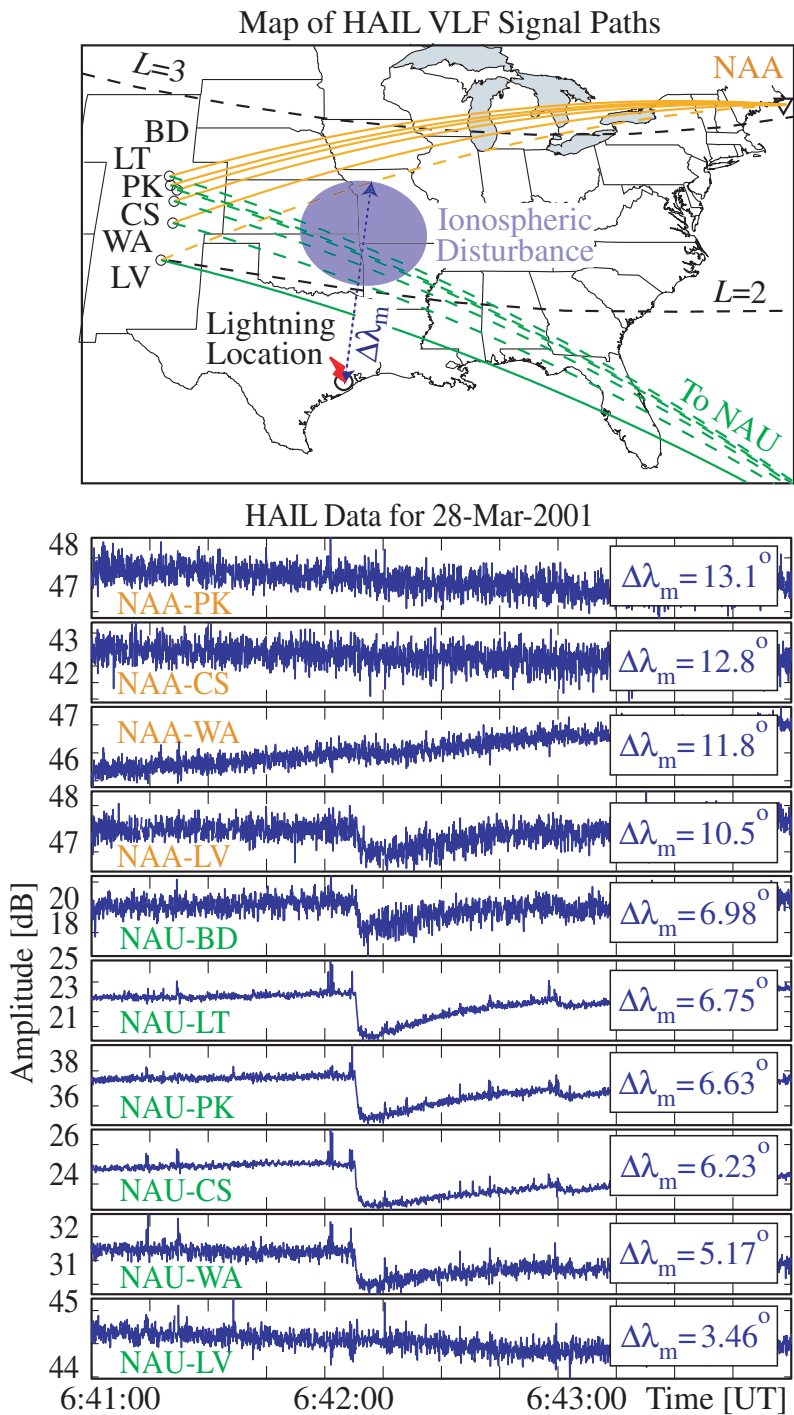
Figure 2.6: [Previous Page] Typical LEP events observed on 28 March 2001. The top panel shows a map of the six HAIL site locations. The causative lightning (06:42:07.023 UT) is located on the southeastern coast of Texas ($29°19'$N, $95°28'$W). The inferred region of ionospheric disturbance is superimposed. The lower panels show a three-minute record of the received amplitude (in dB) at the six operating HAIL sites. The distance ($\Delta\lambda_\mathrm{m}$), in degrees latitude, between the flash location and the point of crossing of the GCP of the geomagnetic longitude of the causative flash is shown for each signal. The format of the figure is identical to that of Figure 2.5.

## 2.4   Cloud-to-Ground (CG) Lightning

For each LEP event included in this study, a spheric (see Section 1.3) associated with the causative lightning discharge is measured at many of the HAIL sites with 10 millisecond resolution. The recorded timing of the spheric is then associated with a CG discharge in the high resolution (<1 ms) NLDN data. The majority of the causative flashes have both discernible spherics associated with the causative lightning flash and a corresponding CG discharge in the NLDN data (typically within measurement resolution, or 10 ms of the causative spheric time). Of the 80 events on 24 March, 72 (or 90%) are time-coincident with a CG flash in the NLDN data. On 28 March, 68 of 81 (or 84%) events are time-coincident with CG discharges. Though intracloud (IC) lightning is generally more common than CG flashes at these latitudes [*Prentice and Mackeras*, 1971], the NLDN network typically does not record them. By design, the NLDN network records only CG lightning flashes, with a detection efficiency of between 80% and 90% at these locations [*Cummins et al.*, 1998]. The fact that over 80% of the LEP events are time-coincident with CG flashes in the NLDN data implies that CG flashes induced nearly all of the detected LEP events (i.e., those events for which there are not associated NLDN recorded flashes are probably simply missed by the NLDN). The potential role of IC discharges remains undetermined until there is a reliable method of recording them. In this connection, it should be noted that while VLF recordings at HAIL sites routinely record impulsive spherics from both CG and IC flashes, there is no easy way by which the flash type or location can be determined from these data. Previous work [*Inan et al.*, 1988a] also associated the majority of LEP events with CG discharges. However the lower detection efficiency of

the lightning detection network in the region of that particular case study (the storm was several hundred kilometers off the eastern coast of the United States) prevented the association of as high a percentage of LEP events with CG lightning discharges.

Figure 2.7 shows that the majority of CG flashes detected by the NLDN network (all occurring within the same two storms) did not produce perturbations on the HAIL array consistent with our criteria for LEP events. During the four-hour period on 24 March, only 80 of the 34,725 detected CG flashes (0.23%) produce LEP events with perturbations greater than 0.5 dB. Similarly, only 81 of 4,810 flashes (1.68%) produce LEP events with perturbations greater than 0.5 dB during the period analyzed on 28 March. Figures 2.7b and d show that a larger percentage (>30%) of lightning discharges with higher peak current magnitudes (>100 kA) produce detectable LEP events, although even some of the largest flashes are not associated with LEP events. Discharges with larger peak currents produce more electromagnetic radiation, and therefore release more wave energy into the magnetosphere that can propagate as a nonducted whistler and induce electron precipitation. However, it is possible that other properties (such as the frequency content) of the wave energy released might be controlling factors in the precipitation induced by a lightning flash of a given intensity. The frequency content of the whistler wave determines the energy content of the electrons scattered in cyclotron resonance [*Inan et al.*, 1989], and thus influences the energy spectra and flux levels of the precipitated electrons, so that the production of detectable LEP bursts might depend on this factor which is not recorded by the NLDN network.

The polarity of the peak current signifies the direction of the charge flow. Positive (+CG) discharges represent the removal of positive charge from the cloud and vice versa for negative (-CG) discharges. Both of these polarities are referred to as CG discharges here. The data in hand does not suggest any dependence on the polarity of the current, but rather only on its magnitude. On average, positive (+CG) discharges have larger peak current magnitudes, while negative (-CG) discharges occur more frequently. But given equal peak current intensities, the data suggest that a negative flash is equally likely to induce a detectable LEP event as a positive flash. Such a dependence is expected since the LEP event is believed to be produced by the

electromagnetic impulse generated by the lightning discharge, which couples through the ionosphere and up into the magnetosphere where it becomes a whistler, and both positive and negative flashes can equally generate such electromagnetic waves, the magnitude of which is determined by the rate of change of current [*Uman*, 1984, p.61].

While previous studies of LEP events produced by ducted whistlers noted the presence of the magnetospheric duct as a necessary condition for the occurrence of an LEP event, no such condition is required for the occurrence of nonducted LEP events. There is reason to expect that smaller discharges also cause LEP events, but the wave energy released by these lower intensity currents may not produce enough precipitation and secondary ionization to significantly (i.e., detectably) perturb VLF signals.

Lightning flashes occurring in the northern hemisphere produce south-going whistler waves, causing counter-streaming resonant particles perturbed through gyroresonance interaction with the south-going whistler wave to precipitate into the northern hemisphere. This type of precipitation is referred to as "direct" precipitation, as opposed to "mirrored" precipitation [*Inan et al.*, 1985, 1988a]. Particles are also precipitated in the southern hemisphere ("mirrored" precipitation) as a result of gyroresonance interaction with south-going whistler waves, after first mirroring and/or backscattering in the north. At the geographic longitudes of the regions studied in this paper, the magnetic field at 100 km altitude is stronger in the northern hemisphere, and thus the mirror height for trapped energetic electrons is higher than in the conjugate point in the southern hemisphere [*Inan et al.*, 1988b]. Therefore, if electrons just above the loss cone are weakly scattered into the loss cone, they do not all precipitate into the atmosphere in the northern hemisphere but rather mirror there and backscatter and return to the southern hemisphere where they are deposited into the upper atmosphere. Only in cases where the pitch angle scattering is sufficiently strong would a burst of electrons precipitate into the atmosphere in the north. For causative lightning flashes located near regions conjugate to the South Atlantic magnetic anomaly, as is the case here, mirrored precipitation is thus believed to be significantly more effective (i.e., higher precipitated flux levels are expected) than direct precipitation
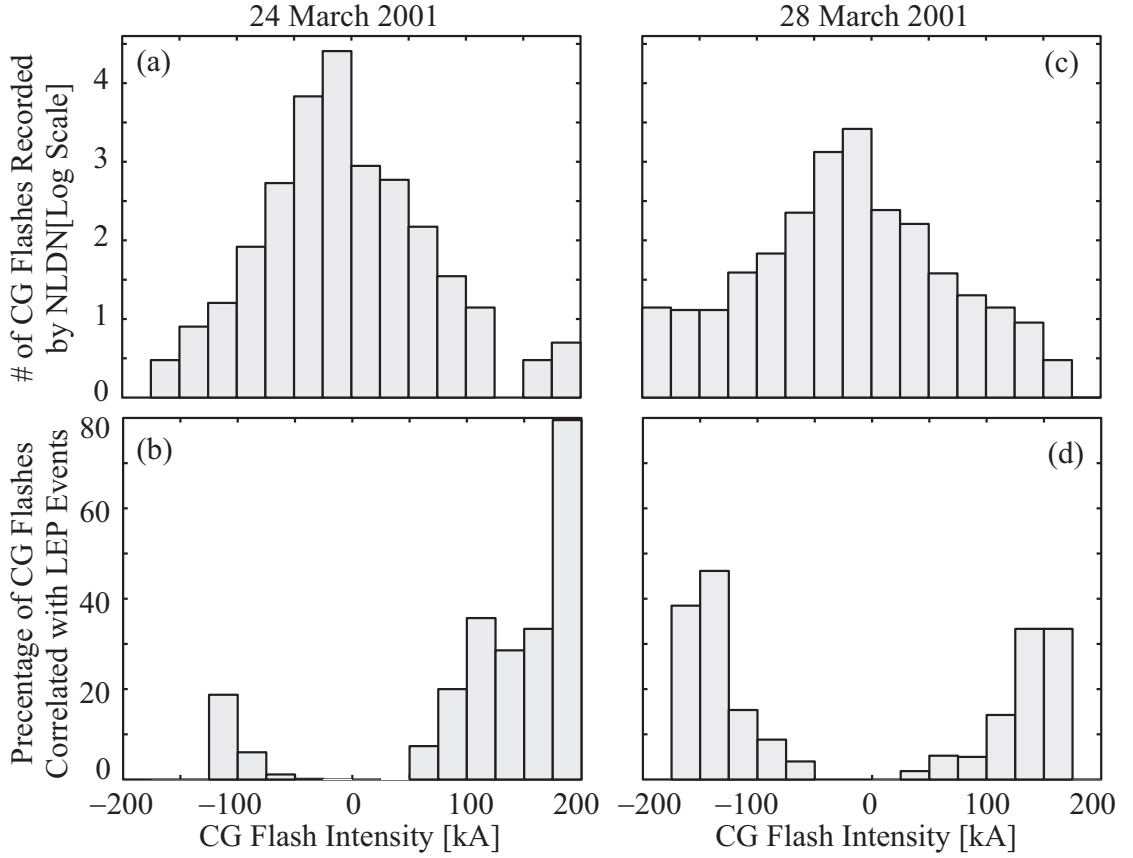
Figure 2.7: (a) Distribution (shown on a log scale) of all CG flashes detected by the NLDN network in terms of flash intensity for the period from 06:00 to 10:00 UT on 24 March 2001. (b) Percentages of all CG flashes detected by the NLDN network that are time-correlated with VLF LEP events, in terms of CG flash intensity. As for all histograms following, those bins with three or less data points are deemed to not be statistically significant, and thus not shown. (c) Distribution of all CG flashes detected by the NLDN network in terms of flash intensity for the period from 06:00 to 10:00 UT on 28 March 2001. (d) Percentages of all CG flashes detected by the NLDN network that are time-correlated with VLF LEP events, in terms of CG flash intensity, on 28 March 2001.

[*Inan et al.*, 1988b]. In fact, the LEP events observed on HAIL may be due to particles that have first "backscattered" in the southern hemisphere, as described in Section 4.4 and *Burgess and Inan* [1990, Fig. 5]. Simultaneous observations of precipitation in both hemispheres have been carried out in a few selected cases [e.g., *Burgess and Inan*, 1990; *Peter et al.*, 2005a], but the relative roles of "direct" versus "mirrored" precipitation in LEP events is still largely unknown.

The difference in mirroring height between the northern and southern hemispheres at the longitudes of the HAIL array is one possible reason that the majority of CG flashes detected by the NLDN network did not produce detectable precipitation on the HAIL array. This observation also suggests that higher precipitated flux levels (and thus a higher number of precipitation events above a threshold) could be expected in the southern hemisphere, and that measurements of precipitation in the northern hemisphere may represent only a small fraction of the total amount of energetic electrons that are precipitated into the atmosphere and lost from the radiation belts.

In summary, there are at least two reasons for the low percentage of CG discharges in the NLDN data that are time-correlated with LEP events detected by the HAIL array. Firstly, only events with perturbation magnitudes greater than 0.5 dB are considered here. Secondly, the "direct" precipitation measured at the longitudes of the HAIL array is expected to be less pronounced than the "mirrored" precipitation induced in the southern hemisphere, due to the South Atlantic magnetic anomaly. These two factors imply that in our study we observe events due to only those whistlers that cause the strongest pitch angle scattering of electrons, and thus the most intense precipitation bursts, while the majority of the induced precipitation may be below the threshold of observation. Finally, other factors, such as ionospheric irregularities, the pitch angle distribution of trapped energetic electrons, and the spectral properties of the electromagnetic radiation from the CG discharges, may influence the amount of induced precipitation.

## 2.5 Temporal and Spatial Characteristics of LEP Events

The VLF signatures of the LEP events monitored during the two days under study are time-correlated with CG lightning flashes recorded in the NLDN data, and the previously defined measurable temporal and spatial features are determined. A statistical analysis of these parameters is presented in this section.

The four measurables: event perturbation magnitude, onset delay, onset duration and recovery time, are recorded for each LEP event. While this study constitutes the first statistical work aimed at quantifying these parameters, there have been several previous theoretical and experimental works on individual events. In this context, our statistical results are compared to both results of past experimental work [*Johnson et al.*, 1999] and theoretical calculations [*Lauben et al.*, 1999, 2001].

The theoretical calculations of *Lauben et al.* [1999, 2001] are based on a quantitative model of oblique whistler-induced electron precipitation. The model calculates the temporal and spatial characteristics of electron precipitation caused by lightning discharges occurring at mid-latitudes. A simple tilted dipole magnetic field model with typical magnetospheric conditions was used, with peak currents of the lightning discharges set to ∼10 kA, generally lower than those discharges that are associated with LEP events in this study. *Johnson et al.* [1999] reported on a number of LEP events monitored on 18 October 1998, with the causative discharges located in the middle of Texas. In that work, no attempt was made to correlate the event measurables with the locations of the causative discharges, so the influence of causative discharge latitude on the LEP event signatures was not considered.

Only those LEP events successfully correlated with CG discharges in the NLDN data (72 events on 24 March 24 2001, 68 events on 28 March 2001) are included in our statistical data analysis. For each of these events the geomagnetic latitude and longitude of the causative lightning discharge are taken from the NLDN data. For each received signal, the intersection point of the Great Circle Path (GCP) and the magnetic longitude of the causative discharge is calculated. The latitudinal distance $\Delta\lambda_{\mathrm{m}}$ (in degrees) between the location of the causative discharge and this intersection

point is then calculated for each received signal. All data points are then binned according to this distance between the causative discharge and precipitation region location, and the values for each bin are averaged and plotted in histogram format. An uncertainty in latitude of $\pm30'$ is introduced by the binning of the data sets, and this uncertainty includes the standard deviation (due to the distribution of data points as measured) and any observational error, which is generally smaller than the standard deviation. Throughout this dissertation, the use of the symbol $\pm$ is meant to signify the uncertainty of the measurement, including the standard deviation and/or observational errors.

### 2.5.1   Spatial Signatures of LEP Regions

Figure 2.8 shows the magnitude of perturbation of the VLF signal versus the distance between the causative discharge and the corresponding location on the GCP ($\Delta\lambda_{\mathrm{m}}$). Each LEP event is normalized so that the maximum VLF signal perturbation detected is equal to 1 dB, and so that each LEP event contributes equally to the histogram regardless of the intensity of the disturbance. The VLF signal perturbations detected on the NAU GCPs are then multiplied by a scale factor of 0.45 (determined empirically) to realize continuity between the perturbations recorded on the two transmitter signals. The NAA and NAU signal measurements are scaled differently due to their different sensitivities to a given perturbation, a result of the difference in frequencies and GCPs between these two signals. As mentioned previously, the HAIL array captures the peak and latitudinal extent of the precipitation regions on both days. Due to the disposition of the array, only variations in latitude are distinguishable, and for the purposes of this study, we assume the precipitation region to be longitudinally symmetric. Such an assumption is consistent with previous calculations [*Lauben et al.*, 1999] based on a simple tilted dipole model and neglecting longitudinal gradients in the Earth's magnetic field or cold plasma density.

On 24 March 2001, the mean location of all CG flashes detected by the NLDN network for the four-hour period between 06:00 and 10:00 UT is at $32°57'$N latitude. Figure 2.8a shows that the measured peak of the perturbation occurs in the $6°30'$ to
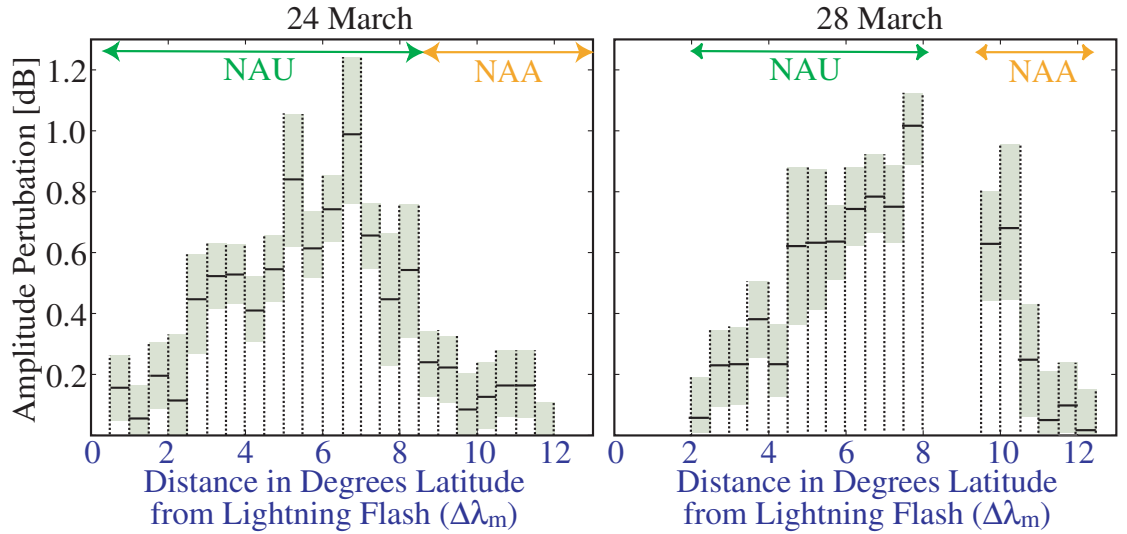
Figure 2.8: The normalized magnitude of perturbations caused by LEP events as a function of distance between the flash location and GCP for 24 March (left) and 28 March (right) 2001. All values are first binned (bins demarcated by dashed lines) according to the latitudinal distance between the flash location and the point of crossing of the GCP and the geomagnetic longitude of the causative flash ($\Delta\lambda_m$), as illustrated in Figure 2.5. The values in each bin are subsequently averaged (shown by a solid line). The standard deviation incorporates the measurement error and is denoted by the shaded area. The measurements taken from the more northern NAA paths and the more southern NAU paths are denoted as such. The gap in data on 28 March is due to the gap between the NAA and NAU GCPs (see Figure 2.6). Bins with three or less data points are not included.

7° (715 to 770 km) bin north of this location, at $39°42'\pm30'$N. The majority (>90%) of the precipitation occurs in the region $2°\pm30'$ to $10°\pm30'$ poleward of the causative discharge, over a range of $880\pm110$ km. A similar precipitation pattern is measured on 28 March 2001. The mean location for the CG discharges detected by the NLDN network between 06:00 and 10:00 UT is located further south ($29°09'$N), and the nonducted wave energy is injected at a slightly lower $L$-shell. The gap in the data, from 8° to 9°, is due to the lack of overlap between the NAA and NAU GCPs for this location. Despite a shape similar to that on 24 March, the peak is displaced further, in the $7°30'$ to 8° (825 to 880 km) bin north of the causative thunderstorm, at a corresponding latitude of $36°50'\pm30'$N. The majority (90%) of the precipitation occurs in a region $3°\pm30'$ to $12°\pm30'$ poleward of the causative discharge, over a range of $990\pm110$ km, more extensive than that on 24 March. Therefore those events associated with causative discharges at lower latitudes (those on 28 March) typically exhibit a larger region of precipitation and are displaced further poleward from the causative discharge.

When compared to the theoretical calculations for nonducted whistler-induced precipitation, our results agree well with the general spatial disposition of the precipitation region. Figure 2.9 shows *Lauben et al.* [2001] model calculations for precipitated energy flux ($E$>100 keV), integrated over longitude and time to obtain the profile $\tilde{Q}(\Delta\lambda_{\mathrm{m}})$. The model uses a 10 kA peak current discharge with a lightning source latitude (29°N) comparable to those of the case studies. The solid black line depicts the theoretical values obtained from the *Lauben et al.* [2001] model, with the peak of precipitation denoted by the solid arrow. The profile $\tilde{Q}(\Delta\lambda_{\mathrm{m}})$ is plotted on a log scale as a function of latitudinal distance ($\Delta\lambda_{\mathrm{m}}$) between the flash location and the point of precipitation, the same horizontal axis as that for Figure 2.8.

It should be noted that the *Lauben et al.* [2001] model did not consider magnetospheric reflections of the nonducted whistler waves, instead only considering the first traverse of the magnetic equator (a so-called "hop") of the whistler waves. Furthermore, the model assumed a cold plasmaspheric density based on the work of *Carpenter and Anderson* [1992]. In this chapter, we compare our analysis with the model results of *Lauben et al.* [2001]. In Chapters 3–5 of this dissertation, we describe a new model

framework and compare the modeling results directly to VLF signal observations of LEP events included in the study described here. Many of the discrepancies between the *Lauben et al.* [2001] model and the observations described here are indeed resolved with the new model framework of Chapters 3–5.

A third-order polynomial is fit to the measured perturbation magnitude (Figure 2.8) for both days, with a correlation coefficient of 0.84 for 24 March and 0.91 for 28 March. *Inan and Carpenter* [1987] showed that for single-waveguide mode propagation the change of amplitude in the VLF signal ($\Delta A$) is proportional to $d\Delta h$, with $d$ being the extent of the perturbed region along the propagation path and $\Delta h$ being the differential reduction of the lower ionospheric reflection height for the VLF signal. Although VLF propagation on shorter paths (and on land) is more complicated and generally involves the superposition of several waveguide modes [*Poulsen et al.*, 1993a], we assume that the measured perturbation magnitude ($\Delta A$) is still approximately proportional to $d\Delta h$. We also assume that $d\Delta h$ is proportional to the precipitated energy flux $\tilde{Q}(\Delta\lambda_\mathrm{m})$, in order to compare our measurements of event perturbation magnitude ($\Delta A$) directly to the theoretical calculations of *Lauben et al.* [2001]. We adopt these assumptions for simplicity and for the purposes of the discussion here. The validity of these assumptions is assessed with our more detailed model calculations described in Section 3.3.3, where we apply a full numerical model of VLF signal propagation in the Earth-ionosphere waveguide and incorporate variations in ionospheric density along the path.

The fitted values for perturbation magnitude are compared to the theoretical values for precipitation energy flux $\tilde{Q}(\Delta\lambda_\mathrm{m})$ in Figure 2.9. For the red (24 March) and green (28 March) dashed lines, the peaks are denoted by the dashed arrows and the peak values are normalized to match the peak value calculated by the model. For lightning located at a similar latitude, the majority of the electron flux is calculated to be deposited at $L>2$, at slightly higher latitudes than observed in the two case studies. The model calculates that the peak of the energy flux deposited would have a greater poleward displacement ($12°$) from the causative discharge than that observed ($6°45'\pm30'$ on 24 March and $7°45'\pm30'$ on 28 March). As is discussed in Section 3.3.3, this discrepancy between the theoretical model of *Lauben et al.* [2001]
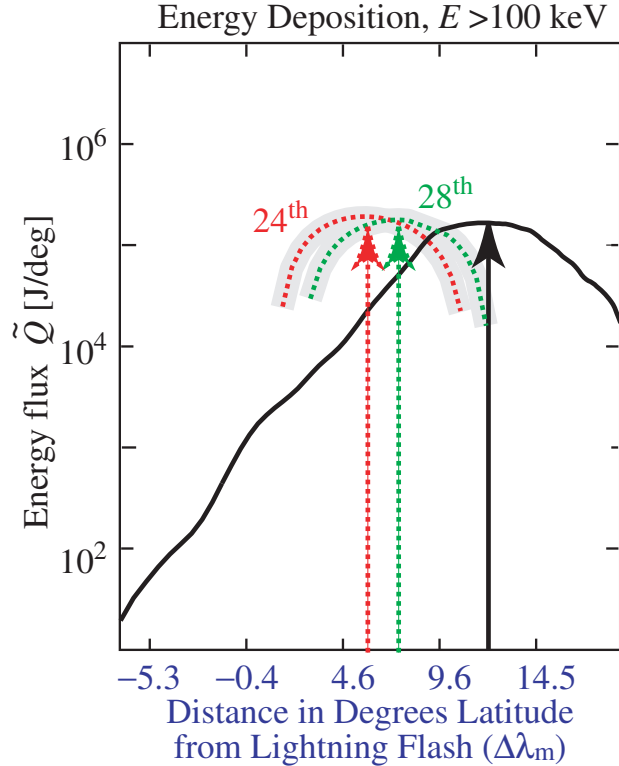
Figure 2.9: The panel shows precipitated energy flux ($E>100$ keV), integrated over longitude and time to obtain the profile $\tilde{Q}(\Delta\lambda_{\mathrm{m}})$, as calculated in *Lauben et al.* [2001] for a lightning source latitude of $\sim$29°N. The solid black line depicts the theoretical values obtained from the model, with the peak of precipitation denoted by the solid arrow. Third-order polynomials are fit to the normalized magnitude of perturbation measured on the two days (Figure 2.8), and represent the presumed energy flux density measured by the HAIL array based on the assumption that $\Delta A \propto \tilde{Q}(\Delta\lambda_{\mathrm{m}})$. The red (24 March) and green (28 March) dashed lines denote the fitted polynomials, with the shaded areas denoting the observational uncertainty. The peaks are denoted by the dashed arrows, and are normalized to match the peak value calculated by the model.

and observations made on HAIL is resolved via the use of a cold plasmaspheric density model different than *Carpenter and Anderson* [1992].

According to the observations made on HAIL, over 90% of the observed precipitation occurs within a region of 880±110 km (8°±1°) on 24 March, and 990±110 km (9°±1°) on 28 March. The region within which 90% of the predicted precipitation occurs is smaller than that calculated by the model (1380±110 km or 12°30'±1°). This discrepancy between the theoretical model and observations in terms of the regional extent in which the majority (90%) of the precipitation occurs is examined in Section 4.4, where it is argued that the discrepancy may indicate the model assumes a slower falloff in whistler wave energy illumination with distance than what is actually generated by the lightning flash. Another possible explanation discussed in Section 4.4 (and also in Section 2.4) is that the theoretical model does not properly account for differences in the relative amounts of "direct" versus "mirrored" precipitation induced.

The *Lauben et al.* [1999, 2001] model calculates a larger region of precipitation for causative discharges located at lower latitudes. The same qualitative trend is seen in the observed data for the two periods of the case study, with larger regions of precipitation associated with causative discharges located at lower latitudes (28 March) than higher latitudes (24 March). The previous experimental measurements (e.g., Figure 4 of *Johnson et al.* [1999]) were similar to the perturbation signatures observed here, both qualitatively and quantitatively.

In terms of the poleward displacement of the precipitation region, the *Lauben et al.* [1999, 2001] model calculates that the precipitation region would have a greater poleward displacement (with respect to its causative discharge) for source lightning located at lower latitudes. This calculation is consistent with the larger poleward displacement observed on 28 March than on 24 March, although the absolute value of the poleward displacement calculated by the model is larger than either of those observed on the two days. We note that the latitudinal displacement observed on the two days is more in line with that measured in *Johnson et al.* [1999]. These discrepancies may indicate that the actual oblique whistler-mode raypaths are confined to lower $L$-shells than those in the model, due to a more rapid radial variation of the magnetospheric

cold plasma density. The *Lauben et al.* [2001] model uses a cold plasmaspheric density model based on *Carpenter and Anderson* [1992], while the model described in Section 3.3.1 uses a plasmaspheric density model based on *Tarcsai et al.* [1988] that is more relevant for lower $L$-shells ($L<2.5$). As the results of Section 4.4 indicate, the refined model of Section 3.3.1 accurately captures the poleward displacement of the precipitation region from the lightning flash.

In summary, while past experimental work coincides with our results quantitatively, the theoretical model of *Lauben et al.* [1999, 2001] calculates slightly larger displacements and wider precipitation regions than those observed. As will be shown in Section 4.4 for two representative LEP events, refinements to the theoretical model (in particular the use of a more accurate equatorial profile of the cold plasma density) resolve these discrepancies.

### 2.5.2   Temporal Signatures of LEP Events

#### Onset Delay

Figure 2.10 shows the average onset delay versus the latitudinal distance between the causative discharge and the corresponding disturbance point along the GCP. The measurements are first binned according to their distance from the causative discharge. As there are approximately seventy LEP events included in the analysis for each day, and each LEP event is measured independently on several VLF signal paths, each bin typically includes more than twenty measurements. The values in each bin are subsequently averaged to determine a mean and standard deviation for each bin. A linear increase in onset delay with latitude is evident for both days. The onset delay is linearly proportional to the latitudinal distance from the lightning source with a correlation coefficient of 0.97 on 24 March and 0.96 on 28 March. This correlation means that the onset of precipitation is delayed proportionally to the northward displacement from the causative discharge. On 24 March, events are generally first observed 0.3±0.1 seconds after the causative discharge, and thereafter extend northward in latitude, with the most northern paths perturbed 2.0±0.2 seconds after the
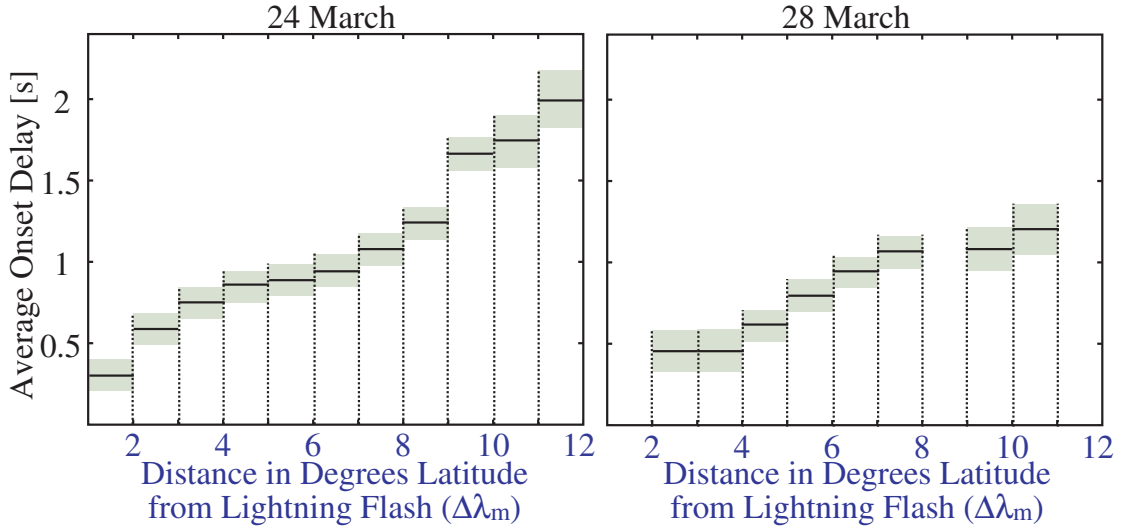
Figure 2.10: Average onset delay for the LEP events as a function of distance between flash location and GCP for 24 March (left) and 28 March (right) 2001. All values are first binned according to the distance from the flash, and then averaged (shown by a solid line). The standard deviation incorporates measurement error and is denoted by the shaded area.

original discharge. The onset delay increases $0.15\pm0.05$ seconds per degree in latitude ($1.4\pm0.5\times10^{-3}$ s/km). On 28 March, the events are first seen $0.4\pm0.2$ seconds after the causative discharge and again extend northward in latitude, with the northernmost paths perturbed $1.2\pm0.2$ seconds after the discharge. The event is seen to extend northward at a slower rate than on 24 March, with the onset delay increasing $0.08\pm0.04$ seconds per degree ($7.3\pm0.4\times10^{-4}$ s/km). Therefore, for those events associated with causative discharges located at lower latitudes (28 March), the onset delay appears to increase less rapidly with increasing latitude.

The nearly linear increase in onset delay with increasing $L$-shell (or latitude) is consistent with previous experimental [*Johnson et al.*, 1999] and theoretical [*Lauben et al.*, 1999, 2001] works. Figure 2.12 shows an overlay of individual precipitation energy flux profiles for selected $L$ shells based on theoretical calculations from *Lauben et al.* [2001]. Only some of the curves ($2.4<L<3$) are relevant at these latitudes. The absolute magnitudes of the onset delays calculated by the *Lauben et al.* [2001] model (0.2 s to 0.8 s) are shorter than those observed here, possibly due to the fact that the

precipitation is detectable in the northern hemisphere only after first backscattering in the southern hemisphere, an effect not considered in the model. This possibility is discussed in more detail in Section 4.4. The differences between the two case studies in the rate of increase in onset delay with latitude are not easily explained by the model, and may be due to differences in magnetospheric conditions, such as differences in the cold plasma density profile as a function of $L$-shell (which determines the wave and particle travel times to and from the interaction regions and thus the onset delay).

**Onset Duration**

The format of Figure 2.11 is identical to that of Figure 2.10, except that the onset duration is plotted rather than the onset delay. Once again, a linear increase with increasing $L$-shell is evident on both days. The event duration is linearly proportional to the latitudinal distance from the lightning source, with a correlation coefficient of 0.98 on 24 March and 0.91 on 28 March 2001. The strong correlation indicates that the further north from the causative discharge the long the precipitation persists. On 24 March, the duration increases from 1.5±0.2 seconds at the most southern measurement to 4.1±0.5 seconds at the most northern. This equals a rate of increase in duration of 0.26±0.07 seconds per degree latitude ($2.3 \pm 0.6 \times 10^{-3}$ s/km). For 28 March, the duration increases from 1.2±0.2 to 2.5±0.2 seconds; the precipitation does not continue as long as on 24 March. The rate of increase on 28 March is less than on 24 March, at 0.13±0.04 seconds per degree ($1.2 \pm 0.4 \times 10^{-3}$ s/km). To summarize, those events associated with causative discharges at lower latitudes (those on 28 March), generally exhibit shorter durations and a slower rate of increase in duration with latitude.

The increase in duration with increasing $L$-value is consistent with the calculations of the theoretical model of *Lauben et al.* [2001] (Figure 2.12). The model calculates shorter durations (0.3 to 1.0 seconds) at lower latitudes ($L$-shells), with significantly longer durations (1.5 to 3 seconds) at higher latitudes, similar to those of the case studies. The generally shorter durations calculated by the model may be indicative of a lower than usual cold plasma density in the magnetosphere, which would result in increased propagation speeds for the wave and also higher energies (and thus faster
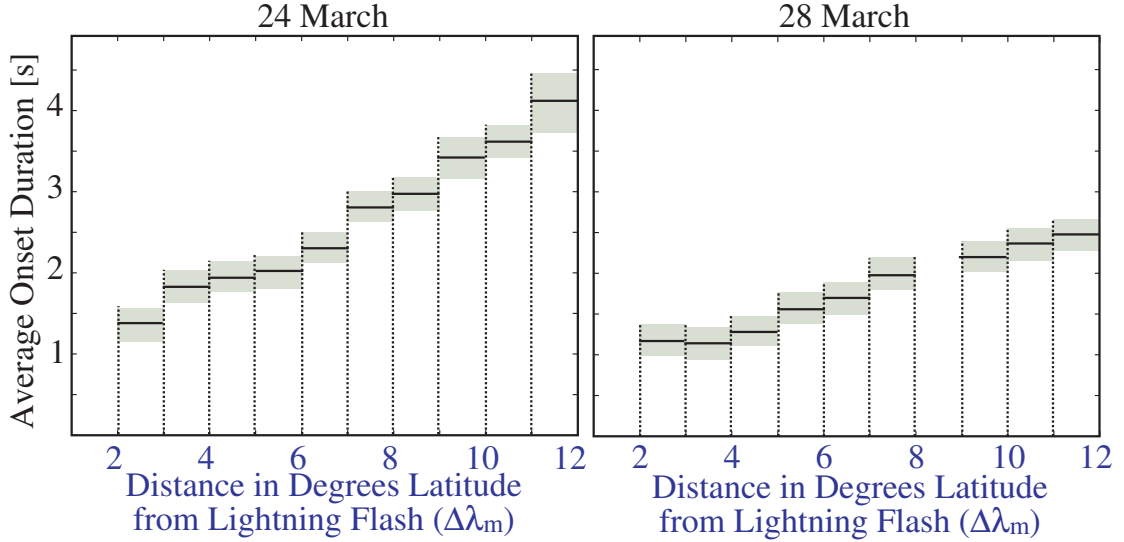
Figure 2.11: Average onset duration for the LEP events as a function of distance between flash location and great circle path (GCP) for 24 March (left) and 28 March (right) 2001. The format is identical to that of Figure 2.10, with the average value for each bin denoted by a solid line and the standard deviation by the shaded area.

travel times) for resonant electrons. It should also be noted that the model does not include magnetospheric reflections of the obliquely propagating whistler-mode wave, which have been recently shown to lengthen the duration of electron precipitation [*Bortnik et al.*, 2003a]. Incorporating these and other modifications, the theoretical model framework described in Section 3.3.1 calculates a duration of precipitation consistent with that observed for two representative LEP events.

The differences in onset delay and onset duration between the two days analyzed here are not easily explained by the model, and may be due to differences in magnetospheric conditions, such as the cold plasma density profile, rather than due to a dependence of onset duration on source latitude.

**Event Recovery**

Finally, Figure 2.13 shows recovery time versus the distance between the causative discharge and the GCP. Unlike the other spatial and temporal signatures, the recovery
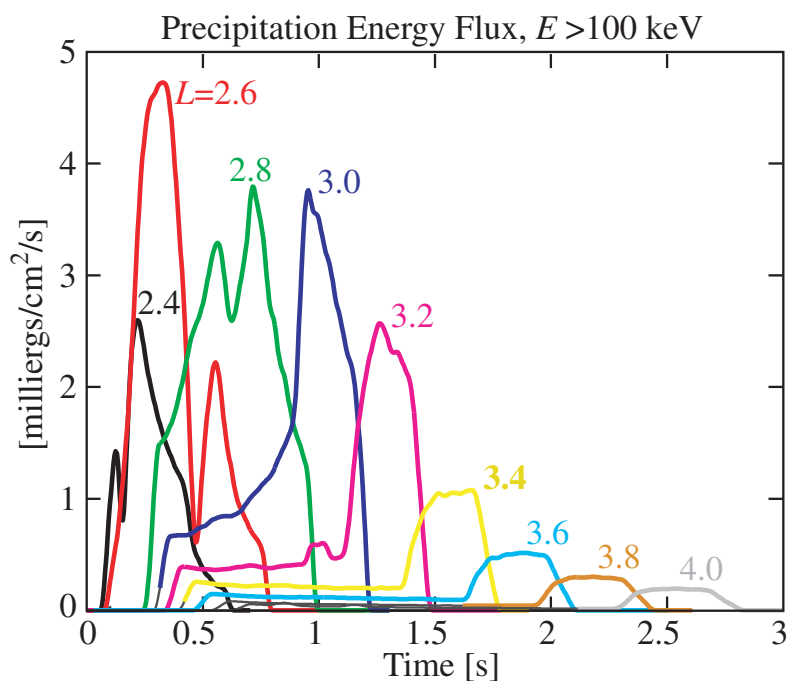
Figure 2.12: *Lauben et al.* [2001] overlay of the theoretical precipitation energy flux profiles evaluated for selected $L$ shells spanning $2.4 < L < 4.0$ at the longitude of the lightning flash.
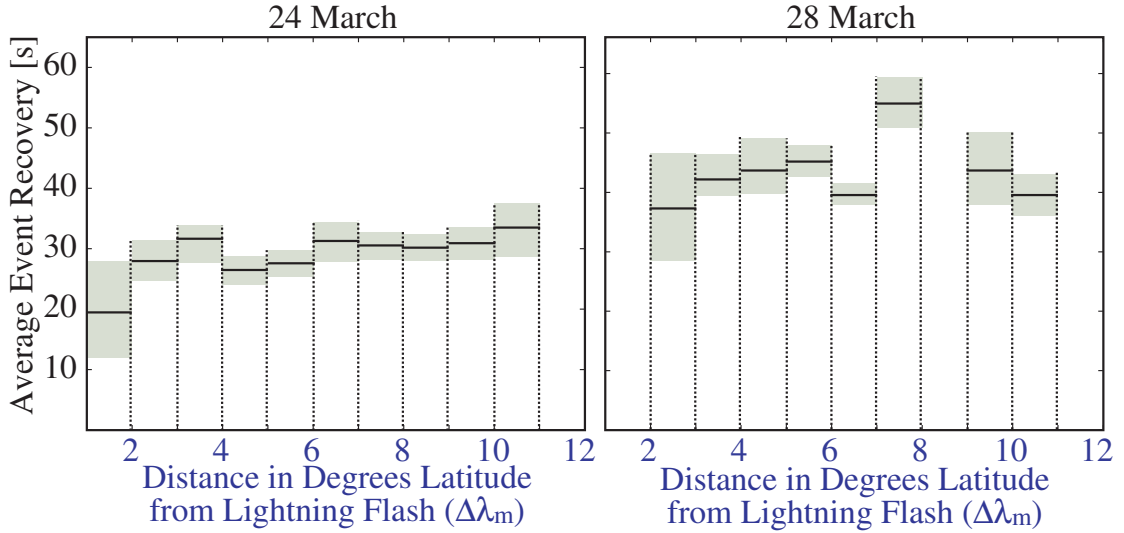
Figure 2.13: Average event recovery time for the LEP events as a function of distance between flash location and great circle path (GCP) for 24 March (left panel) and 28 March 2001. The format is the same as Figures 2.10 and 2.11.

time shows no correlation to the distance from the source lightning, with an absolute correlation coefficient less than 0.4 for both days. This result is not unexpected, since the recovery time is not strongly dependent on the propagation characteristics of the nonducted whistler wave energy or other magnetospheric conditions. Recovery time is essentially the chemical response of the ionosphere to the newly introduced secondary ionization [*Pasko and Inan*, 1994] and is only dependent on the conditions of the ionosphere and the energy spectrum of the precipitating electrons (which in turn determines the altitude at which the secondary ionization is produced). The relatively slow recovery times are consistent with expected relaxation times for secondary ionization produced in the $D$-region [*Glukhov et al.*, 1992]. While the recovery time is nearly constant across the array, it is different on the two days of the study, with a mean value and standard deviation of 28.7±4.2 s on 24 March and 41.1±8.6 s on 28 March. The differences in recovery time on the two days is probably a result of the energy spectrum of precipitation flux, which is determined (to a large degree) by the energy spectrum of the available trapped flux, known to be variable from day to day [*Gaines et al.*, 1995].

## 2.6  Summary

Both of the thunderstorms considered in our statistical analysis contain lightning discharges that induce detectable electron precipitation events that exhibit differential delay patterns consistent with precipitation induced by nonducted whistler waves. Analysis of the high resolution VLF data allows us to quantify several parameters of nonducted whistler-induced precipitation events. Measurements of the onset delay between the causative lightning discharge and the first appearance at the ionosphere of the bursts of electrons precipitated on different field lines show a steadily increasing onset delay with increasing $L$-value, consistent with precipitation induced by nonducted whistlers as previously noted in *Johnson et al.* [1999]. In this paper we show that the dependence of the onset delay on the distance from the causative discharge for LEP events associated with lightning in both storms agrees with previous measurements presented in *Johnson et al.* [1999]. We also show that the onset delays for LEP events associated with lightning flashes occurring in the two storms of different location are measurably different in a manner consistent with theoretical calculations [*Lauben et al.*, 2001]. The absolute values of the measured onset delays are consistently larger than that calculated by the model of *Lauben et al.* [2001]. This is possibly due to the fact that precipitation observed in the northern hemisphere has already mirrored and/or backscattered from the southern hemisphere, as discussed in Section 4.4.

Our analysis additionally allows the assessment of the full spatial extent (in latitude) of the disturbed ionospheric region and the dependence of the magnitude of the VLF perturbation on the distance between the propagating VLF wave and the location of the causative discharge. The precipitation region is shown to be poleward-displaced in geomagnetic latitude with respect to the causative lightning flash, with the VLF perturbation magnitude (and thus presumably the precipitation flux) having an approximately Gaussian profile in latitude with 90% of the precipitation typically occurring over a region with spatial extents of 880±110 km and 990±110 km

respectively for the two cases studied. Differences in the spatial extent and poleward-displacement of the disturbed ionospheric region are found to be discernible for lightning discharges associated with the two different storm locations. We also measure the duration of nonducted LEP events and measure variations in the onset duration with distance of the subionospheric VLF Great Circle Path from the location of the causative discharge. The onset durations also differ for the LEP events associated with lightning occurring in the two different storm locations, once again in a manner consistent with theoretical calculations. Our results additionally indicate a distinct positive correlation between the peak current of cloud-to-ground (CG) lightning discharges and the occurrence rates of nonducted LEP events.

This first statistical analysis of the perturbations of VLF signals caused by nonducted whistler-induced electron precipitation yields a quantification of the temporal and spatial signatures of LEP events. The events are typified by a linear increase in onset delay and duration with increasing $L$-shell, while the recovery time is independent of latitude over the range of latitudes covered by the HAIL array. The latitudinal variation of onset delay agreed with previous observations presented in *Johnson et al.* [1999]. The two case studies presented here concern storms located at different latitudes. For the case where causative discharges are located at lower latitudes (28 March 2001), the LEP events exhibited shorter onset durations than when the causative discharges are located at higher latitudes (24 March 2001). The LEP events associated with causative discharges located at lower latitudes (28 March 2001) also exhibited less rapidly increasing onset delays and durations with latitude. They also exhibited precipitation in a wider area displaced further poleward from the causative discharge. The qualitative spatial and temporal characteristics are in general agreement with both previous measurements and theoretical calculations.

This chapter dealt exclusively with VLF signal perturbations associated with LEP events. The following chapters undertake theoretical modeling to relate these observations of VLF signal perturbations to the associated electron precipitation events and ionospheric disturbances.

This page intentionally left blank.

# Chapter 3

# Model Framework for LEP Events

## 3.1  Introduction

The previous chapter describes the temporal and spatial signatures of VLF signal perturbations associated with LEP events as detected on the HAIL array. We now quantitatively relate the VLF signal perturbations to the ionospheric disturbance and electron precipitation that cause the VLF signal perturbations.

Through a comparison of VLF experimental observations of two representative LEP events with a comprehensive model of lightning-induced electron precipitation and the resulting ionospheric disturbance, we will examine the use of VLF remote sensing to quantitatively measure the precipitating flux associated with LEP events. In doing so, we demonstrate the usefulness of VLF remote sensing in accurately characterizing precipitation events and ionospheric electron density enhancements.

This chapter provides the details of the framework used to model the lightning-induced electron precipitation, resulting ionospheric disturbance, and VLF signal perturbation, with the output of the modeling framework directly comparable to the HAIL observations. This modeling framework is also described in *Peter and Inan* [2007].

Table 3.1: Case Parameters

| Case | Date | Time [UT] | Latitude | Longitude | Peak Current | $L_{pp}$ |
|------|------|-----------|----------|-----------|--------------|----------|
| 1 | 24 Mar 2001 | 07:13:20.68 | 33.34°N | 100.06°W | +133.3 kA | 3.45 |
| 2 | 28 Mar 2001 | 07:09:47.86 | 30.19°N | 95.73°W | -155.1 kA | 2.84 |

## 3.2   Description of the Two Case Studies

This chapter considers two representative LEP events detected by the Holographic Array for Ionospheric/Lightning Research (HAIL), which are chosen based on their clear VLF signatures, their occurrence at a similar time of night and year, and the existence of a previous statistical work that included both events (Chapter 2). Figures 3.1 and 3.2 show three-minute records of the NAA and NAU VLF signal amplitudes received at the HAIL sites in operation during each case, with a map showing the location of the relevant HAIL sites and GCPs. Note that the paths with the peak perturbation (i.e., NAA-WA for Case 1 and NAU-PK for Case 2), are poleward displaced from the causative flash location, typical of nonducted LEP events [*Johnson et al.*, 1999] and as discussed in Chapter 2. No perturbation is detected on the northernmost and southernmost GCPs, so that the full latitudinal extent of the ionospheric perturbation region is captured in both cases.

The National Lightning Detection Network (NLDN) provides the timing, location and peak current of causative cloud-to-ground (CG) lightning discharges within the continental United States with one-ms resolution [*Cummins et al.*, 1998], as described in Chapter 2. The correlation of the specific causative lightning flash in the NLDN data with the VLF perturbation observed on HAIL is reported in *Peter and Inan* [2004]. The first case is induced by a +133.3 kA CG flash, located in northern Texas, at 07:13:20.68 on 24 March 2001. The second case is induced by a -155.1 kA CG flash, located ∼300 km south of the Case 1 flash, at 07:09:47.86 UT on 28 March 2001. Table 3.1 lists the relevant parameters for the two cases.
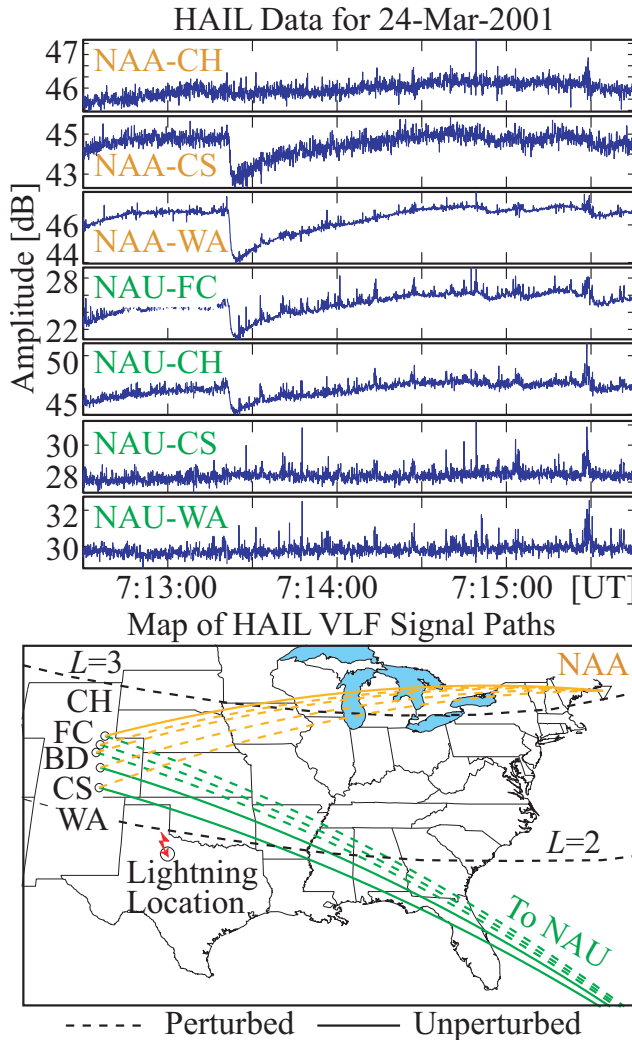
Figure 3.1: VLF signatures of Case 1 LEP event. (Top) Case 1 LEP event observed on 24 March 2001, the same event shown in Figure 2.5. A three-minute record of the NAA and NAU signal amplitude (in dB) at five HAIL sites (not all signals shown). (Bottom) Map showing the GCPs from the two VLF transmitters to each HAIL site. An associated VLF perturbation is detected on the dashed GCPs, and no measurable perturbation is detected on the solid GCPs.
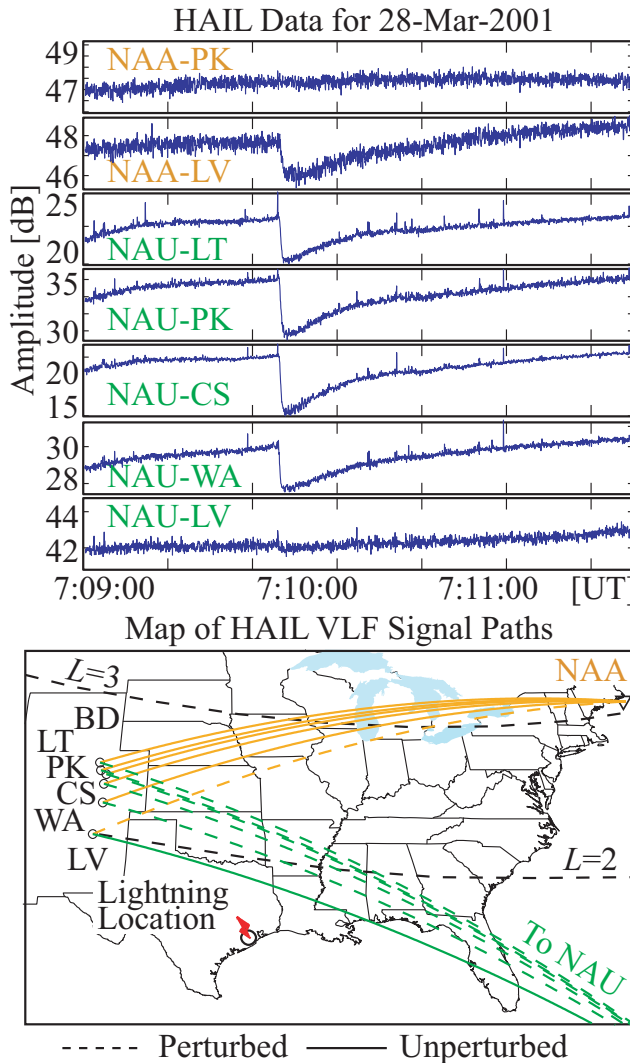
Figure 3.2: VLF signatures of Case 2 LEP event. (Top) Case 2 LEP event observed on 28 March 2001. A three-minute record of the received NAA and NAU signal amplitude at six HAIL sites. (Bottom) A map showing the perturbed GCPs (dashed lines), and those GCPs with no measurable perturbation (solid lines). For both events, the full latitudinal extent of the LEP precipitation region is captured.

## 3.3 Description of Model

The theoretical model framework used in this dissertation is made up of three major components: a model of whistler-induced electron precipitation [*Bortnik et al.*, 2006a]; a Monte Carlo simulation of the energy deposition into the ionosphere resulting from the calculated precipitation flux [*Lehtinen et al.*, 2001]; and a model of VLF subionospheric signal propagation that takes into account the disturbed ionospheric density profiles [*Chevalier and Inan*, 2006]. The model outputs VLF signal perturbations that are compared directly to the VLF signal perturbations observed on the HAIL array. A block diagram of the framework used to model the two representative LEP events is shown in Figure 3.3.

The lightning discharge is modeled in the same manner as *Bortnik et al.* [2002], using the expression of *Uman* [1984, p.61]. The power spectral density is directly proportional to the square of the peak vertical current (taken from NLDN data and listed in Table 3.1), and falls off with the square of distance from the lightning location. The computed wave power density is translated to ∼1000 km altitude, the point of injection of the rays, by properly attenuating it according to an absorption factor taken from [Fig. 3-35 of *Helliwell*, 1965]. The magnitude of the whistler-mode wave magnetic field is directly proportional to the peak vertical current of the lightning flash. The wave normal vectors input into the model are initially vertical, assuming no horizontal density gradients in the ionosphere.

### 3.3.1 Whistler-Induced Precipitation Model

Whistler wave propagation in the magnetosphere is simulated using the Stanford VLF ray tracing code [*Inan and Bell*, 1977], which is essentially an implementation of a two-dimensional integration of Haselgrove's equations [*Haselgrove*, 1954]. A tilted, centered dipole geomagnetic field model is used. The effects of Landau damping are included using the theoretical formulation of *Brinca* [1972] in conjunction with typical suprathermal electron distributions observed by the HYDRA instrument on the Polar spacecraft [*Bell et al.*, 2002]. The initial whistler wave packet is injected at 1000 km, with a pulse length of ∼200 ms [*Bortnik et al.*, 2006a], consistent with

**Whistler-Induced**
**Precipitation**
**Model**

**Electron**
**Precipitation**

**Monte Carlo**
**Model**

**Ionospheric Density**
**Enhancement**

**FDFD**
**Model**

**VLF Signal**
**Perturbations**
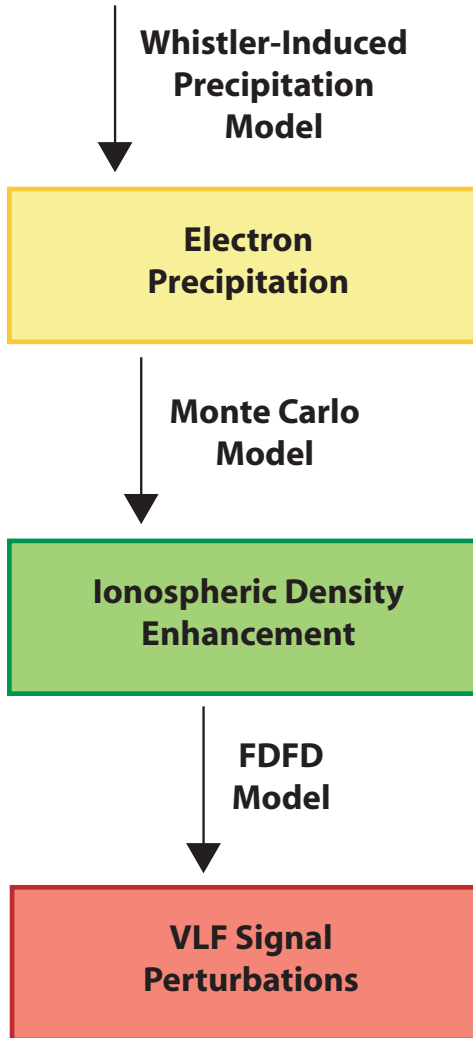
Figure 3.3: Block diagram showing the framework of the LEP model. The theoretical model framework is made up of three major components: a model of whistler-induced electron precipitation [*Bortnik et al.*, 2006a]; a Monte Carlo simulation of the energy deposition into the ionosphere resulting from the calculated precipitation flux [*Lehtinen et al.*, 2001]; and a model of VLF subionospheric signal propagation that takes into account the disturbed ionospheric density profiles [*Chevalier and Inan*, 2006].
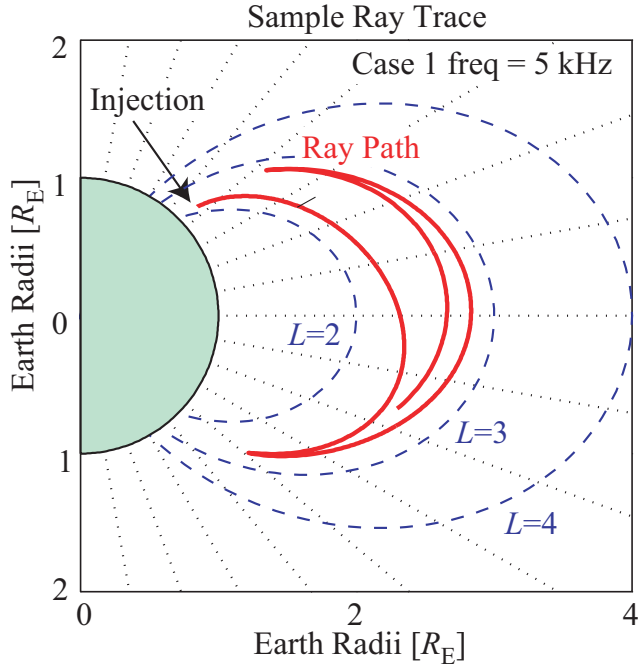
## Sample Ray Trace

Figure 3.4: A sample ray (shown in red) as traced by the Stanford 2-D VLF ray tracing code [*Inan and Bell*, 1977], for the Case 1 lightning location and a frequency of 5 kHz. This is one of thousands of rays used in the model. Notice the propagation of the whistler wave across the Earth's magnetic field lines, and the magnetospheric reflection (MR) of the wave energy.

a typical lightning waveform [Ch. 4, *Uman*, 1984]. A sample ray (one of thousands injected) is traced in Figure 3.4. This is one of thousands of rays used in the model.

### Plasmaspheric Density

Variations in the cold plasmaspheric electron density can significantly influence the propagation of lightning-generated whistler waves. Steeper radial gradients in plasmaspheric density constrain the wave energy to lower $L$-shells. Higher absolute values in plasmaspheric density slow the propagation of whistler waves, with the speed of propagation being approximately inversely proportional to the square root of density [*Park*, 1972]. The equatorial density profile adapted for our use (Figure 3.5) is based on the work of *Tarcsai et al.* [1988]. The *Carpenter and Anderson* [1992] model (also
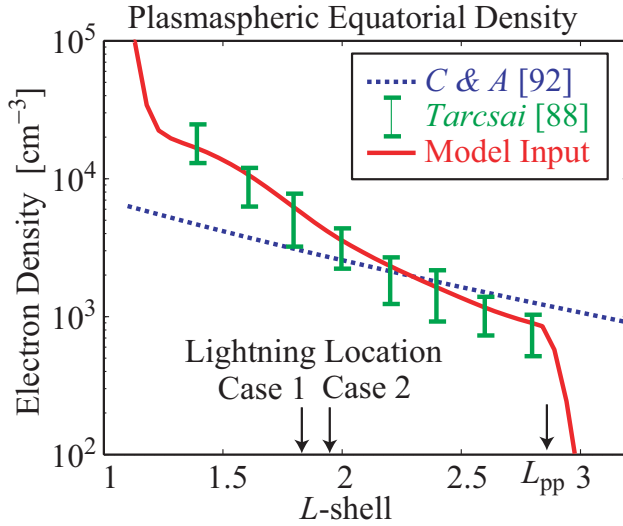
Figure 3.5: Equatorial cold plasmaspheric electron density used in the model, shown in red. The *Tarcsai et al.* [1988] and *Carpenter and Anderson* [1992] models are shown for reference. The plasmapause location is determined from the EUV IMAGE satellite data, with the Case 2 $L_{pp}$ shown.

shown for reference) is intended for use for $L > 2.5$. Using the equatorial density based on *Carpenter and Anderson* [1992], the model calculates the electron precipitation to be displaced significantly further poleward from the lightning flash than that which is observed on the HAIL array [*Bortnik et al.*, 2006b]. Using the equatorial density based on *Tarcsai et al.* [1988], the model calculates a precipitation location in excellent agreement with the location of the HAIL disturbances observed (Figure 4.4), suggesting that the *Tarcsai et al.* [1988] model estimates the plasmaspheric density gradients at lower $L$-shells more accurately than *Carpenter and Anderson* [1992]. This result is expected since the *Carpenter and Anderson* [1992] model is largely based on in-situ and whistler data from relatively higher $L$-shells, while the *Tarcsai et al.* [1988] model is at least partly based on observations of whistlers at very low latitudes. The dependence of the poleward displacement on the plasmaspheric density gradients suggests the possible use of VLF remote sensing of precipitation events as an indicator of the radial variation in plasmaspheric density.
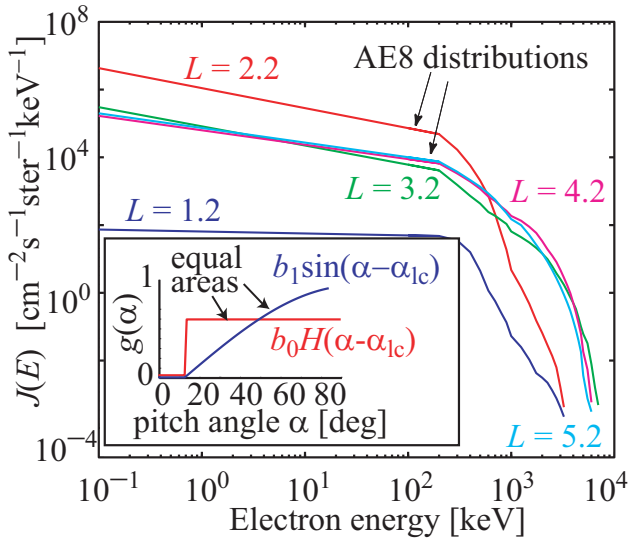
Figure 3.6: Trapped energetic electron flux levels based on the AE8 model [*Vette*, 1991] at $L$=1.2, 2.2, 3.2, 4.2, and 5.2. The inset shows a "square" and "sine" pitch-angle distribution. $H$ denotes the Heaviside step function. Figure modified from *Bortnik* [2004].

Geomagnetic activity increased in the later half of March 2001, resulting in relatively compressed plasmapause locations of $L_{pp}$∼3.45 for Case 1 and $L_{pp}$∼2.84 for Case 2 (Table 3.1). The plasmapause locations are estimated from EUV IMAGE data [courtesy of *M. Spasojevic*, 2006]. The variation of electron number density along the field lines is calculated using the diffusive equilibrium model of *Angerami and Thomas* [1964]. The presence of plasmaspheric ducts of enhanced electron density can be used in the model, but previous modeling has showed that the majority of whistler wave energy is not trapped by the ducts [*Bortnik et al.*, 2003b], and accordingly no plasmaspheric ducts are included in the present model.

**Trapped Energetic Flux**

The precipitated flux induced by lightning-generated whistlers is highly sensitive to the flux levels and initial pitch angle distribution of the trapped electron population, especially near the edge of the bounce loss cone [*Inan et al.*, 1982, 1989]. The trapped energetic flux levels we use (Figure 3.6) are based on the AE8 radiation belt model

[*Vette*, 1991].  However, the trapped flux levels for $L>2$ are known to vary considerably with time, especially during geomagnetically active periods such as those during the two cases considered here. Given this variability of energetic flux levels with $L$-shell, differences between the model and observation are expected in terms of the spatial characteristics (e.g., $L$-dependence) and the absolute magnitude (i.e., flux) of the precipitation.

In fact, the NOAA-POES satellites observed a dramatic increase in the trapped energetic flux levels near the loss cone during the later half of March 2001 (Figure 2.3).  The AE8 radiation belt model assumes a "sine" pitch-angle distribution (as illustrated in the inset).  To account for the increase in particle flux near the loss cone observed by the NOAA-POES satellites, an initial unperturbed "square" pitch-angle distribution is input into the model, scaled by $b_0$ to give an equal number of total particles for both pitch angle distributions.  Modeling results using a "sine" pitch angle distribution (not shown) calculate VLF signal perturbations two orders of magnitude less than those observed, suggesting that the pitch angle distribution near the loss cone is more similar to that represented by the "square" distribution during the two cases.  In this context, it is important to note that for the parameters of typical whistler wave intensities and in the inner radiation belt and slot regions, the wave-induced scattering involves basically weak diffusion (or small angle scattering), and that the precipitation fluxes are thus simply proportional to the flux levels near the loss cone edge [*Inan et al.*, 1982, 1989; *Bortnik et al.*, 2002]. It should be stressed that our purpose here is to develop metrics to quantitatively relate the observed VLF perturbation signatures to the associated electron precipitation, rather than to determine whether a given trapped flux level or near-loss-cone distribution is more reasonable than another.

**Pitch Angle Scattering**

The pitch angle scattering of energetic particles into the loss cone by cyclotron resonance with whistler waves is calculated according to the work of *Bortnik et al.* [2006a].

The rate of pitch-angle change of a particle moving through an oblique whistler wavefield is determined from the relativistic gyro-averaged equations of motion for a general harmonic resonance [*Bell*, 1984; *Jasna*, 1993], with the first five resonant modes considered [*Bortnik et al.*, 2006a]. Nonlinearities due to wave forces are not included. Typical errors between the analytical solution used and the full solution are <1% for near-resonant particle velocities [*Bortnik et al.*, 2006a].

The combination of the ray tracing simulation and the scattering calculation returns precipitation flux as a function of $L$-shell and time at the geomagnetic longitude of the source lightning flash. All particles scattered into the bounce loss cone are counted as precipitation flux (see Figure 4.1), with the resulting energy deposition into the atmosphere determined as described in Section 3.3.2. It is assumed that there are no longitudinal gradients in ionospheric or plasmaspheric density, and the longitudinal variation of the precipitation flux is simply scaled according to the falloff in lightning-generated electromagnetic energy with the distance from the flash longitude [*Bortnik et al.*, 2003b, Eqn. 1], allowing the determination of precipitation flux as a function of longitudinal displacement from the source lightning longitude [*Bortnik et al.*, 2006b, Fig. 6].

### 3.3.2 Monte Carlo Deposition

The calculated precipitation flux (determined as a function of incident particle energy) is subsequently input into a Monte Carlo simulation of the penetration of energetic electrons into the ionosphere to determine the energy deposition (and secondary ionization production) as a function of $L$-shell and altitude [*Lehtinen et al.*, 2001]. While it would be possible to calculate a specific perturbed pitch angle distribution for different particle energies, locations and times, a single perturbed pitch angle distribution is assumed for all energies, times, and locations to simplify the calculations. The perturbed pitch angle distribution (Figure 3.7a) used in all of our modeling is thus based on the modeling work of *Inan et al.* [1989]. Figure 3.7b shows this pitch angle distribution mapped down to 120 km altitude (the point of injection into the Monte Carlo simulation). Figure 3.7c shows the dependence of the percentage of the particle

energy deposited into the atmosphere on particle pitch angle. Particles nearly perpendicular to the geomagnetic field at 120 km are more likely to be reflected prior to losing all their energy in collisions with atmospheric constituents, resulting in lower average energy deposition.

It should be noted that the *Inan et al.* [1989] pitch angle distribution is calculated from a model of ducted whistler induced precipitation, rather than nonducted whistler induced precipitation. However, given that the initial, unperturbed pitch angle distribution is unknown (assumed here to be square), and that particles are unlikely to be scattered far into the loss cone (i.e., the wave-induced scattering involves basically weak diffusion or small-angle scattering for both ducted and nonducted interactions), the use of the *Inan et al.* [1989] distribution provides a sufficiently accurate representation of the effect of the precipitation events on the ionosphere.

The altitude of energy deposition in the ionosphere is highly dependent on the energy of the precipitating particle. Figure 3.8 shows the energy deposition as a function of altitude for particles of four different energies precipitated at $L$=2.5. Higher energy particles by definition deposit more total energy per particle, and they deposit relatively more energy at lower altitudes [*Banks et al.*, 1974]. Also note that particles in the 100-300 keV range deposit the majority of their energy at $\sim$85 km, the inferred nighttime reflection height for VLF signals [*Wait and Spies*, 1964].

Using the precipitation flux (a function of $L$-shell and longitude) as an input for the Monte Carlo simulation, a three-dimensional map (altitude, longitude, and $L$-shell) of energy deposition is determined. The resulting electron density enhancement is calculated assuming one ion-electron pair is produced per 35 eV deposited [*Rees*, 1963]. It should be noted that relaxation processes are not considered in the model and typically occur on the timescales of 10-100 seconds in the mid-latitude $D$-region ionosphere [*Glukhov et al.*, 1992]. As the majority of the precipitation for the two cases occurs within the first five seconds (i.e., the onset durations are no longer than a few seconds), it is assumed the relaxation of the ionosphere does not significantly change the results presented.

The electron density enhancement is added to an ambient nighttime density profile (profile 2 in Figure 4 of *Pasko and Inan* [1994]) to give the modified ionospheric density
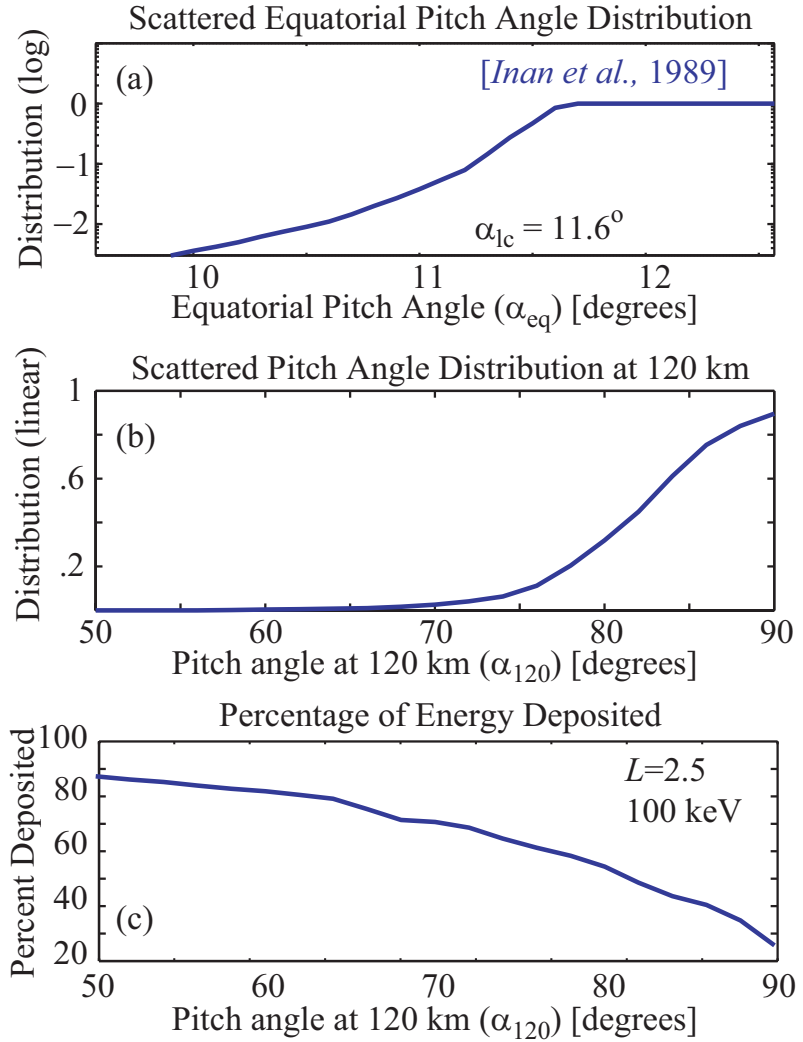
Figure 3.7: Scattered pitch angle distribution. (a) Scattered equatorial pitch angle distribution for precipitating particles at $L$=2.5, taken from *Inan et al.* [1989]. (b) The scattered pitch angle distribution mapped down to 120 km. (c) Percent of energy deposited into the atmosphere for a 100 keV particle as a function of pitch angle at 120 km and $L$=2.5.
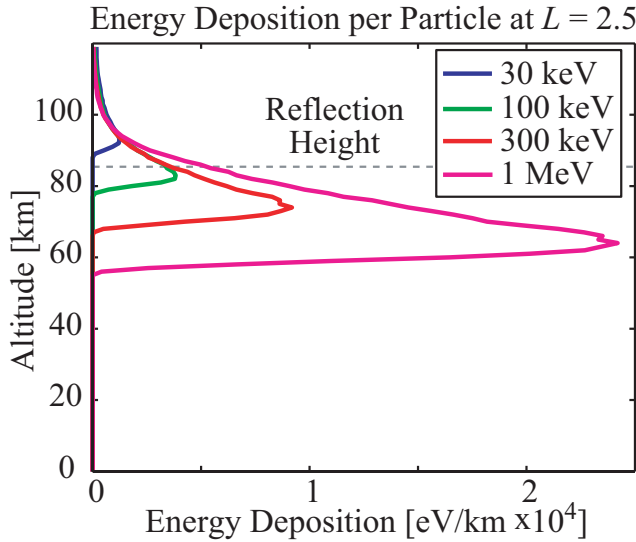
Figure 3.8: Energy deposition per particle, as a function of altitude, for electrons of four different energies at $L$=2.5. The precipitation is assumed to have the pitch angle distribution given in Figure 3.7a.

profile as a function of $L$-shell (sampled every 0.1 $L$), longitude (sampled every 0.5 degrees), and altitude (sampled every 1 km). The variation in ionospheric density along the GCP of the propagating VLF signal is then input into a model of VLF signal propagation.

### 3.3.3   VLF Signal Propagation

The ionospheric density along each GCP monitored by the HAIL array is input into a new Finite Difference Frequency Domain (FDFD) model of subionospheric VLF signal propagation [*Chevalier and Inan*, 2006] to quantitatively relate the ionospheric density enhancements to the measured VLF signal perturbations. The model consists of a 2D grid in cylindrical coordinates taking into account the curvature of the Earth. The input parameters into the magnetized plasma equations [*Lee and Kalluri*, 1999] are static magnetic field, ground conductivity, electron-neutral collision frequency, and electron density. For the static magnetic field a tilted dipole model is used [*Walt*, 1994, p.27-31]. The model incorporates variances in the electromagnetic properties of

the ground and seawater where relevant in the region modeled. The electron-neutral collision frequency profile can be varied along the path; for the results shown here a single profile $\nu(z)=4.303\times10^{11}e^{-0.1622z}$ is used, where $\nu$ is in s$^{-1}$ and $z$ is in kilometers. The electron density profile is obtained from the Monte Carlo calculations (after addition to the ambient profile). Due to computational resource constraints, the GCP is broken up into segments (Figure 3.9a), with each segment surrounded with a Perfectly Matched Layer (PML) boundary condition to absorb any outgoing waves [*Chevalier and Inan*, 2006]. Making use of the total field/scattered field methodology [*Taflove and Hagness*, 2000], the VLF signal is then propagated in the forward direction from segment-to-segment along the path.

Figure 3.9b shows the magnitude of the $H_z$ magnetic field (oriented perpendicular to the path of propagation) for the 40.75 kHz NAU signal. The VLF signal reflects at ~85 km, the nighttime reflection height of the $D$-region ionosphere, and is guided along the Earth-ionosphere waveguide. As the wave propagates along the path, the higher-order modes rapidly decay, leaving only the lower order modes at the location of the receiver (Figure 3.9c). As the HAIL receivers measure the wave magnetic field strength at the surface of the Earth, we calculate the amplitude and phase of the wave magnetic field along the entire path at the surface of the Earth (Figure 3.9d). Due to the decay of the higher order modes with distance, the amplitude at the HAIL receiver locations is relatively stable. The affect of the ionospheric disturbance on the magnetic field strength at the location of each HAIL receiver is calculated and compared with the VLF signal perturbations observed.

## 3.4 Summary and Conclusions

In this chapter, we provide the details of the theoretical framework used to model two representative lightning-induced electron precipitation events. This modeling framework is the most comprehensive model to date in terms of quantitative interpretation of VLF signal perturbations associated with nonducted lightning-induced electron precipitation. The model consists of three major components (Figure 3.3): a model of whistler-induced electron precipitation [*Bortnik et al.*, 2006a]; a Monte
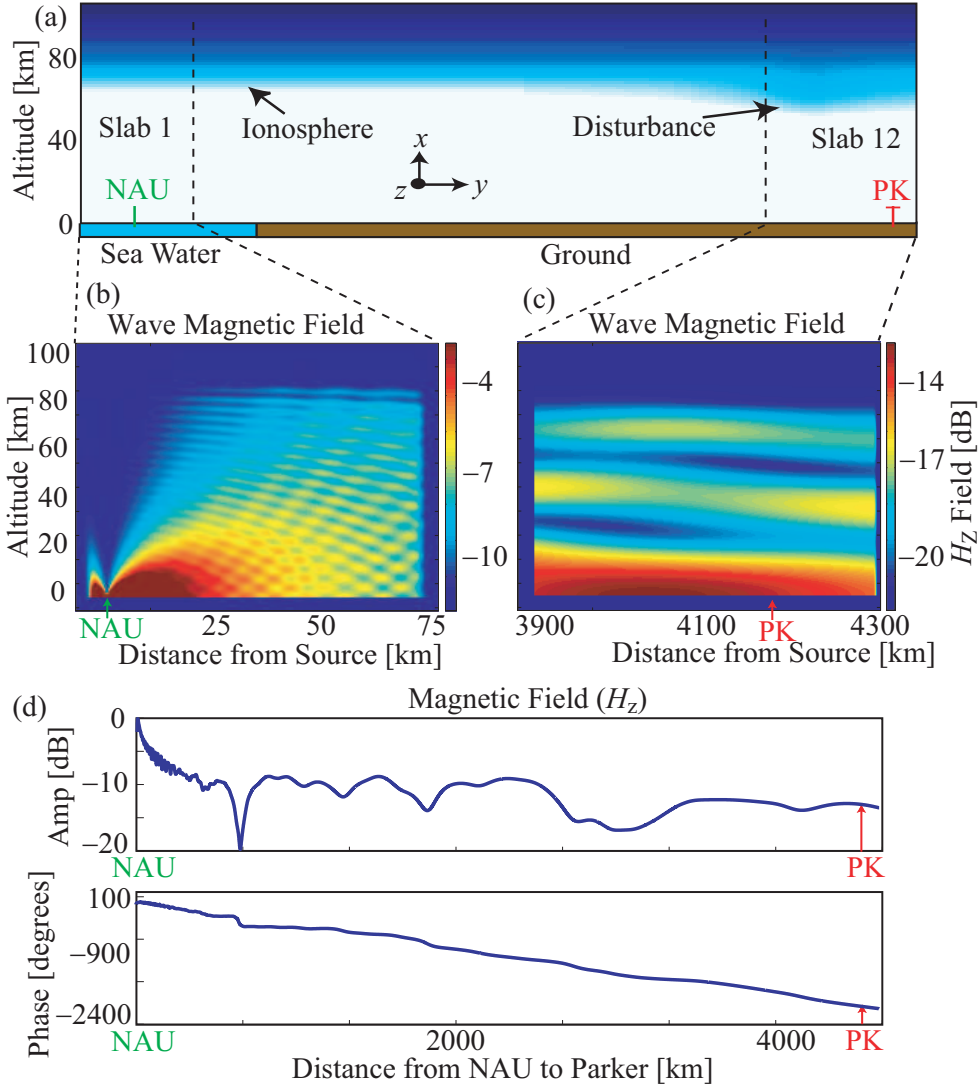
Figure 3.9: Model of VLF signal propagation. (a) Schematic of the Finite Different Frequency Domain (FDFD) fully electromagnetic model of VLF signal propagation, showing the division of the GCP into segments. (b) 2D image of the wave magnetic field $H_z$ (oriented along the path) near the NAU transmitter, measured in dB with respect to the magnetic field at the transmitter. (c) Magnetic field $H_z$ near the Parker (PK) receiver (note the larger region and different color scale than in b). (d) Magnetic field $H_z$ amplitude (top) and phase (bottom) along the GCP from NAU to PK, with respect to the wave magnetic field at the transmitter, for an ambient ionosphere.

Carlo simulation of the energy deposition into the ionosphere resulting from the calculated precipitation flux [*Lehtinen et al.*, 2001]; and a model of VLF subionospheric signal propagation that takes into account the disturbed ionospheric density profiles [*Chevalier and Inan*, 2006]. This modeling framework is easily applicable to precipitation events other than those associated with lightning-generated whistlers. In fact, a similar methodology has already been applied to subionospheric VLF signatures of VLF transmitter-induced precipitation [*Inan et al.*, 2007].

In the next chapter, we apply the modeling framework to two representative LEP events. The VLF amplitude and phase perturbations calculated by the model are compared directly to the VLF signal observations. However, it should be stressed that some of the inputs into the whistler-induced precipitation model are known to be highly variable and not known at the time of the observations. These inputs include the trapped energetic flux levels, the pitch angle distribution of the trapped radiation belt electrons (i.e., the slope of the near-loss-cone distribution), and the cold plasmaspheric electron density. Recognizing that the precipitation is highly dependent on these variables, our objective is to develop metrics with which we can quantitatively relate the precipitation flux to measured VLF signal perturbations, independent of the trapped flux levels. Chapter 5 describes the development of such a methodology by which we can estimate the total precipitation induced by a single lightning flash, independent of trapped radiation belt flux levels and using only the developed metrics and observations of VLF signal perturbations.

This page intentionally left blank.

# Chapter 4

# Comparison of Model and Observations

## 4.1 Introduction

The previous chapter provides the details of a framework used to model lightning-induced electron precipitation events. The model consists of three major components (Figure 3.3): a model of whistler-induced electron precipitation [*Bortnik et al.*, 2006a]; a Monte Carlo simulation of the energy deposition into the ionosphere resulting from the calculated precipitation flux [*Lehtinen et al.*, 2001]; and a model of VLF subionospheric signal propagation that takes into account the disturbed ionospheric density profiles [*Chevalier and Inan*, 2006].

In this chapter, we apply this model framework to two representative LEP events, as described in Section 3.2. We present the calculated electron precipitation induced by the lightning-generated whistler waves, the ionospheric electron density enhancement resulting from this precipitation, and the VLF signal perturbations resulting from the ionospheric disturbance. We directly compare the VLF amplitude and phase perturbations calculated by the model to the VLF signal observations made on HAIL.

## 4.2   Precipitation Flux

As detailed in Chapter 3, the whistler-induced precipitation model calculates differential flux as a function of time, energy, and $L$-shell. Figure 4.1 shows the differential flux at $L$=2.5 for both cases. Lower energy precipitation, associated with Landau resonance between the whistler wave and the energetic electrons, persists for longer times ($\sim$10 seconds) than the higher energy precipitation ($>$30 keV), induced as a result of cyclotron resonance pitch angle scattering by the propagating whistler wave. The majority of the high-energy precipitation occurs within the first five seconds. The duration of precipitation is lengthened by the presence of magnetospherically reflecting (MR) whistlers, consistent with past modeling [*Bortnik et al.*, 2003b], and is considerably longer than that assumed in past works [*Rodger et al.*, 2002]. The compressed plasmapause ($L_{pp}\sim$2.84 for Case 1 and $L_{pp}\sim$3.45 for Case 2) results in guiding of whistler wave energy at the steep plasmapause gradient [*Inan and Bell*, 1977].

Integrating the differential number flux (Figure 4.1a) over time gives the energy spectrum of the total precipitated flux through 0.5, 1, 2, and 5 seconds (Figure 4.1b). Significant precipitation of lower energy ($<$10 keV) electrons continues through five seconds. The majority of the higher energy electron precipitation ($>$100 keV), those energies most important in altering the $D$-region ionosphere (Figure 3.8), occurs within the first two seconds.

As we use the same radiation belt model (Section 3.3.1) as that used in the model of *Bortnik et al.* [2006a,b], we expect the precipitation calculated by our model runs to be comparable to the results reported in *Bortnik et al.* [2006a,b]. To directly compare our results with *Bortnik et al.* [2006a,b], we calculate the precipitated energy flux ($E>$45 keV), which peaks at $\sim$1$\times$10$^{-2}$ [ergs s$^{-1}$cm$^{-2}$] at $L \sim$2.4 for Case 1 and $L\sim$2.2 for Case 2. This peak flux is approximately ten times larger than the peak energy flux calculated for LEP events in *Bortnik et al.* [2006b]. However, this difference is simply due to the differences in the intensity of causative lightning flashes considered. Noting that the peak lightning flash currents for the two cases considered here (Table 3.1) are more than ten times larger than the 10.53 kA peak current used in *Bortnik*
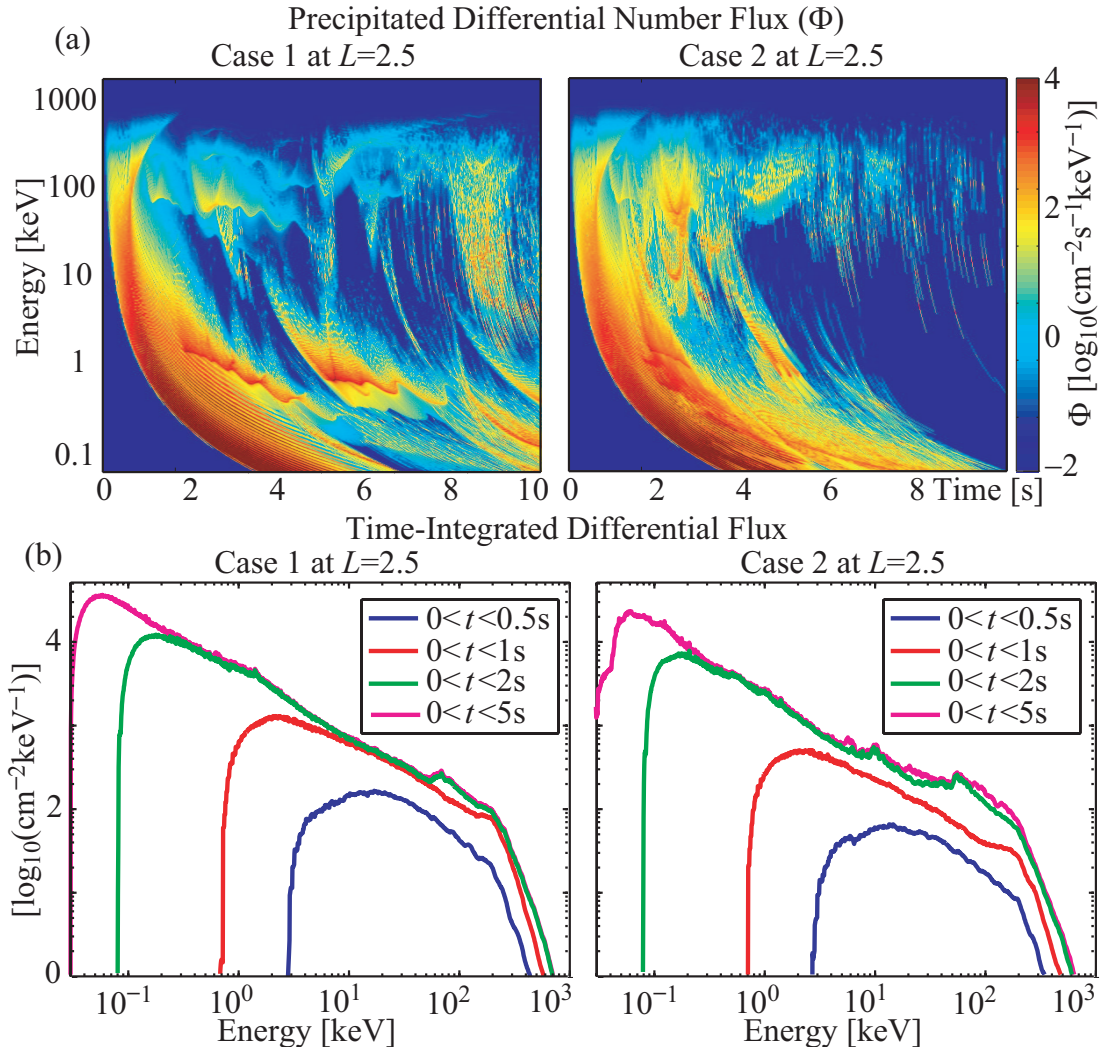
Figure 4.1: Differential number flux. (a) Differential flux as a function of time and energy at $L$=2.5 from 10 eV to 1 MeV for both cases. The higher energy precipitation is induced by cyclotron resonance pitch angle scattering by the propagating whistler wave. Time equals zero at the time of the causative lightning flash. (b) Time-integrated differential flux as a function of energy integrated over 0.5, 1, 2, and 5 seconds at $L$=2.5 for both cases.

*et al.* [2006b], and the whistler wave magnetic field amplitude produced is directly proportional to the peak lightning current input into the model, the results are in good agreement. Consistent with *Bortnik et al.* [2006b], the majority ($>70\%$) of the energy flux is carried by 100-300 keV electrons.

## 4.3   Ionospheric Density Enhancement

The time-integrated differential number flux (Figure 4.1b) is input into the Monte Carlo simulation of energy deposition (see Section 3.2). The resulting energy deposition at $t=2$s and $L=2.5$ as a function of altitude is shown in Figure 4.2. The maximum in energy deposited is at $\sim$85 km altitude, the inferred nighttime reflection height for VLF subionospheric signals. The resulting electron density enhancement is calculated assuming one ion-electron pair is produced per 35 eV deposited [*Rees*, 1963]. The peak density enhancement at $\sim$85 km is $\sim$15% of the ambient profile for both cases, consistent with previous modeling of ionospheric disturbances associated with LEP events [*Clilverd et al.*, 2002; *Rodger et al.*, 2002; *Lev-Tov et al.*, 1995].

Figure 4.3b shows a three dimensional image of the time-integrated electron density enhancement as a function of $L$-shell, longitudinal displacement from the lightning source, and altitude. For both cases, the enhancement region is centered at $\sim$85 km and at the longitude of the lightning flash. The enhancement region is peaked at higher $L$-shells in Case 1 ($L\sim$2.3) than in Case 2 ($L\sim$2.1), due to the different lightning source location.

Taking the horizontal plane through the 3-D image gives the time-integrated density enhancement at 85 km (as a function of longitude and $L$-shell), which is superimposed on a map of the VLF signal paths (Figure 4.4). As 85 km is near the VLF nighttime reflection height, the density enhancement at 85 km gives a reliable indication of the VLF perturbations expected for each HAIL path. The region of density enhancement agrees qualitatively with the perturbations observed on the HAIL array, with both the poleward displacement and spatial extent consistent with observations. This agreement suggests that the plasmaspheric density profile used in the model (Figure 3.5) is similar to that in effect during the two cases.
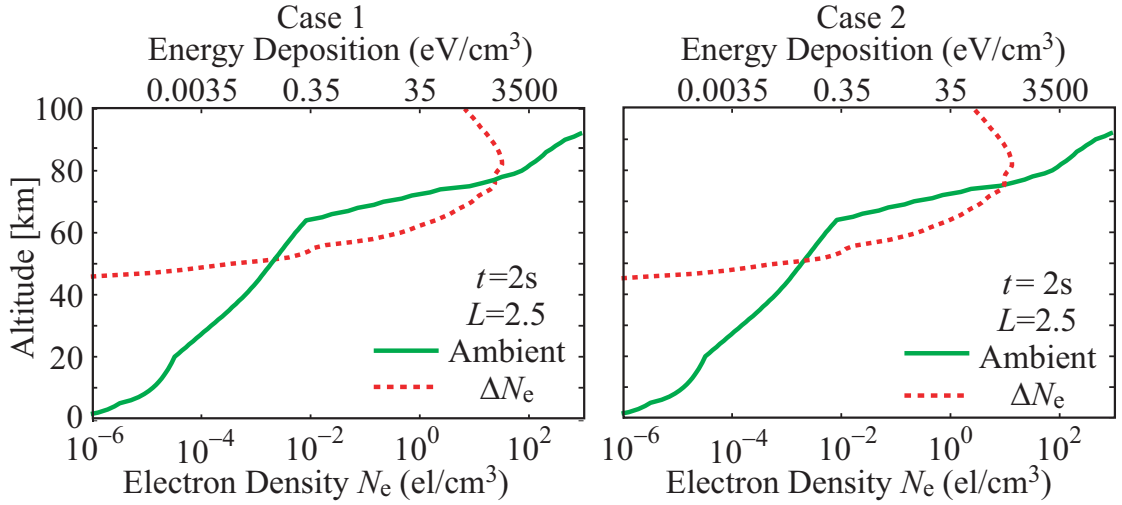
Figure 4.2: Energy deposition and ionospheric electron density enhancement. Total energy deposited into the ionosphere, and resulting electron density enhancement, at $L=2.5$ and $t=2$ seconds for both cases. The disturbed ionospheric density profile is calculated by adding the electron density enhancement to the ambient ionospheric density profile (profile 2 in Figure 4 of *Pasko and Inan* [1994]).
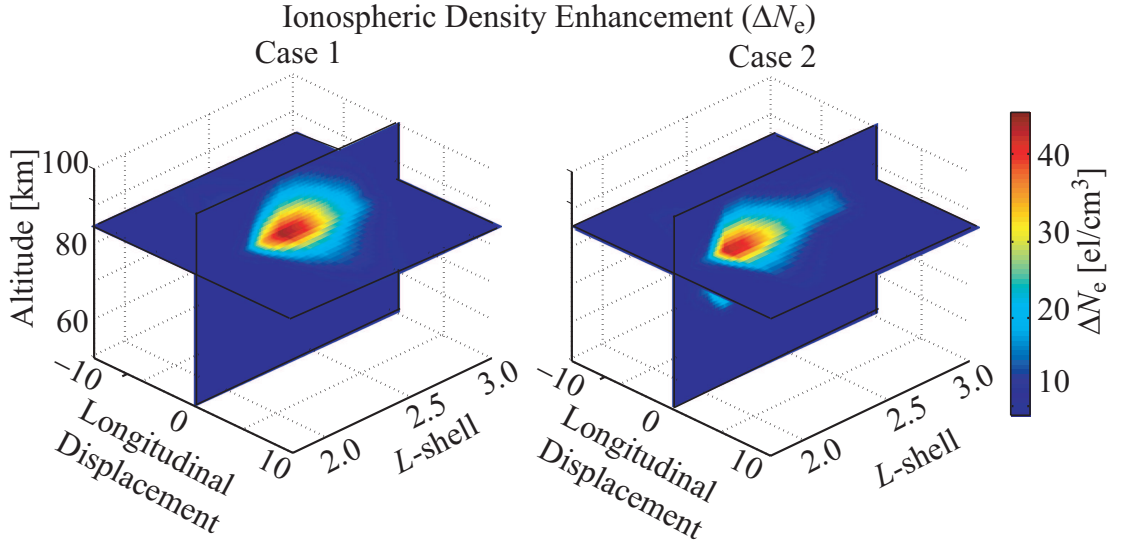


Figure 4.3: Ionospheric density enhancement. 3D plot of electron density enhancement at $t=2$s. Two planes dissect the image at an altitude of 85 km and at 0° longitudinal displacement from the lightning source.

Ionospheric Density Enhancement ($\Delta N_e$) at 85 km
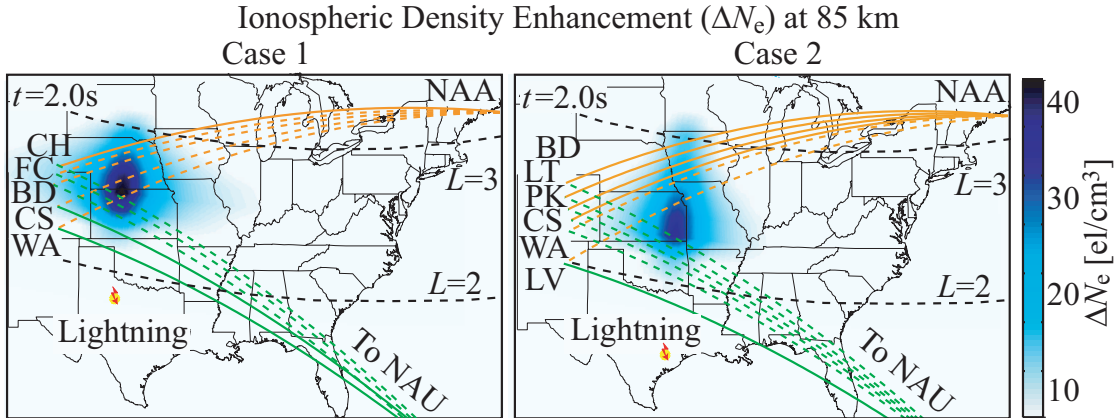


Figure 4.4: Ionospheric density enhancement at 85 km. 2D plot of electron density enhancement for both cases at $t$=2s and 85 km, superimposed on a map of the HAIL array. The dashed lines represent GCPs on which a detectable perturbation is observed. There is excellent qualitative agreement between the location of the ionospheric disturbance calculated by the model and VLF signal perturbations observed on HAIL.

## 4.4 VLF Signal Perturbations

The FDFD model of VLF signal propagation (described in Section 3.3.3) is used to quantitatively relate the effects of the density enhancement on the VLF signals recorded at HAIL. The FDFD simulation is initially performed with an ambient ionospheric profile, giving an ambient amplitude and phase for each HAIL path. The disturbed ionospheric density profile (Figure 4.3) along the GCP is then input into the FDFD model, and the perturbed amplitude and phase is compared to the ambient amplitude and phase to determine the perturbation change in amplitude and phase. The perturbation in amplitude and phase calculated by the model is then directly compared to the HAIL VLF signal observations.

Figure 4.5 show six-second snapshots of the VLF signal amplitude and phase recorded by HAIL for Case 1. The time delay between the lightning flash and onset of perturbation increases with latitude, consistent with the effect previously referred to as "differential delay" (Section 1.3.2). Overlaid in red are the VLF signal perturbations calculated by the model. Top to bottom corresponds to increasing time,
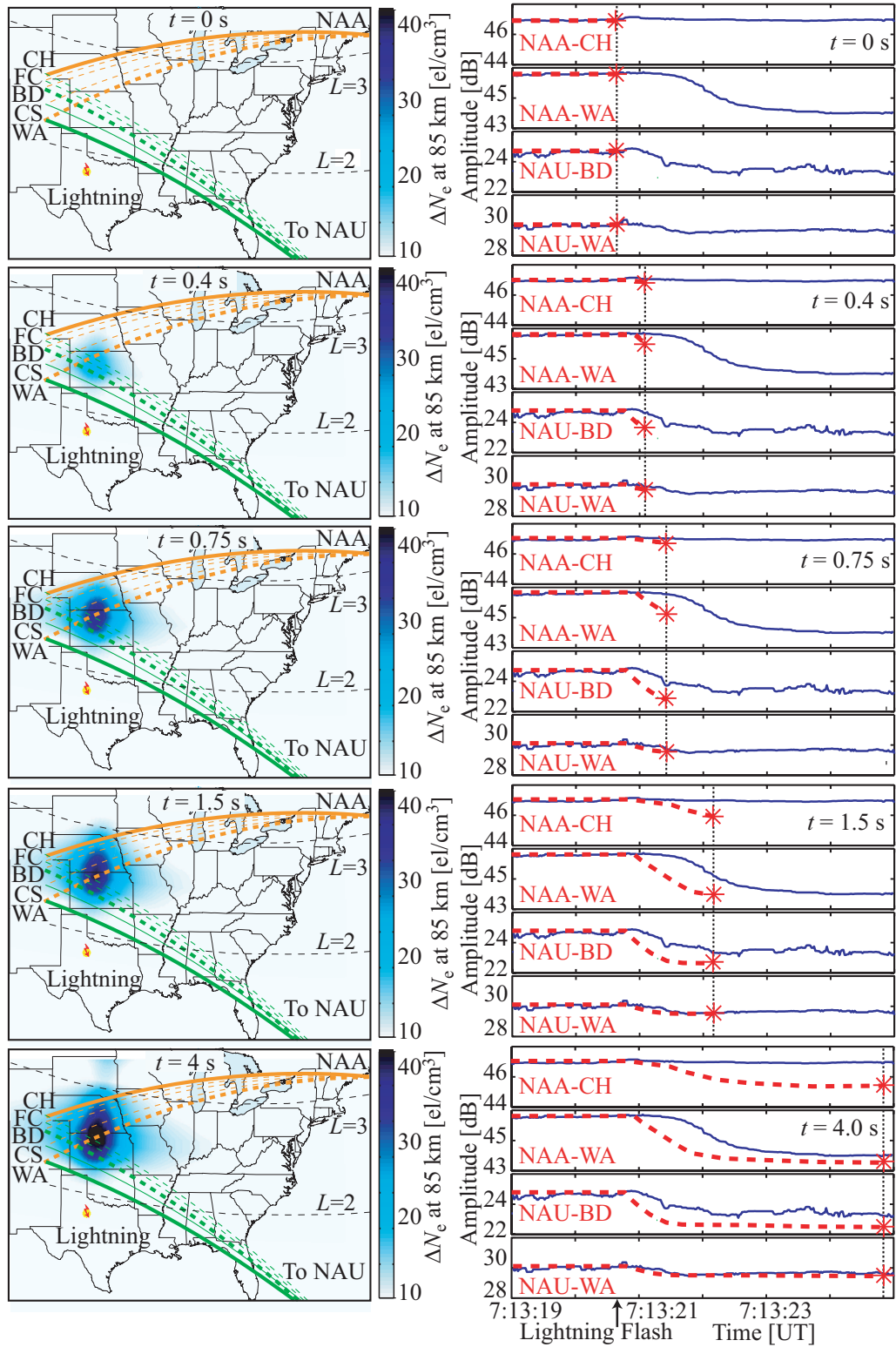
Figure 4.5: [Previous Page] Snapshots of density enhancement and VLF perturbations for Case 1. The left hand panels show 2D plots of electron density enhancement for Case 1 at 85 km, superimposed on a map of the HAIL array. The right hand panels show (in blue) six-second snapshots of four VLF signal amplitudes for Case 1, filtered with a 20-point median filter. The four signals correspond to the thick GCPs on the maps to the left. Overlaid in red are the VLF signal perturbations calculated by the model for Case 1 as a function of time. The top to bottom panels correspond to $t$=0, 0.4, 0.75, 1.5, and 4 seconds, with $t$=0 seconds corresponding to the time of the lightning flash. The vertical dashed black lines denote the time, and the red asterisks denote the calculated VLF signal amplitude perturbation.

showing the amplitude perturbation calculated by the model at $t$=0, 0.4, 0.75, 1.5 and 4 seconds, where $t$=0 seconds corresponds to the time of the causative lightning flash. The model calculations show the characteristic VLF signatures of LEP events. The left hand panels show 2D plots of electron density enhancement for Case 1 at 85 km, superimposed on maps of the HAIL array. The top to bottom panels show snapshots at increasing time, with the deposition of energy moving to higher $L$-shells with time, consistent with previous observations of nonducted LEP events [*Peter and Inan*, 2004]. The onset duration (as defined in *Peter and Inan* [2004] and corresponding to the time over which significant precipitation occurs) calculated by the model is comparable to the VLF observations. The simulation results show a differential delay consistent with the observations. The onset delay, as measured by the HAIL array and averaged for over 70 LEP events observed on 24 March 2001, increases linearly with latitude (Figure 2.10). For the $\sim$70 events included in that statistical analysis, of which the Case 1 LEP event is included, the onset delay is calculated to increase 0.15±0.05 seconds per degree in latitude ($1.4 \pm 0.5 \times 10^{-3}$ s/km). The theoretical model calculates an onset delay for the Case 1 LEP event that also increases with latitude, albeit at a slightly slower rate of $\sim$0.11 seconds per degree in latitude ($\sim 0.9 \times 10^{-3}$ s/km). The theoretical calculations show a differential delay consistent with the observations; however, the model calculates generally shorter onset delays ($\sim$0.5s) than those observed in the HAIL data ($\sim$1s).

Past modeling work [*Lauben et al.*, 1999; *Bortnik et al.*, 2006a] has consistently calculated shorter onset delays than those observed for the two cases. *Johnson et*

*al.* [1999] reported a number of LEP events detected by the HAIL array, with the causative lightning flashes located in the middle of Texas, and compared the perturbation signatures with a model of nonducted whistler-induced precipitation [*Lauben et al.*, 1999]. In order for the model and observation to agree, the modeled precipitation was delayed ∼0.35s in time, similar to the difference in onset delay between the observations and the model calculations of this work. *Johnson et al.* [1999] attributed this discrepancy to variations in the magnetospheric cold plasma density to values higher than those used in *Lauben et al.* [1999], resulting in longer travel times for both the waves (whistler-mode refractive index is proportional to the square root of electron density) and particles (gyroresonant electron energies are lower for higher values of refractive index).

While it is possible that the plasmaspheric cold plasma densities at the longitudes of the HAIL array are significantly higher than those used in the model (Figure 3.5), we suggest here that another mechanism may be at least partly responsible for the discrepancy in onset delay between the model results and observations. The number of particles at the edge of the northern bounce loss cone at the longitudes of the HAIL array is known to be substantially less than at the edge of the southern loss cone [*Inan et al.*, 1988b, Fig. 3]. Further, the wave-induced scattering involves small changes in pitch angle in comparison with the difference between the northern and southern loss cone angles [*Bortnik et al.*, 2002]. Hence, the majority of the particles which are pitch-angle scattered during the first equatorial crossing of the whistler wave may be scattered into the southern bounce loss cone, but not quite make it into the northern loss cone. These particles may thus not precipitate into the northern hemisphere directly. Instead, these particles would first mirror in the northern hemisphere and subsequently travel to the southern hemisphere where they would penetrate to lower mirror altitudes therein, colliding with atmospheric constituents [*Inan et al.*, 1988b]. Since the particles nevertheless arrive at the southern hemisphere at grazing pitch angles (i.e., they have been barely moved into the southern loss cone) a significant fraction of these particles would in fact undergo "backscaterring" upon collision in the southern atmosphere [*Lehtinen*, 2000, p.90]. The particles' pitch angle distribution would be broadened as a result of the backscattering interaction with the atmosphere.

The particles would then return to the northern hemisphere, now having a more isotropic (i.e., broadened) pitch angle distribution. This more isotropic pitch angle distribution would include a substantial number of particles within the northern loss cone, and the majority of these particles would then deposit their energy into the northern hemisphere atmosphere [*Inan et al.*, 1988b].

Compared to direct precipitation, these particles would undergo one full extra bounce period prior to precipitating, and so the onset delay between the lightning flash and the onset of the precipitation would be increased by $\sim$0.4 seconds, consistent with the observations. For whistlers originating from northern hemisphere lightning, this mechanism would also result in shorter onset delays in the southern hemisphere than in the northern hemisphere, consistent with past observations [*Burgess and Inan*, 1990, Fig. 5]. This mechanism would also result in substantially more precipitation in the southern than northern hemispheres, also consistent with past observations [*Inan et al.*, 1988b].

Figures 4.6 and 4.7 show the observed and modeled amplitude and phase perturbations of the VLF signal paths as a function of the distance from the lightning source for both cases. The distance is measured from the flash location to the point of crossing of the GCP and the geomagnetic longitude of the causative flash, the same coordinate used in Chapter 2. For the amplitude data for Case 1, the displacement of the peak perturbation from the causative flash is $\sim$6° for both the model and observation. The magnitude of the peak amplitude perturbation for the model and observation is within 25%. For Case 2, the displacement of the peak perturbation from the causative flash is $\sim$5° for the simulation, $\sim$4° for the HAIL observation. The magnitude of the peak perturbation is within a factor of three for Case 2, indicating that trapped flux levels may have increased during the second case. *Clilverd et al.* [2002] states that nonducted whistler-induced precipitation would occur with a 5°–10° latitudinal gap between the lightning and the equatorward edge of the patch, inconsistent with the LEP events observed here. For the two cases examined here, this gap is far less (2°–4°) in both the model results and observations, and is dependent on the cold plasmaspheric density profile (Section 3.3.1). The model calculates a perturbation region wider in latitudinal extent than what are observed for both
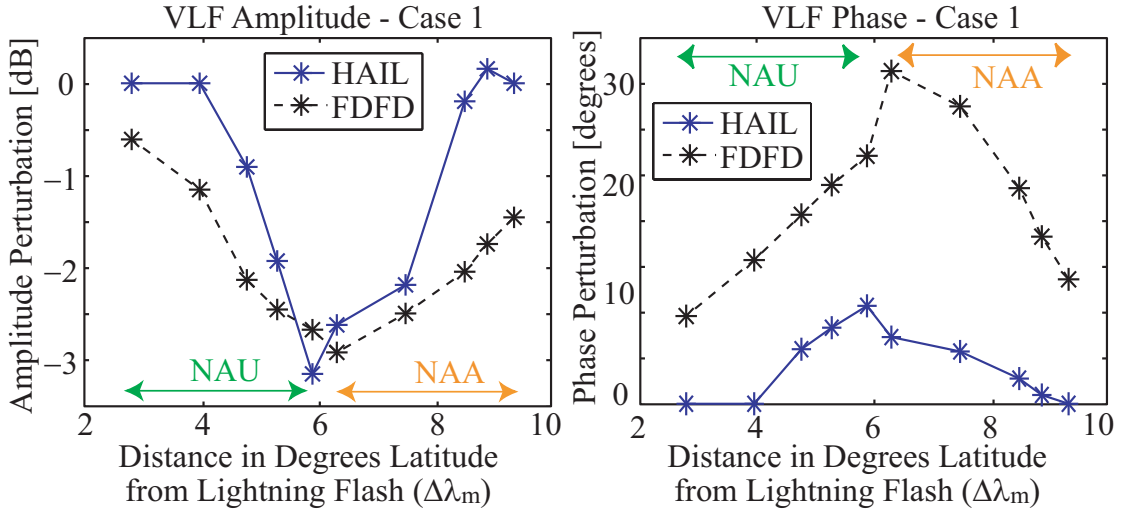
Figure 4.6: Case 1 VLF signal perturbations versus latitude. Observed (HAIL) and modeled (FDFD) amplitude and phase perturbations of the VLF signal paths as a function of the distance from the lightning source at $t=2$ seconds after the causative flash for Case 1. Each asterisk denotes a separate VLF signal amplitude perturbation. The distance is measured from the flash location to the point of crossing of the GCP and the geomagnetic longitude of the causative flash.

Cases 1 and 2, the most likely reason being that the model assumes a slower falloff in the lightning-generated whistler wave energy with distance (see Section 3.3) than what is actually generated by the lightning flashes in these cases.

Given the variability in the trapped energetic flux (Section 3.3.1), differences between the model and observation are expected. In fact, our main objective is not to compare and contrast the model calculations (for assumed trapped particle flux levels) with the HAIL VLF signal observations, but is rather to develop metrics with which we can characterize the VLF signal perturbations in terms of the associated precipitation flux. In other words, it goes without saying that the trapped flux levels near the loss cone edge for any given case would not be known except in an average sense, and the knowledge of this quantity is not important for our purpose since precipitation flux is linearly proportional to trapped flux. The fact that the magnitude of the peak amplitude perturbations is within 25% of that observed on HAIL simply indicates that the trapped flux levels determined on the basis of the AE8 model and
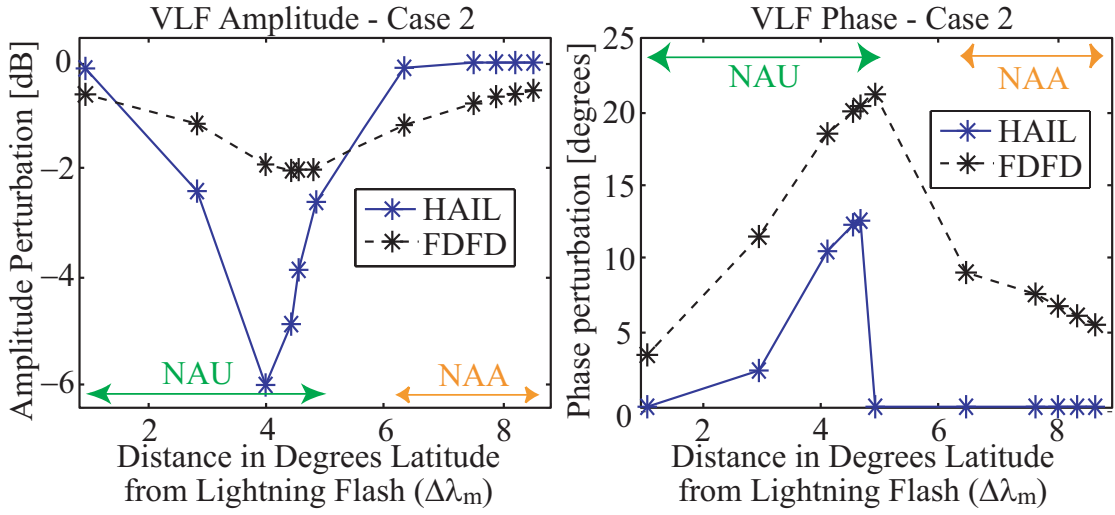
Figure 4.7: Case 2 VLF signal perturbations versus latitude. Observed (HAIL) and modeled (FDFD) amplitude and phase perturbations of the VLF signal paths as a function of the distance from the lightning source at $t=2$ seconds for Case 2.

the POES measurements may have been reasonably representative for these cases.

The model calculates positive phase perturbations, consistent with past work [*Wolf and Inan*, 1990] and the VLF signal perturbations detected on HAIL (Figures 4.6 and 4.7). However, the model calculates phase perturbations consistently larger than those observed. The FDFD model calculates a ratio of ∼0.1 [dB/deg] for amplitude and phase perturbations, smaller than that observed for the two cases by a factor of ∼2 to 3. *Inan and Carpenter* [1987, Eqn. 5] theoretically estimated the ratio between amplitude and phase perturbations for a single mode VLF signal to be 0.048 [dB/deg], independent of the perturbation extent and intensity, even smaller than that calculated by the FDFD model.

Starting at 08:00 UT on 24 March 2001 (an hour after Case 1), phase perturbations on the scale calculated by the model are detected on the HAIL array that are associated with the same thunderstorm as Case 1. The amplitude signatures are similar to those of Case 1, so that the amplitude/phase ratio varied with time. The phase signatures of LEP events in HAIL data are generally less consistent (from event to event and from night to night) than the amplitude signatures, and are known to change over the course of a night. *Wolf and Inan* [1990] examined VLF signatures of

LEP events, and found only a weak correlation between amplitude and phase perturbations that is highly dependent on the path examined. It should also be noted that the VLF signal phase measured by HAIL is relatively noisy in comparison with the VLF signal amplitude, in part due to the fact that the MSK demodulation algorithm used in 2001 was a preliminary one. A more robust algorithm is currently in use at the HAIL VLF sites, providing substantially better signal-to-noise ratio for phase data. Given this fact, and knowing that the phase response varies considerably over time and for different paths, the VLF amplitude signatures recorded on HAIL for the two cases examined here give a more reliable measure of the ionospheric disturbance. With the recent installation of new hardware and software at the HAIL sites, the usability of the phase data for quantitative analysis is now much improved.

## 4.5   Summary and Conclusions

In this chapter, we apply the modeling framework developed in Chapter 3 to two representative LEP events. The VLF amplitude and phase perturbations calculated by the model are compared directly to the VLF signal observations made on HAIL. In both of the two cases studied, the model calculates peak VLF amplitude and phase perturbations within a factor of three of those observed, well within the expected variability of radiation belt flux levels at the edge of the loss cone. The model calculates a peak in the precipitation that is poleward displaced $\sim 6°$ from the causative lightning flash, consistent with observations. The modeled precipitated energy flux ($E > 45$ keV) peaks at $\sim 1 \times 10^{-2}$ [ergs s$^{-1}$ cm$^{-2}$]. The model calculates shorter onset delays (by $\sim 0.5$ seconds) than those observed, and it is suggested that this difference may indicate that the observed precipitation onsets may be due to electrons that have once backscattered and/or mirrored in the southern hemisphere. The model calculates an increasing onset delay with latitude, consistent with observations. The model calculates a perturbation region wider in latitudinal extent than what are observed for both Cases 1 and 2, the most likely reason being that the model assumes a slower falloff in the lightning-generated whistler wave energy with distance (see Section 3.3) than what is actually generated by the lightning flashes in these cases.

Recognizing that the precipitation is highly dependent on trapped radiation belt flux levels (that are known to be highly variable), our objective in the next chapter is to develop metrics with which we can quantitatively relate the precipitation flux and ionospheric disturbance to measured VLF signal perturbations, independent of the trapped flux levels.

# Chapter 5

# Quantifying LEP via VLF Remote Sensing

## 5.1 Introduction

In the previous chapter, the modeling framework developed in Chapter 3 is applied to two representative LEP events. The VLF amplitude and phase perturbations calculated by the model are compared directly to the VLF signal observations made on HAIL.

In this chapter, we develop metrics with which we quantitatively relate the precipitation flux to measured VLF signal perturbations, independent of the trapped flux levels. We thus develop a methodology by which we estimate the total precipitation induced by a single lightning flash, independent of trapped radiation belt flux levels and using only the developed metrics and observations of VLF signal perturbations.

## 5.2 Metrics to Quantify LEP Events

To quantitatively relate VLF signal perturbations to electron precipitation, several metrics are used to quantify the precipitation and ionospheric disturbance. Through a comparison of the metrics with the VLF perturbations calculated by the FDFD model, quantitative relationships between VLF signal perturbations and the precipitation are
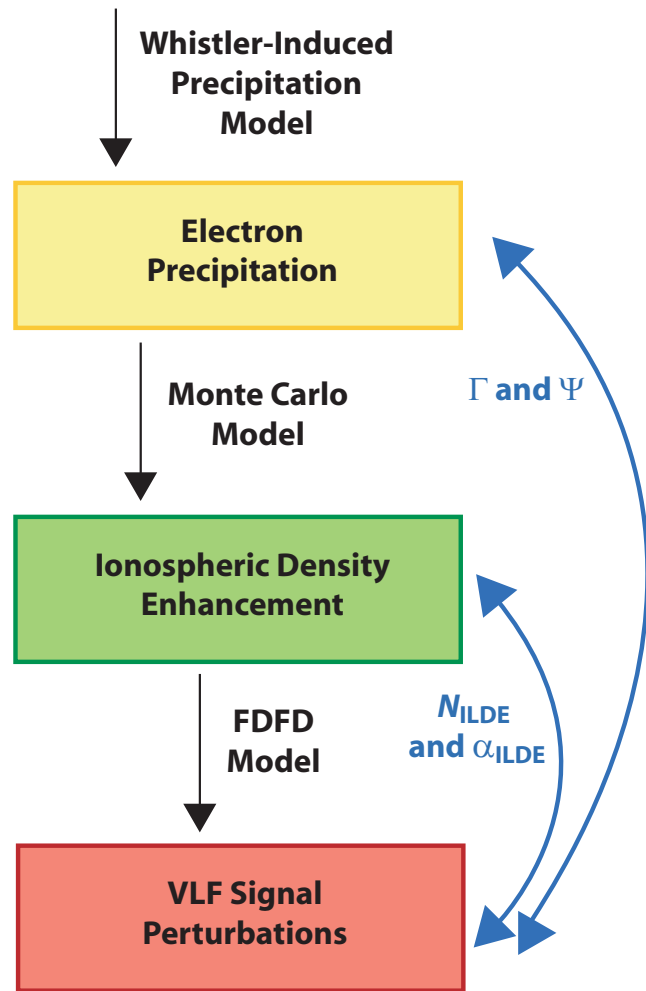
Figure 5.1: Block diagram showing the framework of the LEP model and the relationships of the metrics and conversion ratios to the framework.
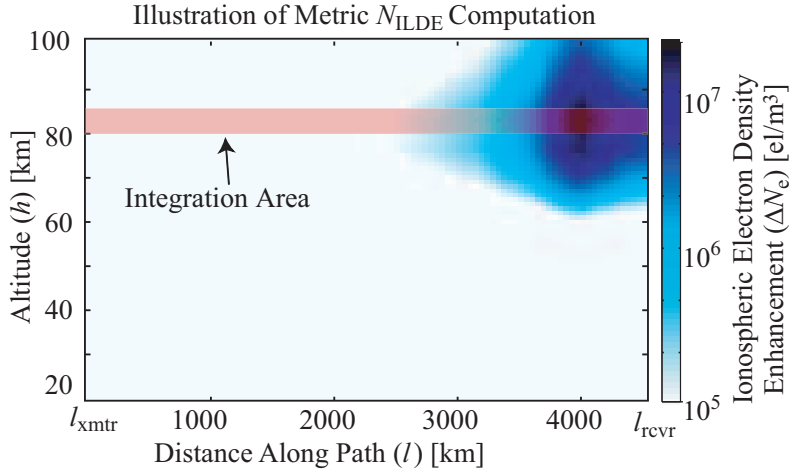
Figure 5.2: Illustration of the Integrated Line Density Enhancement ($N_{\mathrm{ILDE}}$) metric, as described in the text. The ionospheric electron density enhancement ($\Delta N_e$) is shown as a function of altitude and distance along the path for a representative VLF signal path. The pink shaded box denotes the integration area from 80 to 85 km and over the path length.

estimated. A block diagram of the model framework is repeated in Figure 5.1. Also shown are the relationships of the metrics and conversion ratios (which we define later in the chapter) to the model framework.

## 5.2.1 Integrated Line Density Enhancement (ILDE)

The Integrated Line Density Enhancement (ILDE) metric gives a measure of the ionospheric density enhancement along a given VLF signal GCP. It is defined as the ionospheric electron density enhancement produced by the energy deposition from the LEP event, integrated from 80 to 85 km in height and over the entire path length:

$$N_{\mathrm{ILDE}} = \int_{80\,\mathrm{km}}^{85\,\mathrm{km}} \int_{l_{\mathrm{xmtr}}}^{l_{\mathrm{rcvr}}} \Delta N_e(l, h)\, \mathrm{d}l\, \mathrm{d}h \tag{5.1}$$

where $l$ is the distance along the path, $h$ is altitude, and $\Delta N_e$ is the electron enhancement obtained from the Monte Carlo simulation. $N_{\mathrm{ILDE}}$ has units of secondary electrons produced per meter perpendicular to the path.

Figure 5.2 illustrates the calculation of $N_{\mathrm{ILDE}}$ for a given VLF signal path. The

ionospheric electron density enhancement ($\Delta N_e$) is calculated using the Monte Carlo model (Section 3.3.2) as a function of distance along the VLF signal path. The density enhancement is then integrated from 80 to 85 km in altitude and along the entire VLF path length to obtain $N_{\mathrm{ILDE}}$. As $\Delta N_e$ is obtained directly from the output of the Monte Carlo model of ionospheric density enhancement, $N_{\mathrm{ILDE}}$ provides an estimate of the expected VLF signal perturbation without having to use the FDFD model of VLF signal propagation.

The validity of the ILDE metric is illustrated in Figures 5.3a and b, where $N_{\mathrm{ILDE}}$ is compared to the VLF signal perturbations calculated by the FDFD model as a function of distance from the lightning flash. As stated in Section 4.4, differences between the FDFD model results and the VLF signal perturbations observed are expected due to the large variability in trapped energetic electron flux levels near the loss cone edge. We therefore compare $N_{\mathrm{ILDE}}$ directly to the VLF signal perturbations calculated by the model, assuming that the FDFD model calculations and the observations made on HAIL would agree if the inputs into the whistler-induced precipitation model were accurately known. The strong (r>0.9) correlation indicates that $N_{\mathrm{ILDE}}$ does indeed give a reliable indication of the VLF signal perturbations expected.

The strong correlation between the VLF signal perturbations calculated by the FDFD model and $N_{\mathrm{ILDE}}$ indicate that observations of VLF signal perturbations made on HAIL can be used to estimate the associated ionospheric density enhancement. To convert between the VLF amplitude perturbations observed on HAIL and the density enhancement along a given path, a conversion ratio $\alpha_{\mathrm{ILDE}}$ of $4.7\pm2.0\times10^{16}$ [el m$^{-1}$/dB] is estimated for enhancement events of similar location and characteristics to the cases examined in this work, where $\alpha_{\mathrm{ILDE}} = N_{\mathrm{ILDE}}/\Delta A$. The use of phase measurements to estimate the density enhancement is less reliable (Section 4.4), and a conversion ratio $\beta_{\mathrm{ILDE}}$ of $4\pm2\times10^{15}$ [el m$^{-1}$/degree] should be used with caution, where $\beta_{\mathrm{ILDE}} = N_{\mathrm{ILDE}}/\Delta\phi$. Using these conversion ratios, VLF remote sensing can be used to infer the ionospheric density enhancement associated with precipitation events, independent of the variable trapped electron flux levels. These conversion ratios are suggested for precipitation events of similar location and characteristics, and for similar VLF path configurations, to the cases examined in this work. Application
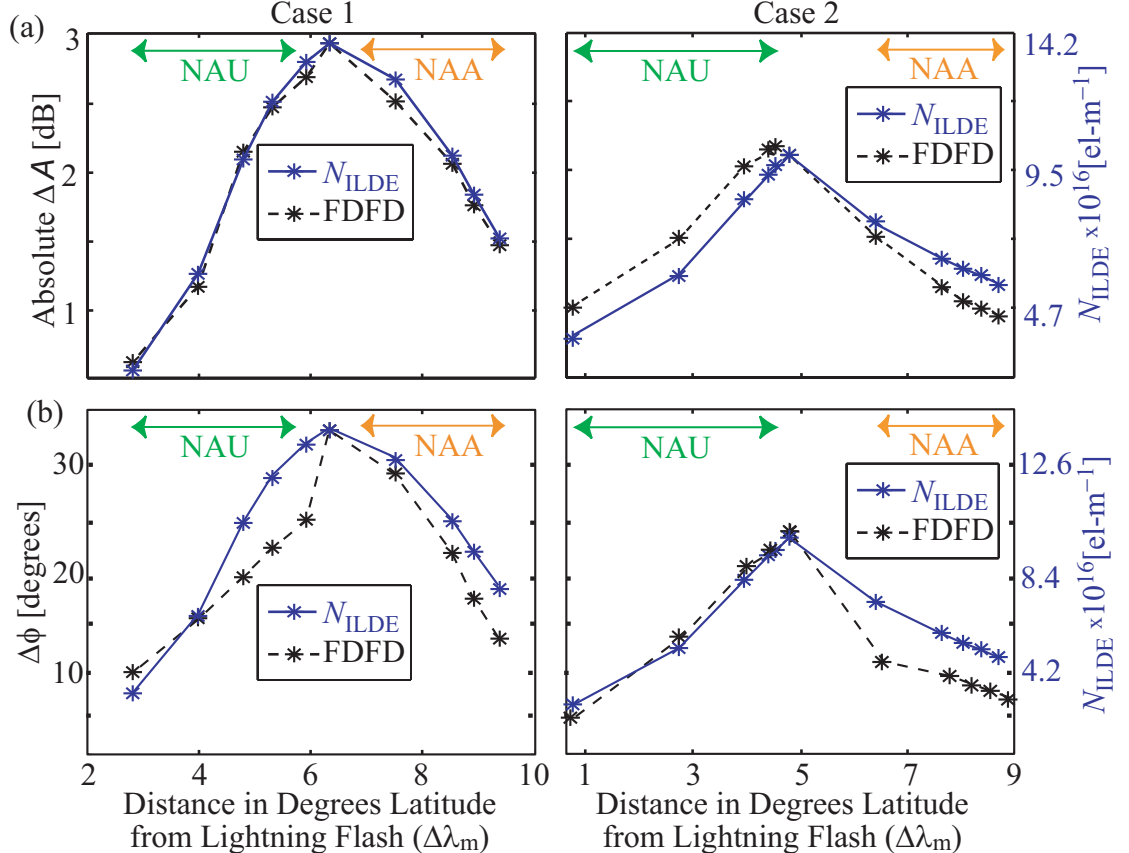
Figure 5.3: Ionospheric disturbance metric $N_{ILDE}$. (a) $N_{ILDE}$ as a function of distance from the lightning source for both cases, with the scale shown on the right. Also shown is the VLF signal amplitude perturbation calculated by the FDFD model, with the scale shown to the left. (b) $N_{ILDE}$ versus distance from the lightning source for both cases, compared to the VLF signal phase perturbation calculated by the model.

of this methodology to other types of precipitation events (and other VLF signal paths) should refine these conversion ratios to be applicable in other regions and on other VLF paths.

## 5.2.2 Electron Precipitation Metric ($\Gamma$)

In order to quantitatively relate VLF signal perturbations directly to the energetic electron precipitation, we define a time-integrated precipitation metric $\Gamma$ as follows:

$$\Gamma = \int_{l_{\mathrm{xmtr}}}^{l_{\mathrm{rcvr}}} \int_{0\,\mathrm{s}}^{5\,\mathrm{s}} \int_{100\,\mathrm{keV}}^{300\,\mathrm{keV}} \Phi(E, t, l)\, \mathrm{d}E\, \mathrm{d}t\, \mathrm{d}l \tag{5.2}$$

where $E$ is electron energy, $t$ is time of precipitation, and $\Phi$ is the precipitated differential number flux obtained from the whistler-induced precipitation model (Section 4.2). The $\Gamma$ metric has units of electrons precipitated per meter perpendicular to the path.

Figure 5.4 illustrates the calculation of $\Gamma$ for a given VLF signal path. The precipitated differential number flux ($\Phi$) at each point along the path is calculated using the whistler-induced precipitation model (Section 3.3.1). Shown is the differential number flux at a representative location along the GCP, repeated from Figure 4.1a. The flux is then integrated from 0 to 5 seconds in time and 100 to 300 keV in energy to give the precipitation at a specific location along the path. This process is repeated at each location along the path (sampled every ∼30 km), and integrated over the entire path length to obtain $\Gamma$. As $\Phi$ is obtained directly from the output of the whistler-induced precipitation model, $\Gamma$ provides an estimate of the expected VLF signal perturbation *without* having to use either the FDFD model of VLF signal propagation or the Monte Carlo model of ionospheric density enhancement.

In Figures 5.5a and b, $\Gamma$ is compared to the VLF signal perturbations calculated by the FDFD model, as a function of distance from the lightning source. There is good agreement for both the NAA and NAU transmitter paths. This agreement is shown more clearly in Figure 5.6, a scatter plot of all the VLF signal perturbations calculated by the model as a function of $\Gamma$. The scatter plot includes all of the VLF signal paths over a range of times ($0<t<5$ s) and for both cases. The strong
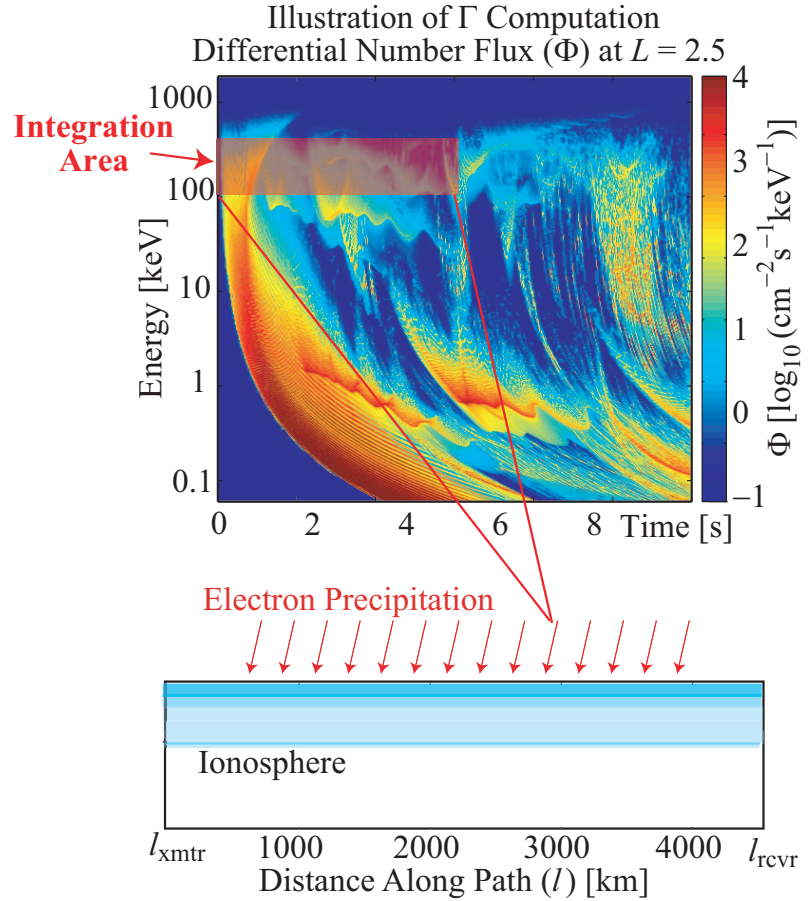
Figure 5.4: Illustration of the precipitation metric $\Gamma$, with the top panel showing the precipitated differential number flux ($\Phi$) at a representative location along a given signal path, repeated from Figure 4.1a. The boxed region denotes the integration area from 0 to 5 seconds and 100 to 300 keV in energy. The resulting precipitation is for a given location along the path, as represented in the lower panel. The precipitation at each point along the path is calculated in a similar manner, and integrated over the entire path length.
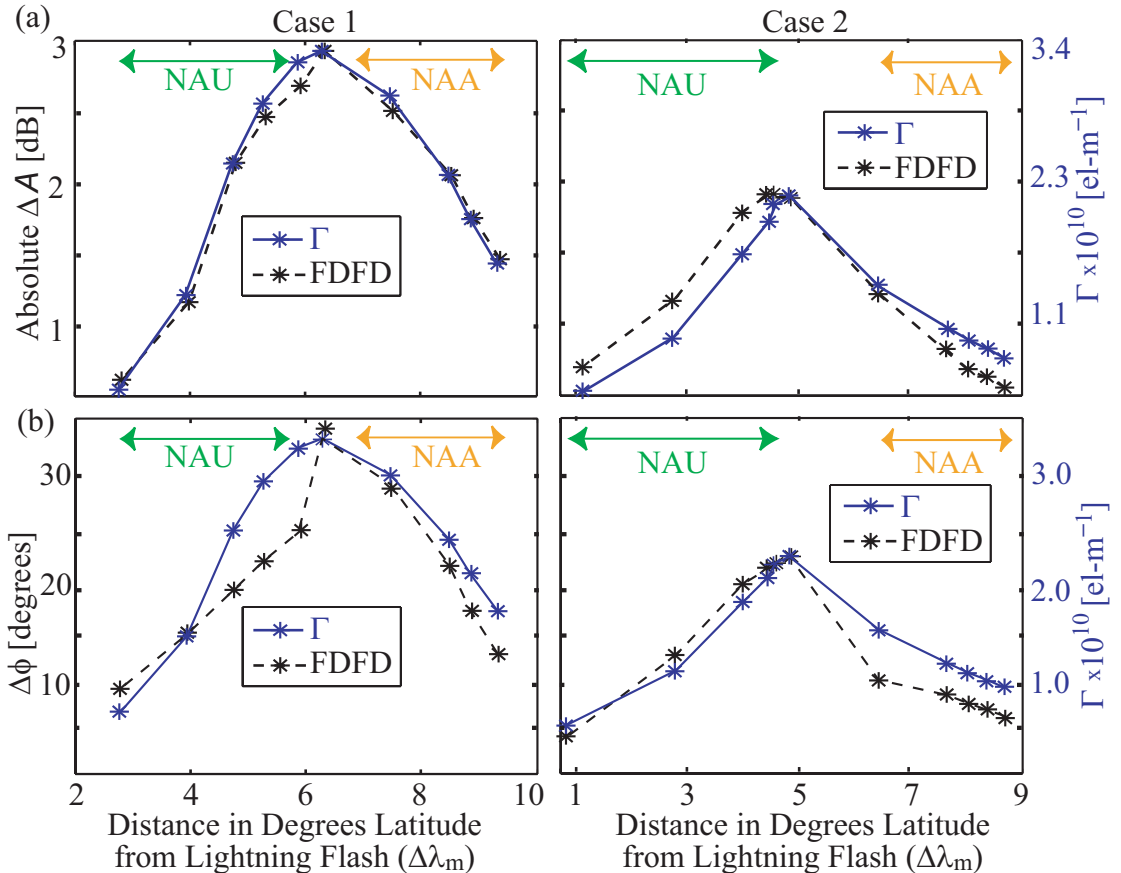
Figure 5.5: (a) Precipitation metric $\Gamma$ (right axis) versus the modeled amplitude perturbation (left axis) as function of distance from the lightning flash for both cases. (b) $\Gamma$ compared to the modeled phase perturbation for both cases.

(r>0.9) correlation indicates that $\Gamma$ provides a reliable indication of the VLF signal perturbations expected, and that observations of VLF signal perturbations made on HAIL can be used to estimate the associated electron precipitation along a given GCP. A conversion ratio $\Psi$ of $1.1\pm0.4\times10^{10}$ [el m$^{-1}$/dB] is estimated for precipitation events of similar location and characteristics (and similar VLF path configurations) to the cases examined in this work, with $\Psi = \Gamma/\Delta A$. The conversion ratio $\Psi$ is equal to the slope of the black line shown in the top panel of Figure 5.6. The use of phase measurements to estimate precipitation is less reliable, and a conversion ratio $\Lambda$ of $1.0\pm0.5\times10^{9}$ [el m$^{-1}$/degree] should be used with caution, with $\Lambda = \Gamma/\Delta\phi$.

It should be noted that the conversion ratios ($\alpha_{\text{ILDE}}$ and $\Psi$) establish a linear relationship between our metrics ($N_{\text{ILDE}}$ and $\Gamma$) and a logarithmic quantity, the VLF signal amplitude perturbation measured in decibels. However, given the small range of amplitude perturbations examined in this work and typically associated with LEP events, the amplitude perturbation measured in dB behaves in a nearly linear fashion, and hence we can establish a linear relationship between our metrics and the amplitude perturbations measured in dB. Using these ratios, VLF remote sensing can be used to quantitatively estimate the precipitation associated with LEP events, independent of the variable trapped electron flux levels, as demonstrated in the next section.

## 5.3 Estimating Precipitation from VLF Data

Figure 5.1 shows a block diagram illustrating the relationship of the metrics and associated conversion ratios to the model framework. Developed with respect to the LEP model, the conversion ratios allow us to use VLF signal perturbations observed on HAIL to infer the electron precipitation and ionospheric disturbance associated with a given lightning flash. We now demonstrate the use of these metrics for the Case 1 lightning flash.

Using $\Psi$, VLF data can be used to quantitatively estimate the total precipitation loss associated with a LEP event. Assuming the HAIL paths are oriented in the east-west direction, so that integrating across the paths is equivalent to an integral over
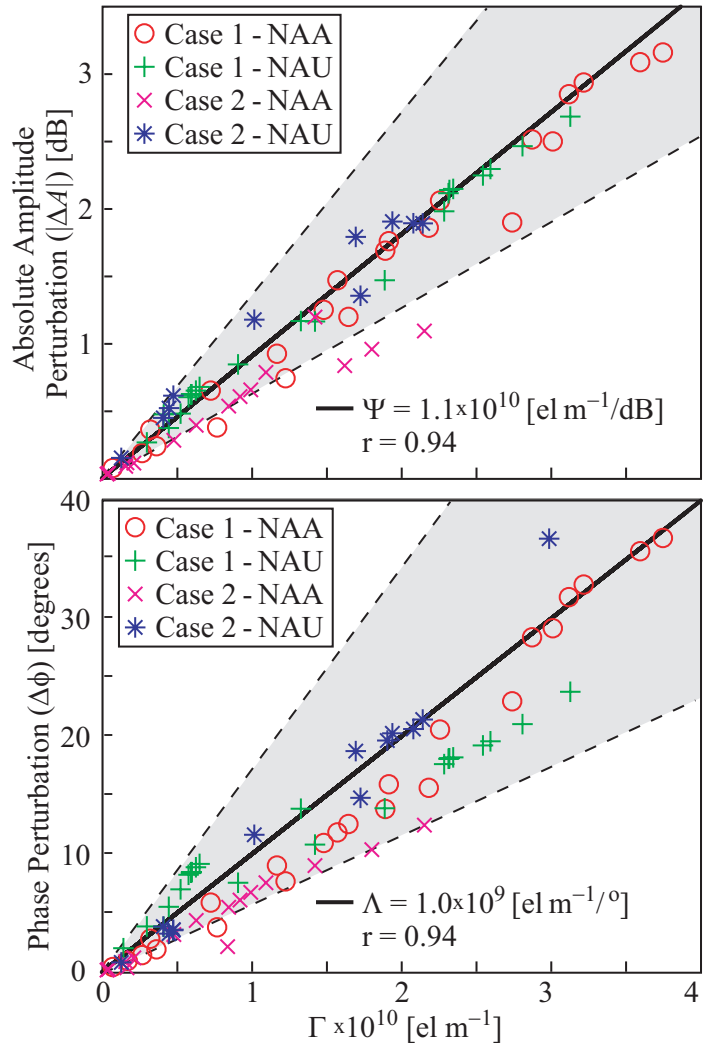
Figure 5.6: Scatter plot of $\Gamma$ and VLF signal perturbations. (Top) A scatter plot of the VLF amplitude perturbations calculated by the FDFD model as a function of $\Gamma$. Each point represents a particular VLF signal path at a particular time, with the case and transmitter signal denoted by different symbols. The slope of the solid black line equals the conversion ratio $\Psi = 1.1 \pm 0.4 \times 10^{10}$ [el m$^{-1}$/dB]. The shaded region denotes the uncertainty range. The amplitude perturbations are strongly correlated (r>0.9) with $\Gamma$ for both cases, both transmitters, and over a range of precipitation intensities. (Bottom) A scatter plot of the VLF phase perturbations calculated by the FDFD model as a function of $\Gamma$. The fitted line has a slope equal to the conversion ratio $\Lambda$ of $1.0 \pm 0.5 \times 10^9$ [el m$^{-1}$/degree], with the shaded region denoting the uncertainty range.

latitude, the total number of electrons precipitated (100–300 keV) for a LEP event
($\Upsilon$) is estimated as follows:

$$\Upsilon \simeq (1.1 \times 10^5) \times \Psi \times \int_{\lambda_0}^{\lambda_1} |\Delta A(\lambda)| \, \mathrm{d}\lambda \qquad (5.3)$$

where $\Delta A$ is the amplitude perturbation (in dB), $\Psi$ is the conversion ratio previously
obtained and equals $1.1\pm0.4\times10^{10}$ [el m$^{-1}$/dB], the factor $1.1\times10^5$ is used to convert
from degrees latitude to meters, and $\lambda$ is the latitudinal distance from the lightning
flash to the GCP. As illustrated in Figure 5.7, integrating the HAIL VLF signal per-
turbations for Case 1 (Figure 4.6) over latitude gives a perturbation area of $1.46\times10^6$
[dB-m]. Multiplying the perturbation area by $\Psi$ gives a total electron precipita-
tion (100-300 keV) induced by the LEP event of $1.6\pm0.3\times10^{16}$ electrons. Similarly,
a perturbation area of $9.8\times10^5$ [dB-m] for Case 2 gives a total loss of $9.8\pm2.0\times10^{15}$
electrons (100-300 keV). This estimate of precipitation loss is calculated directly from
the VLF signal perturbations observed on HAIL, using only the conversion ratio $\Psi$.

It should be noted that here we count as precipitation all particles scattered into
the bounce loss cone (as defined in $\Gamma$ and $\Psi$). For example, if only 10% of the particles
scattered into the northern bounce loss cone actually deposit their energy into the
atmosphere (with the remaining 90% mirroring and/or backscattering instead), the
actual number of electrons precipitated into the northern hemisphere atmosphere that
resulted in a given observed VLF signal perturbation is actually a factor of 10 less than
that estimated by the conversion ratio $\Psi$. Therefore, the conversion ratio $\Psi$ should
be considered an upper bound when used in estimating precipitation, and it should
be kept in consideration that the ratio is used to estimate the number of particles
scattered into the bounce loss cone. As the relative roles of direct versus backscattered
precipitation are more clearly understood, together with a clearer understanding of
the evolution of the pitch angle distribution of scattered particles within the loss cone
over time, the choice of how to define $\Gamma$ and $\Psi$ will become clearer.

Following this methodology, subionospheric VLF data can provide a quantitative
measure of the loss of energetic electrons into the atmosphere. This estimate fur-
thermore is independent of the trapped pitch angle distribution and flux levels in the
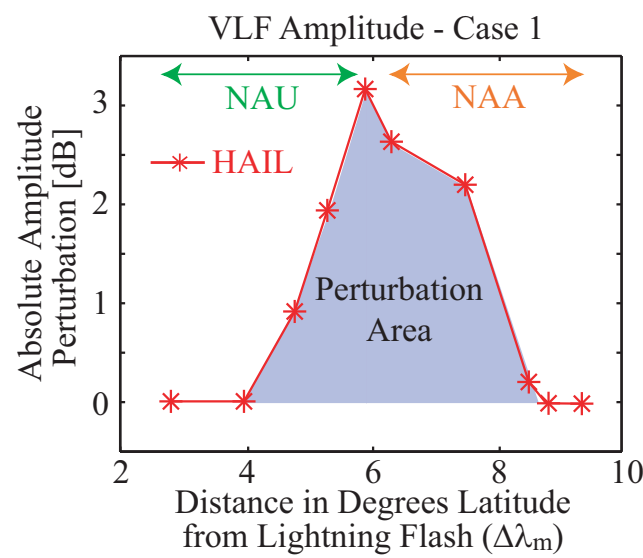
Figure 5.7: HAIL observations of the absolute amplitude perturbation as a function of latitudinal distance from the lightning flash for Case 1, repeated from Figure 4.6. The shaded area represents the perturbation area, integrated over latitude, used to estimate the total precipitation ($\Upsilon$) induced by the Case 1 lightning flash (100-300 keV).

radiation belt. It should be noted that the metrics presented are for nonducted LEP events detected by the HAIL array. Similar analysis to that presented here, applied to other precipitation events and other VLF paths, should broaden the use of VLF remote sensing to quantitatively measure precipitation on a global scale. This methodology is fully applicable to other types of precipitation events and other VLF signal path configurations, the values of the conversion ratios (i.e., $\Psi$ and $\alpha_{\mathrm{ILDE}}$) simply need to be recalculated for the particular case considered. A similar methodology has already been applied to subionospheric VLF signatures of VLF transmitter-induced precipitation [*Inan et al.*, 2007], and further refinements of the conversion factors $\Psi$ and $\Lambda$ should encourage the use of VLF remote sensing to quantitatively measure precipitation events.

## 5.4 Radiation Belt Loss

Based on the low-altitude S81-1 (SEEP) satellite measurement of LEP events, *Voss et al.* [1998] calculated that $\sim$0.0015% of $E>$45 keV electrons in a single flux tube at $L$=2.15 were precipitated in a single LEP event. The precipitation was assumed to be due to ducted whistlers, although no independent evidence existed for the ducted nature of the interaction. Using Equation 5 of *Voss et al.* [1998], we calculate the percentage loss from a single flux tube at the geomagnetic longitude of the lightning flash, for a range of $L$-shells (Figure 5.8). The percentage loss is based on the precipitation calculated by the whistler-induced precipitation model (Section 3.3.1), and is dependent on the initial pitch angle distribution input into the model. The loss includes all particles scattered into the northern and southern bounce loss cones. As we do not have VLF signal perturbation measurements in the conjugate location in the southern hemisphere for the two cases examined, we can only verify the precipitation in the northern hemisphere. Again, we define precipitation loss here as all particles scattered into the bounce loss cone, while not all of these particles may in fact deposit their energy into the atmosphere (i.e., some particles may instead mirror and/or backscatter). Hence the loss estimates given here should be considered an upper bound.
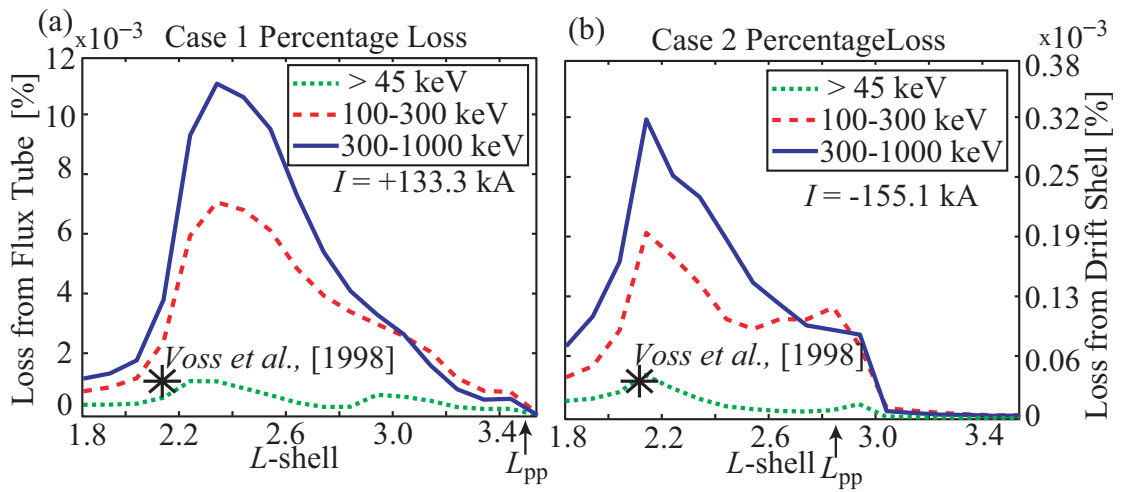
Figure 5.8: Radiation Belt Loss. (a) Percentage of electrons lost into the bounce loss cone from a single flux tube at the geomagnetic longitude of the lightning flash, as a function of *L*-shell, for three energy ranges and Case 1. The scale on the right shows the percentage loss (integrated over longitude) from the drift shell (calculated over the entire drift orbit, assuming an azimuthally independent trapped flux). This value represents the percentage of all available trapped particles, as a function of *L*-shell, lost by a single lightning flash. (b) Percentage of electrons lost for Case 2. Also shown is the peak current of the lightning flash (*I*) for both cases. The asterisks show the calculation of precipitation loss from *Voss et al.* [1998].

For Case 1, the percentage loss from a single flux tube (for 100-300 keV) peaks at ∼0.007% at $L$∼2.35. For Case 2, the percentage loss peaks at ∼0.006% at $L$∼2.2. Notice the secondary peak at $L$∼2.8 in Case 2, due to the guiding of whistler wave energy near the plasmapause [*Inan and Bell*, 1977]. To compare with *Voss et al.* [1998], the percentage loss for $E$>45 keV is also shown. For Case 1, the percentage loss peaks at ∼0.001% at $L$∼2.3. For Case 2, the loss peaks at ∼0.0015% at $L$∼2.15. The excellent agreement between the model and *Voss et al.* [1998] adds credence to the accuracy of the model and our metrics, at least for the $L$-shell range and the VLF path distribution of the HAIL array. Also shown (right axis) is the percentage of total flux lost (integrated over longitude) from the drift shell (calculated over the entire drift shell). The loss as a function of longitude is simply a scaling function times the peak loss (Section 3.3), and hence the loss at each $L$-shell integrated over longitude is simply a constant times the peak loss at the longitude of the lightning flash. Since we are assuming no azimuthal variations in trapped flux, the trapped flux integrated over longitude is also a constant for each $L$-shell. Therefore the percentage drift shell loss is simply the percentage loss from a single flux tube at the lightning longitude times a scaling factor (∼0.0319).

## 5.5    Summary and Conclusions

In this chapter, we introduce two metrics ($N_{\mathrm{ILDE}}$ and $\Gamma$) that provide an excellent indication of the precipitation flux and ionospheric disturbance represented by VLF signal perturbations observed with the HAIL array. We also demonstrate a methodology by which we estimate the total precipitation induced by a single lightning flash, independent of trapped radiation belt flux levels and using only the developed conversion ratios and observations of VLF signal perturbations. For the Case 1 lightning flash, the peak loss is estimated at ∼0.001% from a single flux tube at $L$∼2.2, consistent with previous satellite measurements of LEP events [*Voss et al.*, 1998].

The robustness of these metrics for the case in hand is a result of several factors, including: (1) the ionospheric disturbance is smoothly varying throughout the region of interest; (2) the VLF signal at the location of the receivers is relatively stable

(Figure 3.9d); (3) the energy spectra of the precipitation does not vary dramatically with time or location; and (4) the location of the precipitation along each VLF signal path is similar for all GCPs and for both cases. The correlation between the metrics and the VLF signal perturbations suggest the use of conversion ratios ($\alpha_{\text{ILDE}}$ and $\Psi$) to quantitatively relate VLF signal perturbations to the causative ionospheric disturbance and electron precipitation. These conversion ratios are suggested for precipitation events of similar location and characteristics to the cases examined in this work. Application of this methodology to other types of precipitation events (and other VLF signal paths) should refine these conversion ratios to be applicable in other regions and on other VLF paths. Our results demonstrate the usefulness of VLF remote sensing in accurately characterizing precipitation events and resulting ionospheric electron density enhancements.

# Chapter 6

# Summary

## 6.1   Summary

In this dissertation, we describe how VLF remote sensing can be used to quantitatively estimate the precipitation of energetic electrons into the atmosphere. In particular, we describe how observations of VLF signal perturbations made on the Holographic Array for Ionospheric/Lightning Research (HAIL) are used to quantitatively estimate the ionospheric density enhancement and energetic electron precipitation associated with lightning-induced electron precipitation (LEP) events.

Chapter 1 outlines the scope and aim of the dissertation, namely: (i) determination of the temporal and spatial characteristics of the VLF perturbations associated with lightning-induced electron precipitation (LEP) events; (ii) development of a framework to model the electron precipitation, ionospheric disturbance, and VLF signal perturbation associated with LEP events; and (iii) development of a methodology by which observations of VLF signal perturbations are used to quantitatively estimate the precipitation loss associated with a LEP event. We also describe the concept of VLF remote sensing and the detection of LEP events using the Holographic Array for Ionospheric/Lightning Research (HAIL). This chapter also provides the context of LEP events in terms of radiation belt research, and reviews previous related research.

In Chapter 2 we describe the use of HAIL to measure the temporal and spatial

characteristics of VLF signal perturbations associated with LEP events. We undertake a statistical examination of LEP events as detected by the HAIL array during March 2001. We examine in detail two nights of LEP event activity, 24 and 28 March 2001, determining the spatial and temporal characteristics of the VLF signal perturbations associated with the LEP events. We provide evidence that 90% of the precipitation occurs over a region $8°\pm1°$ and $9°\pm1°$ in latitudinal extent for the two time periods. The measured peak of the precipitation is poleward displaced ($6°45'\pm30'$ and $7°45'\pm30'$ for the two case studies) from the causative discharge. Analysis indicates that the onset delay and the duration of precipitation steadily increase with increasing *L*-value, while the signal recovery time is independent of *L*-value for the LEP events associated with both storms. We also discuss the variability in occurrence rates of LEP events, and argue that the precipitation induced by a given lightning flash is highly sensitive to the trapped radiation belt flux levels near the loss cone. This chapter deals exclusively with the VLF signal perturbations associated with LEP events, with no quantitative estimates of the electron precipitation and ionospheric disturbance associated with the VLF signal perturbations.

The remaining chapters of the dissertation deal with quantitatively relating the VLF signal perturbations to the causative ionospheric disturbance and electron precipitation. In Chapter 3, we provide the details of the framework used to model the lightning-induced electron precipitation, resulting ionospheric disturbance, and VLF signal perturbation, with the output of the modeling framework directly comparable to the observations made on HAIL. The model framework is made up of three major components: a model of whistler-induced electron precipitation [*Bortnik et al.*, 2006a]; a Monte Carlo simulation of the energy deposition into the ionosphere resulting from the calculated precipitation flux [*Lehtinen et al.*, 2001]; and a model of VLF subionospheric signal propagation that takes into account the disturbed ionospheric density profiles [*Chevalier and Inan*, 2006]. This modeling framework is the most comprehensive model to date in terms of quantitative interpretation of VLF signal perturbations associated with nonducted lightning-induced electron precipitation. In particular, we describe the setup of the modeling framework with respect to two representative lightning-induced electron precipitation events.

In Chapter 4, we apply the model framework to two representative LEP events. We present the calculated electron precipitation flux induced by the lightning-generated whistler waves, the ionospheric electron density enhancement resulting from this precipitation, and the VLF signal perturbations resulting from the ionospheric disturbance. We then directly compare the VLF amplitude and phase perturbations calculated by the model to the VLF signal observations made on HAIL. In both of the two cases examined, the model calculates peak VLF amplitude and phase perturbations within a factor of three of those observed, well within the expected variability of radiation belt flux levels. The model calculates a peak in the precipitation that is poleward displaced $\sim6°$ from the causative lightning flash, consistent with observations. The modeled precipitated energy flux ($E>45$ keV) peaks at $\sim1\times10^{-2}$ [ergs s$^{-1}$ cm$^{-2}$]. The model calculates shorter onset delays (by $\sim0.5$ seconds) than those observed, and it is suggested that this may indicate that the observed precipitation first backscatters in the southern hemisphere. The model calculates an increasing onset delay with latitude, consistent with observations. The model calculates a perturbation region wider in latitudinal extent than what are observed for both Cases 1 and 2, the most likely reason being that the model assumes a slower falloff in the lightning-generated whistler wave energy with distance (see Section 3.3) than what is actually generated by the lightning flashes in these cases.

Recognizing that the precipitation is highly dependent on trapped radiation belt flux levels (that are known to be highly variable), in Chapter 5 we develop metrics with which we quantitatively relate the precipitation flux and ionospheric disturbance to measured VLF signal perturbations, independent of the trapped flux levels. Through a comparison of VLF experimental observations of the two representative LEP events with the comprehensive model of lightning-induced electron precipitation and the resulting ionospheric disturbance, we examine the use of VLF remote sensing to quantitatively measure the precipitating flux and ionospheric density enhancement associated with two representative LEP events. In particular, we introduce two metrics ($N_{\mathrm{ILDE}}$ and $\Gamma$) that provide an excellent indication of the precipitation flux and ionospheric disturbance represented by VLF signal perturbations observed with the HAIL array. A conversion ratio $\Psi$, relating VLF signal amplitude perturbations to

the time-integrated precipitation (100-300 keV) along the VLF path, of $1.1\pm0.2\times10^{10}$ [el m$^{-1}$/dB] is suggested for precipitation events of similar location and characteristics to those examined.

We also demonstrate a methodology by which we can estimate the total precipitation induced by a single lightning flash, independent of trapped radiation belt flux levels and using only the developed conversion ratio $\Psi$ and observations of VLF signal perturbations. The total precipitated flux (100–300 keV) induced by the Case 1 LEP event is estimated at $1.6\pm0.3\times10^{16}$ electrons. The peak loss is estimated at $\sim0.001\%$ from a single flux tube at $L\sim2.2$, consistent with previous satellite measurements of LEP events [*Voss et al.*, 1998]. Our results demonstrate the usefulness of VLF remote sensing in accurately characterizing precipitation events and resulting ionospheric electron density enhancements.

## 6.2   Discussion

This dissertation deals exclusively with lightning-induced electron precipitation events occurring over the continental United States, as detected by the HAIL array. However, this dissertation also lays down the groundwork for the use of VLF remote sensing to quantitatively estimate radiation belt loss associated with other types of precipitation events across the globe. The two metrics ($N_{\mathrm{ILDE}}$ and $\Gamma$) that are introduced give an excellent indication of the ionospheric disturbance and electron precipitation represented by VLF signal perturbations observed with the HAIL array. The correlation between the metrics and the VLF signal perturbations suggest the use of conversion ratios ($\alpha_{\mathrm{ILDE}}$ and $\Psi$) to quantitatively relate VLF signal perturbations to the causative ionospheric disturbance and electron precipitation. These conversion ratios are suggested for precipitation events of similar location and characteristics to the cases examined in this work. Application of this methodology to other types of precipitation events (and other VLF signal paths) should refine these conversion ratios to be applicable in other regions and on other VLF paths.

In point of fact, the model framework and methodology for quantitatively relating VLF signal perturbations is currently being applied to a variety of other precipitation

events and locations. A similar methodology to that described in this thesis has been applied to transmitter-induced precipitation as detected by a VLF signal path from the NLK transmitter in Jim Creek, Washington to a VLF receiver located in Midway, Hawaii [*Inan et al.*, 2007]. The model framework has also been applied to polar regions, for a VLF signal path between the geomagnetic South Pole and Palmer Station, Antarctica [*Chevalier et al.*, 2007a]. The extension of this methodology to other types of precipitation and other regions of the globe should enable the use of VLF remote sensing as a measurement tool of precipitation loss from the radiation belts.

*Abel and Thorne* [1998a,b] theoretically estimated the loss rates of radiation belt electrons from 100-1500 keV due to Coulomb collisions and resonant interactions with plasma waves, including plasmaspheric hiss, lightning generated whistlers and VLF transmitters. Due to their relative ease of installation and continuous time coverage, the use of ground-based VLF receivers to quantitatively measure precipitation events can provide an excellent experimental verification of the theoretical works of *Abel and Thorne* [1998a,b] and *Bortnik et al.* [2003a].

# 6.3   Suggestions for Future Work

This dissertation serves as a first step toward the use of VLF remote sensing to quantitatively estimate the electron precipitation and ionospheric disturbance associated with LEP events. However, future work will hopefully continue along this vein in terms of using VLF to make quantitative measurements that are independent of magnetospheric conditions. The establishment of such a methodology should make VLF remote sensing a viable quantitative technique for use in estimating radiation belt loss (especially in the 100-300 keV range).

### 6.3.1   Improvements to the Model Framework

**Whistler-Induced Precipitation Model**

In this dissertation, we have used the model setup detailed in *Bortnik* [2004], with only slight modifications as detailed in Section 3.3.1. A refinement of some of the inputs into the model should increase the accuracy of the calculated precipitation.

The first input that could be modified is the lightning-generated whistler wave energy that is input into the ray tracer model. To improve the accuracy of the input whistler wave energy, the lightning flash and resulting whistler wave energy generation could be simulated using the same Finite Difference, fully electromagnetic model [*Chevalier et al.*, 2007b] that is used in this dissertation to model VLF signal propagation. Using either a full three dimensional treatment or a two dimensional approximation, the lightning flash would be modeled as a current source based on NLDN data and/or VLF broadband recordings of the associated lightning spheric. The energy spectra, temporal and spatial characteristics of the illumination region, and the wave normal angles of the whistler wave energy generated by the lightning flash would be calculated at the point of injection (i.e., 1000 km altitude) into the VLF ray tracer model. This calculation could also be done during the daytime and for intracloud (rather than cloud-to-ground) lightning flashes. These calculations can be directly compared to low-altitude satellite observations of lightning-generated whistlers (i.e., DEMETER). The whistler wave energy input into the precipitation model would be based on these calculations, increasing the accuracy of the whistler-induced precipitation model. As an example of how this would likely improve the model, the extent of the precipitation calculated by the model in this dissertation (Figures 4.6 and 4.7) is larger than that observed, suggesting that the model assumes a slower falloff in the lightning-generated whistler wave energy with distance (see Section 3.3) than what is actually generated by the lightning flashes in these cases.

The second set of inputs that could be modified is those used in the VLF ray tracing model, namely the Earth's magnetic field and cold plasmaspheric density. The Earth's magnetic field model used in this dissertation is a simple tilted dipole model, and a more current model [i.e., *Tsyganenko et al.*, 1987] should improve the

accuracy of the VLF ray tracer and resulting precipitation. As discussed in Section 3.3.1, the plasmaspheric density used in the ray tracing model plays a critical role in determining the spatial location of the electron precipitation. Refinements to the plasmaspheric equatorial and field line density should improve the accuracy of the calculation.

The third set of inputs that could be modified is the trapped radiation belt flux model used. In this dissertation, the AE8 radiation belt model [*Vette*, 1991] is used with a "square" pitch angle distribution (Figure 3.6). While simulations are also run with a "sine" pitch angle distribution, a more thorough investigation of the dependence of the calculated precipitation on the radiation belt pitch angle distribution and flux levels should help explain the variability in LEP events that have been observed [*Peter and Inan*, 2004].

**Monte Carlo Model of Ionospheric Density Enhancement**

In this dissertation for the model of ionospheric density enhancement we used the model setup detailed in *Lehtinen* [2000], with only slight modifications as detailed in Section 3.3.2. The main refinement that would affect this model would be the pitch angle distribution of the electron precipitation input into the model. As suggested in Section 4.4, the precipitation in the northern hemisphere is likely a result of electrons that have first backscattered in the southern hemisphere. The Monte Carlo model of energy deposition also calculates the pitch angle distribution of backscattered particles, and hence could be used to determine the pitch angle distribution of these particles as they return to the northern hemisphere. This refinement to the model might also explain the differences in onset delay between the model and observations (Figure 4.5).

**FDFD Model of VLF Signal Propagation**

In this dissertation, the model of VLF signal propagation is based on the work of *Chevalier and Inan* [2006], with only slight modifications as detailed in Section 3.3.3.

The simulation used in this dissertation is only two dimensional, ignoring the variations perpendicular to the path of propagation. For smaller and more intense ionospheric disturbances, a three-dimensional treatment that incorporates variations in ionospheric density perpendicular to the signal path will improve the accuracy of the calculation. Furthermore, the ambient density and collision frequency profiles used in this dissertation are assumed to be constant along the path. Using a more accurate model of the ambient conditions should also improve the accuracy of the model.

## 6.3.2   Refinement of Metrics and Conversion Ratios

The metrics $N_{\mathrm{ILDE}}$ and $\Gamma$ and the corresponding conversion ratios ($\alpha_{\mathrm{ILDE}}$ and $\Psi$) are developed for particular application to the two LEP events examined in this dissertation. However, the general methodology used to quantify the precipitation and ionospheric disturbance can be applied to other precipitation events. The application of this methodology to other precipitation events and other VLF signal paths would refine these metrics and conversion ratios and enhance their accuracy. The application of this methodology has already been demonstrated for transmitter-induced precipitation, as detected on a VLF signal path from the NLK transmitter in Jim Creek, Washington to a VLF receiver located in Midway, Hawaii [*Inan et al.*, 2007]. Also, the conversion ratios are defined relative to VLF signal amplitude changes in dB, rather than in linear units. For a greater range of signal amplitude perturbations, the conversion ratio may not be linear with dB units, and hence should be modified accordingly.

The metric $\Gamma$ is used to estimate the number of particles precipitated (100-300 keV) over a given path. However, the number of particles precipitated is defined as the number of particles scattered into the northern bounce loss cone. This number is different than the number of particles that deposit their energy into the atmosphere directly, as not all particles in the bounce loss cone will deposit their energy on the first bounce (Figure 3.7c). Instead $\Gamma$ could be calculated using the number of particles that directly deposit their energy into the atmosphere, not the number of particles scattered into the bounce loss cone. As the relative roles of direct versus backscattered

precipitation are more clearly understood, the choice of how to define $\Gamma$ will become clearer.

### 6.3.3   Determining the Role of LEP in Radiation Belt Loss

This dissertation describes a methodology to quantitatively estimate the energetic electron precipitation and ionospheric density enhancement associated with LEP events using only observations of VLF signal perturbations and previously defined conversion ratios. The more general purpose of this methodology is to assess the role of LEP in radiation belt loss. To accomplish this goal, this methodology must be expanded to other regions of the world and other VLF signal paths (as referred to above), and the occurrence rates of LEP events determined.

**Occurrence Rates of LEP Events**

Recent work [i.e., *Peter and Inan*, 2004] demonstrated that occurrence rates of LEP events are highly variable, and exhibit strong dependence on geomagnetic activity [*Leyser et al.*, 1984; *Peter et al.*, 2005b]. Measurements of electron fluxes from the NOAA-POES satellite support the notion that LEP occurrence variability is largely due to geomagnetic storm-associated variability in the slot-region electron population [*Peter and Inan*, 2004; *Peter et al.*, 2005b]. Quantification of LEP occurrence rates, and delineating its dependence on causative lightning activity versus geomagnetic activity, is needed to infer radiation belt loss rates. Understanding the role of various parameters on the amount of precipitation induced by a given lightning flash is the next step in more accurately estimating the role of LEP-driven losses. The duration, spatial extent, and energy spectra of the precipitation are likely influenced by such parameters as: P1) causative lightning flash current [*Peter and Inan*, 2004]; P2) trapped radiation belt fluxes and magnetospheric conditions [*Peter et al.*, 2005b]; P3) pitch angle distribution of trapped flux [*Inan et al.*, 1989]; and P4) causative lightning flash location [*Bortnik et al.*, 2003a]. The relative contribution of these parameters to the LEP-driven global loss rates driven is not yet fully understood, and additional parameters such as equinoctial dependence [*Leyser et al.*, 1984] may

also play a role.

Quantification of the role of lightning-induced whistlers in the loss of electron radiation requires an accurate estimate of the amount of precipitation (both temporal profile and spatial extent) induced by a single lightning flash given the relevant parameters P1, P2, P3, and P4, as listed above. Continuous VLF measurements at the HAIL sites are critical in quantifying the influence of these parameters, and preliminary work on establishing a statistical dependence of precipitation on these parameters has been initiated. VLF LEP event recognition software is used to create a six-month database of LEP event occurrence and locations for northern hemisphere data on HAIL. This event database is correlated with both lightning characterization data and satellite (i.e., NOAA-POES) measurements of trapped radiation belt flux levels to determine the influence of both magnetospheric and thunderstorm conditions on the occurrence rates and precipitation flux levels of LEP events. Based on this analysis, the amount of precipitation loss from the radiation belts is calculated based on the characteristics of a given lightning storm. With extension to other regions of the globe, including southern hemisphere precipitation, the occurrence rates of LEP loss can be calculated on a global scale.

**Diffusion Coefficients**

Finally, as mentioned above for the metric $\Gamma$, precipitation loss is defined in this dissertation as the number of particles that have been scattered into the bounce loss cone. However, the role of LEP in radiation belt loss should also be measured in terms of diffusion coefficients, in order to be comparable to other works [i.e., *Abel and Thorne*, 1998a,b]. To do this, the occurrence rates of LEP events must be determined as described above. The use of VLF remote sensing to measure LEP events is only useful in measuring $D_{\alpha\alpha}$ near the edge of the loss cone, as the pitch angle scattering involved is typically small. The loss of radiation belt particles is partly determined by the diffusion rate near the loss cone, and hence the estimation of $D_{\alpha\alpha}$ near the edge of the loss cone will help determine the role of LEP in radiation belt loss.

# Bibliography

Abel, B. and R. M. Thorne, Electron scattering loss in Earth's inner magnetosphere: 1. Dominant physical processes, *J. Geophys. Res., 103,* 2385-2396, 1998a.

Abel, B. and R. M. Thorne, Electron scattering loss in Earth's inner magnetosphere: 2. Sensitivity to model parameters, *J. Geophys. Res., 103,* 2397-2407, 1998b.

Angerami, J.J., and J.O. Thomas, Studies of planetary atmospheres. 1. Distribution of electrons + ions in Earth's exosphere, *J. Geophys. Res., 69 (21),* 4537, 1964.

Angerami, J. J., Whistler duct properties deduced from VLF observations made with the OGO 3 satellite near the magnetic equator, *J. Geophys. Res., 75,* 6115-6135, 1970.

Banks, P.M., C.R. Chappell, and A.F. Nagy, A new model for the interaction of auroral electrons with the atmosphere: spectral degradation, backscatter, optical emissions, and ionization, *J. Geophys. Res., 79 (10),* 1459-1470, 1974.

Bell, T.F., The nonlinear gyroresonance interaction between energetic electrons and coherent VLF waves propagating at an arbitrary angle with respect to the Earth's magnetic field, *J. Geophys. Res., 89 (A2),* 905-918, 1984.

Bell, T.F., U.S. Inan, J. Bortnik, and J.D. Scudder, The Landau damping of magnetospherically reflected whistlers within the plasmasphere, *Geophys. Res. Lett., 29 (15),* 1733, 2002.

Blake, J. B., U. S. Inan, M. Walt, T. F. Bell, J. Bortnik, D. L. Chenette, and H. J.

Christian, Lightning-induced energetic electron flux enhancements in the drift loss cone, *J. Geophys. Res., 106*, A12, 29733-29744, 2001.

Bortnik J., U. S. Inan, and T. F. Bell, *L* dependence of energetic electron precipitation driven by magnetospherically reflecting whistler waves, *J. Geophys. Res., 107 (A8),* doi:10.1029/2001JA000303, 2002.

Bortnik, J., U. S. Inan, and T. F. Bell, Energy distribution and lifetime of magnetospherically reflecting whistlers in the plasmasphere, *J. Geophys. Res., 108(A5),* 1199, doi:10.1029/2002JA009316, 2003a.

Bortnik, J., U. S. Inan, and T. F. Bell, Frequency-time spectra of magnetospherically reflecting whistlers in the plasmasphere, *J. Geophys. Res., 108(A1),* 1030, doi:10.1029/2002JA009387, 2003b.

Bortnik, J., Precipitation of radiation belt electrons by lightning-generated magnetospherically reflecting whistler waves, *Stanford University Thesis,* Stanford University, Palo Alto, CA USA, 2004.

Bortnik, J., U. S. Inan, and T. F. Bell, Temporal signatures of radiation belt electron precipitation induced by lightning-generated MR whistler waves: 1. Methodology, *J. Geophys. Res., 111,* A02204, doi:10.1029/2005JA011182, 2006a.

Bortnik, J., U. S. Inan, and T. F. Bell, Temporal signatures of radiation belt electron precipitation induced by lightning-generated MR whistler waves: 2. Global signatures, *J. Geophys. Res., 111,* A02205, doi:10.1029/2005JA011398, 2006b.

Bracewell R. N. and T. W. Straker, The study of solar flares by means of very long radio waves, *Mon. Not. R. Astr. Soc., 109,* 28-45, 1949.

Brinca, A.L., On the stability of obliquely propagating whistlers, *J. Geophys. Res., 77 (19),* 3495, 1972.

Budden, K. G., The influence of the Earth's magnetic field on radio propagation by waveguide modes, *Proceedings of the Royal Society A, 265,* 1962.

Burgess, W. C., and U. S. Inan, Simultaneous disturbance of conjugate ionospheric regions in association with individual lightning flashes, *Geophys. Res. Lett., 17,* 259-262, 1990.

Burgess, W. C., and U. S. Inan, The role of ducted whistlers in the precipitation loss and equilibrium flux of radiation belt electrons, *J. Geophys. Res., 98,* 15643-65, 1993.

Carpenter, D. L., and J. W. LaBelle, A study of whistlers correlated with bursts of electron precipitation near L=2, *J. Geophys. Res., 84,* (A6), 4427-4434, 1982.

Carpenter, D. L., U. S. Inan, M. L. Trimpi, R. A. Helliwell, and J. P. Katsufrakis, Perturbations of subionspheric LF and MF signals due to whistler-induced electron precipitation bursts, *J. Geophys. Res., 89,* (A11), 9857-9862, 1984.

Carpenter, D. L., and R. R. Anderson, An ISEE/whistler model of equatorial electron density in the magnetosphere, *J. Geophys. Res., 97,* (A2), 1097-1108, 1992.

Carpenter, D. L., M. Galand, T. F. Bell, V. S. Sonwalkar, U. S. Inan, J. LaBelle, A. J. Smith, T. D. G. Clark, and T. J. Rosenberg, Quasiperiodic 5-60 s fluctuations of VLF signals propagating in the earth-ionosphere waveguide: A result of pulsating auroral particle precipitation?, *J. Geophys. Res., 102,* (A1) 347-361, 1997.

Chang, H.C., and U.S. Inan, A theoretical-model study of observed correlations between whistler mode waves and energetic electron precipitation events in the magnetosphere, *J. Geophys. Res., 88 (A12),* 53-58, 1983.

Chang, H.C., and U.S. Inan, Lightning-induced electron precipitation from the magnetosphere, *J. Geophys. Res., 90 (A2),* 1531-1541, 1985a.

Chang, H.C., and U.S. Inan, Test particle modeling of wave-induced energetic electron precipitation, *J. Geophys. Res., 90 (A7),* 6409-6418, 1985b.

Chevalier, M. W., U. S. Inan, A technique for efficiently modeling long path propagation for use in both FDFD and FDTD, *IEEE AWPL, 5,* 525-528, 10.1109/LAWP.2006.887551, 2006.

Chevalier, M. W., U. S. Inan, W. B. Peter, and T. F. Bell, Remote sensing of iono-spheric disturbances associated with relativistic particle precipitation using the South Pole VLF beacon, *J. Geophys. Res.,* [In Preparation], 2007a.

Chevalier, T. W., U. S. Inan, T. F. Bell, Terminal impedance and antenna current distribution of a VLF electric dipole in the inner magnetosphere, *IEEE Transactions on Antennas and Propagation,* [In Review], 2007b.

Chilton C. J., VLF phase perturbation associated with meteor shower ionization, *J. Geophys. Res., 66,* 379-383, 1961.

Christian, H. F., R. J. Blakeslee, D. J. Boccippio, W. L. Boeck, D. E. Buechler, K. T. Driscoll, S. J. Goodman, J. M. Hall, W. J. Koshak, D. M. Mach, and M. F. Stewart, Global frequency and distribution of lightning as observed by the Optical Transient Detector (OTD), *11th International Conference on Atmospheric Electricity, 209261,* 726-729, 1999.

Clilverd M. A., D. Nunn, S. J. Lev-Tov, U. S. Inan, R. L. Dowden, C. J. Rodger, and A. J. Smith, Determining the size of lightning-induced electron precipitation patches, *J. Geophys. Res., 107 (A8),* doi:10.1029/2001JA000301, 2002.

Clilverd M. A., C. J. Rodger, D. Nunn, Radiation belt electron precipitation fluxes associated with lightning, *J. Geophys. Res., 109,* A12208, doi:10.1029/2004JA010644, 2004.

Cornwall, J. M., Scattering of energetic trapped electrons by very low frequency waves, *J. Geophys. Res., 69,* 1251, 1964.

Cummer, S. A., T. F. Bell, and U. S. Inan, VLF Remote sensing of high-energy auroral particle precipitation, *J. Geophys. Res., 102,* 7477-7484, 1997.

Cummins, Kenneth L., Martin J. Murphy, Edward A. Bardo, William L. Hiscox, Richard B. Pyle, and Alburt E. Pifer, A combined TOA/MDF technology upgrade of the U.S. National Lightning Detection Network, *J. Geophys. Res., 103,* 9035-44, 1998.

Demirkol, M. K., U. S. Inan, T. F. Bell, S. G. Kanekal, D. C. Wilkinson, Ionospheric effects of relativistic electron enhancement events, *Geophys. Res. Lett., 26,* 3557-3560, 1999.

Draganov, A. B., U. S. Inan,V. S. Sonwalkar, and T. F. Bell, Magnetospherically reflected whistlers as a source of plasmaspheric hiss, *Geophys. Res. Lett., 19, 3,* 233-236, 1992.

Dungey, J.W., Loss of Van Allen electrons due to whistlers, *Planetary and Space Science, 11 (6),* 591-595, 1963.

Ferguson, J. A. and F. P. Snyder, The segmented waveguide programs for long wavelength propagation calculations, *Tech. Doc., 1071,* Naval Ocean Syst. Cent., San Diego, Calif., 1987.

Fishman, G. J., and U. S. Inan, Observation of an ionospheric disturbance caused by a gamma-ray burst, *Nature, 331,* 418-420, 1988.

Friedel, R. H. W., and A. Korth, Long-term observations of keV ion and electron variability in the outer radiation belt from CRRES, *Geophys. Res. Lett., 22,* 1853-1856, 1995.

Gaines, E. E., D. L. Chenette, W. L. Imhof, C. H. Jackman, and J. D. Winningham, Relativistic electron fluxes in May 1992 and their effect on the middle atmosphere, *J. Geophys. Res., 100,* 1027, 1995.

Glukhov, V. S., V. P. Pasko, and U. S. Inan, Relaxation of transient lower ionospheric disturbances caused by lightning-whistler-induced electron precipitation bursts, *J. Geophys. Res., 97,* 16971-79, 1992.

Green, J.L., S. Boardsen, L. Garcia, W. W. L. Taylor, S. F. Fung, and B.W. Reinisch, On the origin of whistler mode radiation in the plasmasphere, *J. Geophys. Res., 110,* A03201, doi:10.1029/2004JA010495, 2005.

Hargreaves, J. K., The solar-terrestrial environment, *Cambridge University Press,* 1992.

Haselgrove, J., Ray theory and a new method for ray tracing, *Report of the Physical Society Conference on Physics of the Ionosphere,* Cambridge, England, 355-364, 1954.

Helliwell, R.A., Whistlers and related ionospheric phenomena, *Stanford University Press,* Stanford, Calif., 1965.

Helliwell, R. A., J. P. Katsufrakis, and M. L. Trimpi, Whistler-induced amplitude perturbation in VLF propagation, *J. Geophys. Res., 78,* 4679, 1973.

Horne, R. B., The contribution of wave particle interactions to electron loss and acceleration in the Earths radiation belts during geomagnetic storms, *in Review of Radio Science 1999-2002,* edited by W. R. Stone, pp. 801- 828, John Wiley, New York, 2002.

Inan, U.S. and T. F. Bell, The plasmapause as a VLF wave guide, *J. Geophys. Res., 83(19),* 2819, 1977.

Inan, U.S., T.F. Bell, and R.A. Helliwell, Nonlinear pitch-angle scattering of energetic electrons by coherent VLF waves in the magnetosphere, *J. Geophys. Res., 82 (19),* 127-142, 1978.

Inan, U. S., T. F. Bell, and H. C. Chang, Particle-precipitation induced by short-duration VLF waves in the magnetosphere, *J. Geophys. Res., 87 (A8),* 6243-6264, 1982.

Inan, U.S., H.C. Chang, R.A. Helliwell, W.L. Imhof, J.B. Reagan, and M. Walt, Precipitation of radiation belt electrons by man-made waves - a comparison between theory and measurement, *J. Geophys. Res., 90 (A1),* 359-369, 1985a.

Inan, U. S., D. L. Carpenter, R. A. Helliwell, and J. P. Katsufrakis, Subionospheric VLF/LF phase perturbations produced by lightning-whistler induced particle precipitation, *J. Geophys. Res., 90,* 7457, 1985b.

Inan, U. S., and D. L. Carpenter, On the correlation of whistlers and associated subionospheric VLF/LF perturbations, *J. Geophys. Res., 91,* 3106-16, 1986.

Inan, U. S., and D. L. Carpenter, Lightning-induced electron precipitation events observed at $L\sim2.4$ as phase and amplitude perturbations on subionospheric VLF signals, *J. Geophys. Res., 92,* 3293-3303, 1987.

Inan, U. S., D. C. Shafer, W. Y. Yip, and R. E. Orville, Subionospheric VLF signatures of nighttime $D$ region perturbations in the vicinity of lightning discharges, *J. Geophys. Res., 93,* 11455-72, 1988a.

Inan, U. S., T. G. Wolf, and D. L. Carpenter, Geographic distribution of lightning-induced electron precipitation observed as VLF/LF perturbation events, *J. Geophys. Res., 93,* 9841, 1988b.

Inan, U.S., M. Walt, H. Voss, and W. Imhof, Energy spectra and pitch angle distribution of lightning-induced electron precipitation: analysis of an event observed on the S81-1 (SEEP) satellite, *J. Geophys. Res., 94, (A2),* 1379-1401, 1989.

Inan, U. S., F. A. Knifsend, and J. Oh, Subionospheric VLF "imaging" of lightning-induced electron precipitation from the magnetosphere, *J. Geophys. Res., 95,* 17,217-17,231, 1990.

Inan, U. S., T. F. Bell, V. P. Pasko, D. D. Sentman, E. M. Wescott, and W. A. Lyons, VLF signatures of ionospheric disturbances associated with sprites, *Geophys. Res. Lett., 22,* 3461-3464, 1995.

Inan, U. S., N. G. Lehtinen, S. J. Lev-Tov, M. P. Johnson, T. F. Bell, and K. Hurley, Ionization of the lower ionosphere by gamma rays from a magnetar: Detection of a low energy (3-10 keV) component, *Geophys. Res. Lett., 26,* 3357-3360, 1999.

Inan, U. S., M. Golkowski, M. K. Casey, R. C. Moore, W. Peter, P. Kulkarni, P. Kossey, and E. Kennedy, Subionospheric VLF observations of transmitter-induced precipitation of inner radiation belt electrons, *Geophys. Res. Lett., 34,* L02106, doi:10.1029/2006GL028494, 2007.

Jasna, D., U. S. Inan, and T. F. Bell, Precipitation of suprathermal (100 eV) electrons by oblique whistler waves, *Geophys. Res. Lett., 19,* 1639, 1992.

Jasna, D., Gyroresonant scattering of radiation belt electrons by oblique whistler waves, *Stanford University Thesis,* Stanford University, Palo Alto, CA USA, 1993.

Johnson, M. P., U. S. Inan, and D. S. Lauben, Subionospheric VLF signatures of oblique (nonducted) whistler-induced precipitation, *Geophys. Res. Lett., 26,* 3569-72, 1999.

Johnson, M. P., VLF imaging of lightning-induced ionospheric disturbances, *Stanford University Thesis,* Stanford University, Palo Alto, CA USA, 2000.

Lauben, D. S., Precipitation of radiation belt electrons by obliquely-propagating lightning-generated whistler waves, *Stanford University Thesis,* Stanford University, Palo Alto, CA USA, 1998.

Lauben, D. S., U. S. Inan, and T. F. Bell, Poleward-displaced electron precipitation and lightning-generated oblique whistlers, *Geophys. Res. Lett., 26,* 2633-36, 1999.

Lauben, D. S., U. S. Inan, and T. F. Bell, Precipitation of radiation belt electrons induced by obliquely propagating lightning-generated whistlers, *J. Geophys. Res., 106,* 29745-29770, 2001.

Lee, J. H. and D. K. Kalluri, Three-dimensional FDTD simulation of electromagnetic wavetransformation in a dynamic inhomogeneous magnetized plasma, *IEEE Transactions on Antennas and Propagation, 47, (7),* 1999.

Lehtinen, N. G., Relativistic runaway electrons above thunderstorms, *Stanford University Thesis,* Stanford University, Palo Alto, CA USA, 2000.

Lehtinen, N. G., U. S. Inan, T. F. Bell, Effects of thunderstorm-driven runaway electrons in the conjugate hemisphere: Purple sprites, ionization enhancements, and gamma rays, *J. Geophys. Res., 106(A12),* 28841-28856, 10.1029/2000JA000160, 2001.

Lev-Tov, S. J., U. S. Inan, T. F. Bell, Altitude profiles of localized $D$ region density disturbances produced in lightning-induced electron precipitation events, *J. Geophys. Res., 100(A11),* 21375-21384, 10.1029/95JA01615, 1995.

Leyser, T. B., U. S. Inan, D. L. Carpenter, and M. L. Trimpi, Diurnal variation of burst precipitation effects on subionospheric VLF/LF signal propagation near L = 2, *J. Geophys. Res., 89,* 9139-9143, 1984.

Lyons, L.R., R.M. Thorne, and C.F. Kennel, Electron pitch-angle diffusion driven by oblique whistler-mode turbulence, *J. Plasma Physics, 6 (Part 3),* 589-606, 1971.

Lyons, L.R., R.M. Thorne, and C.F. Kennel, Pitch-angle diffusion of radiation-belt electrons within the plasmasphere, *J. Geophys. Res., 77 (19),* 3455-3474, 1972.

Lyons, L.R., and R.M. Thorne, Equilibrium structure of radiation belt electrons, *J. Geophys. Res., 78 (13),* 2142-2149, 1973.

Morfitt, D. G., and C. H. Shellman, MODESRCH: An improved computer program for obtaining ELF/VLF/LF mode constants in an Earth-ionosphere waveguide, *Interim Report Number 77T,* Propagation Technology Division, Naval Ocean Systems Center, San Diego, California, 1976.

NRCR, National Research Council Report, *A Decadal Research Strategy in Solar and Space Physics,* 2003.

Park, C. G., Methods of determining electron concentrations in the magnetosphere from nose whistlers, *Technical Report 3454-1,* Stanford University, Stanford, CA 1972.

Pasko, V. P. and U. S. Inan, Recovery signatures of lightning-associated VLF perturbation as a measure of the lower ionosphere, *J. Geophys. Res., 99,* 17523-17537, 1994.

Peter, W. B. and U. S. Inan, On the occurrence and spatial extent of electron precipitation induced by oblique nonducted whistler waves, *J. Geophys. Res., 109,* A12215, doi:10.1029/2004JA010412, 2004.

Peter, W. B., and U. S. Inan, Electron precipitation events driven by lightning in hurricanes, *J. Geophys. Res., 110,* A05305, doi:10.1029/2004JA010899, 2005a.

Peter, W. B., M. Chevalier, and U. S. Inan, Subionospheric VLF measurements of the effects of geomagnetic storms on the mid-latitude $D$-region, *11th International Ionosphere Effects Symposium, A070,* May 3-5, 2005b.

Peter, W. B., M. W. Chevalier, and U. S. Inan, Perturbations of midlatitude subionospheric VLF signals associated with lower ionospheric disturbances during major geomagnetic storms, *J. Geophys. Res., 111,* A03301, doi:10.1029/2005JA011346, 2006.

Peter, W. B. and U. S. Inan, Quantitative measurement of lightning-induced electron precipitation via VLF remote sensing, *J. Geophys. Res.,* [in review], 2007.

Poulsen, W. L., T. F. Bell, and U. S. Inan, Three-dimensional modeling of subionospheric VLF propagation in the presence of localized $D$ region perturbations associated with lightning, *J. Geophys. Res., 95,* (A3), 2355-2366, 1990.

Poulsen, W. L., U. S. Inan, and T. F. Bell, A multiple-mode three-dimensional model of VLF propagation in the earth-ionosphere waveguide in the presence of localized $D$ region disturbances, *J. Geophys. Res., 98,* 1705-1717, 1993a.

Poulsen, W. L., T. F. Bell, and U. S. Inan, The scattering of VLF waves by localized ionospheric disturbances produced by lightning-induced electron precipitation, *J. Geophys. Res., 98,* 15553-15559, 1993b.

Prentice S. A., and D. Mackeras, The ratio of cloud to cloud-ground lightning flashes in thunderstorms, *Radio Sci., 6,* 299, 1971.

Rees, M. H., Auroral ionization and excitation by incident energetic electrons, *Planet. Space Sci., 11,* 1209, 1963.

Ristic'-Djurovic', J.L., T.F. Bell, and U.S. Inan, Precipitation of radiation belt electrons by magnetospherically reflecting whistlers, *J. Geophys. Res., 103 (A5),* 9249-9260, 1998.

Roberts, C.S., Pitch angle diffusion of electrons in the magnetosphere, *Rev. Geophys., 7,* 305, 1969.

Rodger C. J., M. A. Clilverd, and R. L. Dowden, D region reflection height modification by whistler-induced electron precipitation, *J. Geophys. Res., 107 (A7),* doi:10.1029/2001JA000311, 2002.

Rodger, C. J., D. Nunn, and M. A. Clilverd, Investigating radiation belt losses though numerical modeling of precipitating fluxes, *Ann. Geophys., 22,* 36573667, 2004.

Sechrist, C. F., Jr., Comparison of techniques for measurement of the *D*-region electron densities, *Radio Sci., 9,* 137, 1974.

Sonwalkar, V. S., and U. S. Inan, Lightning as an embryonic source of VLF hiss, *J. Geophys. Res., 94, (A6),* 6986-6994, 1989.

Spasojevic, M., Conversation, Stanford Calif., 2006.

Strangeways, H. J., Lightning induced enhancements of D region ionisation and whistler ducts, *J. Atmos. Sol. Terr. Phys., 61,* 1067 1080, 1999.

Taflove, A. and S. C. Hagness, Computational electrodynamics: the finite-difference time-domain method, *Artech House,* 2000.

Tarcsai, G., P. Szemeredy, and L. Hegymegi, Average electron density profiles in the plasmasphere between $L$=1.4 and 3.2 deduced from whistlers, *Journal of Atmospheric and Terrestrial Physics, 50,* 607-611, 1988.

Tsyganenko, N. A., A. V. Usmanov, V. O. Papitashvili, N. E. Papitashvili, and V. A. Popov, Software for computations of the geomagnetic field and related coordinate systems, *Soviet Geophys. Comm.,* Moscow, 58 pp., 1987.

Uman, M. A., *Lightning,* Dover, Mineola, N.Y., 1984.

Vampola, A. L., VLF transmitter-induced slot electron precipitation, *Geophys. Res. Lett., 4,* 569, 1977.

Vette, J., The AE-8 trapped electron model environment, National Space Science Data Center, *Report 91-24,* Greenbelt, Maryland, 1991.

Voss, H. D., W. L. Imhof, M. Walt, J. Mobilia, E. E. Gaines, J. B. Reagan, U. S. Inan, R. A. Helliwell, D. L. Carpenter, J. P. Katsufrakis, and H. C. Chang, Lightning-induced electron precipitation, *Nature, 312,* 740-742, 1984.

Voss, H. D., M. Walt, W. L. Imhof, J. Mobilia, U. S. Inan, Satellite observations of lightning-induced electron precipitation, *J. Geophys. Res., 103(A6),* 11725-11744, 10.1029/97JA02878, 1998.

Wait, J. R., and K. P. Spies, Characteristics of the Earth-ionosphere waveguide for VLF radio waves, Technical Note 300 , *National Bureau of Standards,* Boulder, CO, 1964.

Walt, M. and W. MacDonald, The influence of the Earth's atmosphere on geomagnetically trapped particles, *Rev. Geophys., 2,* 543, 1964.

Walt, M., Introduction to Geomagnetically Trapped Radiation, *Cambridge University Press,* 1994.

Wolf, T. G., and U. S. Inan, Path-dependent properties of subionospheric VLF amplitude and phase perturbations associated with lightning, *J. Geophys. Res., 95, (A12),* 20, 997-21,005, 1990.

Zhao, Y. J., K. L. Wu, and K. K. M. Cheng, A compact 2-D full-wave finite-difference frequency-domain method for general guided wave structures, *IEEE Trans. Microwave Theory Tech., vol. 50,* pp. 1844 1848, July 2002.

Zmuda, A. J., B. W. Shaw, and C. R. Haave, VLF disturbances caused by the nuclear detonation of October 26, 1962, *J. Geophys. Res., 68,* 4105-4114, 1963.